Making and Breaking of Chemical Bonds:

Dynamics of Elementary Reactions

From Gas Phase to Condensed Phase

Dr. rer. nat. Burkhard Schmidt [1] [2]

Vorgelegt dem Fachbereich Chemie
der Freien Universität Berlin
als Habilitationsschrift im Fach

"Theoretische Chemie"

Berlin, im Juli 1998

[1] Electronic mail: burkhard@math.fu-berlin.de
[2] World Wide Web: http://www.math.fu-berlin.de/∼burkhard

Contents

1 Introduction **7**

2 Photo–Induced Stabilization **11**
2.1 Motivation 13
2.2 Method 15
2.2.1 General Dynamical Equations 15
2.2.2 Dynamical Equations for a Diatomic System 16
2.2.3 Interaction Operator 17
2.2.4 Grid Representations 18
2.2.5 Eigenstate Representations 19
2.2.6 Perturbation Theory 21
2.3 State–Selectivity 23
2.3.1 Model Systems 23
2.3.2 Populations and Selectivity 25
2.3.3 Initial States 25
2.3.4 Vibrational State Selectivity 28
2.3.5 Electronic State Selectivity 31
2.3.6 Rotational State–Selectivity 34
2.3.7 Summary and Outlook 39
2.4 Wavepacket Dynamics 40
2.4.1 Model System 40
2.4.2 Excitation probability 40
2.4.3 Vibrational Coherence 42
2.4.4 Rotational Coherence 44
2.4.5 Thermal averaging 45
2.4.6 Summary and Outlook 46

3 Solvent–Induced Stabilization **49**
3.1 Motivation 51
3.2 Computational Details 53
3.2.1 Introductory Remarks 53
3.2.2 Cross Sections 53
3.2.3 Classical Trajectories 55
3.2.4 Potential Energy Surfaces 56
3.3 Atom–Cluster Reactions 58
3.3.1 One Atom Acting as a Solvent 58

3.3.2 The First Solvation Shell . . . 62
3.3.3 Summary and Outlook . . . 68
3.4 Cluster–Cluster Reactions . . . 69
3.4.1 Introduction . . . 69
3.4.2 Cluster Structures . . . 69
3.4.3 Lifetimes of Collision Complexes . . . 70
3.4.4 Association Cross Sections . . . 71
3.4.5 Summary and Outlook . . . 72

4 Photodissociation in Clusters, Matrices 75
4.1 Motivation . . . 77
4.2 Model and Interactions . . . 79
4.2.1 Ground State . . . 79
4.2.2 Excited State . . . 80
4.2.3 Model Systems . . . 82
4.3 Method . . . 84
4.3.1 General Approximations . . . 84
4.3.2 Ground State Wavefunctions . . . 84
4.3.3 Excited State Dynamics . . . 85
4.3.4 Quantum–Classical Molecular Dynamics (QCMD) . . . 87
4.3.5 Symmetry Adapted Spherical Harmonics (SASHs) . . . 88
4.4 Vibrational Energy Shifts . . . 89
4.4.1 Solvent Structure . . . 89
4.4.2 Results . . . 89
4.4.3 Discussion . . . 91
4.5 Rotational Shifts and Wavefunctions . . . 92
4.5.1 Introduction . . . 92
4.5.2 Potential Energy Surfaces . . . 93
4.5.3 Energy Levels . . . 94
4.5.4 Wave Functions . . . 95
4.5.5 Discussion . . . 97
4.6 Photodissociation Dynamics . . . 98
4.6.1 Hydrogen Wavepacket Dynamics . . . 98
4.6.2 Cage Exit Probabilties . . . 100
4.6.3 Absorption Spectra . . . 102
4.6.4 Cage Dynamics . . . 104
4.6.5 Summary . . . 106
4.6.6 Outlook . . . 107

5 Extended Summary 109

6 Ausführliche Zusammenfassung 115

A Photo–Induced Stabilization 143
A.1 Vibrational State–Selectivity . . . 143
A.2 Competition with Photoacceleration . . . 145
A.3 Electronic State–Selectivity . . . 147

A.4 Rotational State Selectivity 149
A.5 Wavepacket Dynamics 151

B Solvent–Induced Stabilization **153**
B.1 Three–Body Collisions and the Chaperon Effect 153
B.2 Phase Transitions and the Cage Effect 155
B.3 Effect of Evaporative Cooling 157

C Photodissociation Dynamics **159**
C.1 Vibrational Frequency Shifts 159
C.2 Photodissociation of Molecules in Clusters 161
C.3 Photodissociation of Molecules in Matrices 163

Chapter 1

Introduction

The formation of new molecular bonds and the cleavage of existing ones are among the most elementary steps that any chemical reaction, however complex the underlying mechanism may be, is comprised of [1]. In a very simplistic view, the processes of "making" and "breaking" of molecular bonds can be considered as first and second half of a (reactive or non–reactive) collision, respectively (see Fig. 1.1 a). In association reaction, two reactants come together to form a (free or quasi–bound) collision complex which corresponds to the transition state in the statistical theory of chemical kinetics and dynamics [2,3,4,5] (see Fig. 1.1 b). During the lifetime of the collision process energy transfer between the various degrees of freedom may occur, and the atoms may rearrange. The subsequent decay of this collision complex is equivalent to a dissociation process (see Fig. 1.1 c). This view of association and dissociation reactions as "half collision" reveals the similarity of these reactions with scattering processes. Indeed, many concepts of reactive scattering can be applied to the (theoretical) treatment of these processes [6, 7, 8, 9, 10, 11, 12, 13, 14, 15, 16].

If the formation of the collision complex involves electromagnetic (permanent or transition) moments, external fields can be used to manipulate the transition state. In analogy to the above view of a reactive collision, one can consider the processes of photoassociation and photodissociation as initial and final phase of a light–assisted collision [12, 13, 17]. The development of spectroscopy of the transition state is tightly connected with the availability of short light pulses [18]. In recent years the spectroscopy of the transition state has made enormous progress and meanwhile the available pulse lengths have reached the femtosecond regime [19, 20, 21, 22, 23, 24]. At the same time, modern femtochemistry has progressed from the mere observation of the chemical dynamics to its active manipulation by novel control mechanisms based on ultrashort laser pulses [25, 26].

This experimental progress has been closely interconnected with a revival of the time–dependent formulation of quantum mechanics. In particular, the concept of wavepacket dynamics [27, 28] has been introduced to the field of molecular dynamics, and the implementation of new and powerful numerical techniques [29, 30, 31, 32, 33, 34] has lead to a new standard tool in the theory of chemical reaction dynamics and kinetics [35, 36, 15, 16, 37, 38, 39]. Currently,

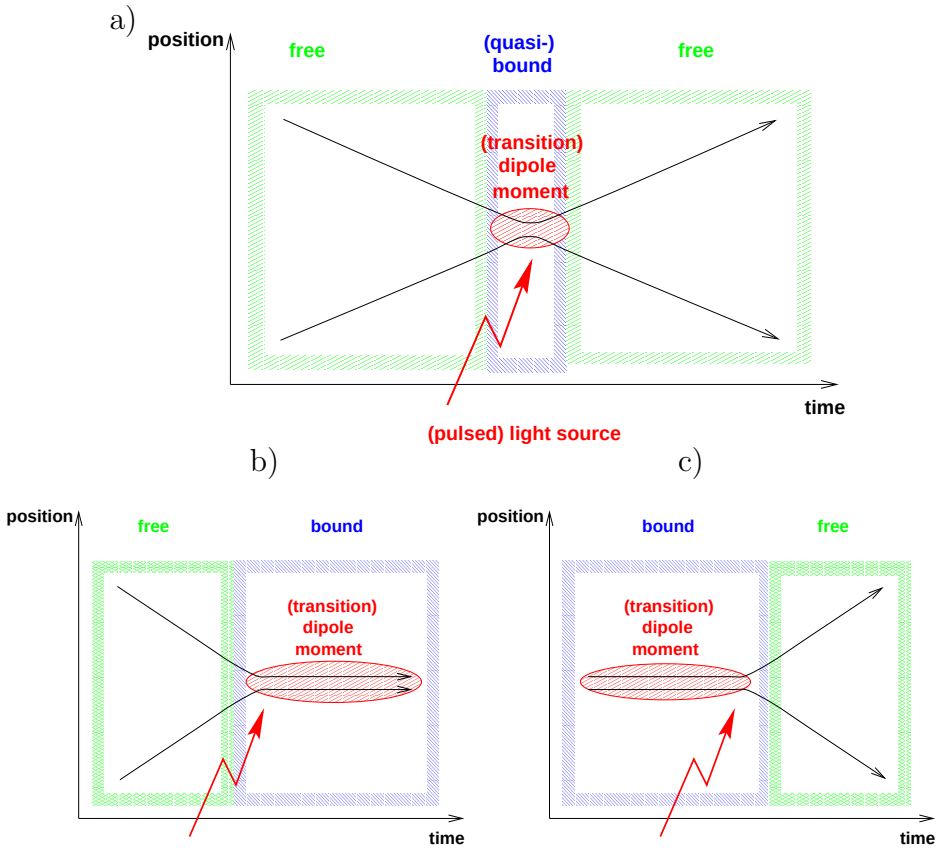

Figure 1.1: a) General scheme of a light–assisted (reactive) collision. In the position–space representation, two reactants collide with each other. In the transition state, light–assisted rearrangements of the atoms may take place and finally the products separate from each other. b) (Photo–)association as first half of a collision process. c) (Photo–)dissociation as second half of a collision process.

one of the main challenges lies in the development of (approximate) methods for quantum molecular dynamics in large systems in order to support the development of femtochemistry towards larger molecules, clusters, and ultimately to molecules in condensed phases.

In the three main sections of the present thesis work, we want to apply the concepts of modern femtochemistry to the following three types of elementary reactions of making and breaking of chemical bonds:

- The association process requires (at least) a bimolecular collision. Upon coming into close contact, the collision complex has to be stabilized in order to yield permanent bond formation between the reactants (see Fig. 1.1 b). This can be achieved by either one of two processes. In a dilute gas a bound←free transition can be achieved by radiative processes, i. e. by absorption or emission of light [40], see chapter 2. So far, photoassociation process are much less well–understood than the reversed process of photodissociation(see below). Only very recently there has been an increasing interest in photoassociation reactions which was stimulated by

new experiments involving collisions of laser–cooled atoms [41]. In particular, the observation and/or control of photoassociation dynamics by short pulse techniques, as well as for any other type of binary reactions, is still at its infancy and the extension of femtochemistry to binary reactions remains a challenge. One aim of the present work is to fill this gap and to demonstrate how pulsed light sources can be used for efficient bound←free population transfer while maintaining a high selectivity with respect to the state of the molecular product. Another aim is to investigate the real–time wavepacket dynamics of these processes and to simulate modern pump–probe experiments.

- At higher particle densities, the photo–induced stabilization of collision complexes competes with the solvent–induced stabilization mediated by collisions with further particles in a solvent environment [42,43,44,45,46]. In chapter 3 of the present work, solvent effects on association reactions shall be investigated ranging between the following too extremes: The notion of the chaperon effect describes a situation where a collision complex is stabilized by transfer of the excess energy to a third (solvent) particle in a three–body collision. In contrast, the cage effect describes a situation where the presence of too many solvent particles can shield the reactants from each other thus leading to a reduced reactivity.

- Finally, chapter 4 of this thesis shall be devoted to the photo–induced breaking of molecular bonds (see Fig. 1.1 c). This class of free←bound transitions is fairly well characterized for simple molecules in the gas phase [47,48]. In the present work we want to investigate solvent effects on the (quantum) dynamics of photodissociation reactions which is at present a very active field of research. One of the most paramount differences between these two extremes can be traced to the solvent cage effect in the latter [49]. Conversely to the above–mentioned cage effect on association reactions, the main effect of the solvent cage on (photo–)dissociation reactions is to delay or to hinder the separation of the photofragments.

In the studies of solvent effects on the making and breaking of molecular bonds in chapters 3 and 4 our special focus shall be on the transition from gas phase to condensed phase dynamics. This is achieved by studying the reaction dynamics of simple diatomics in the environment of rare gas clusters and matrices. The investigation of "microsolvation" in weakly bound clusters is particularly attractive because it allows to vary the size of the solvation environment in a controlled way and to observe solvent effects as a function of the cluster size, from the extreme of a "single atom solvent" up to a crystalline environment [50,51,52,53,54,55,56,57]. Apart from the relatively well–known interactions, the study of van der Waals systems as prototypical systems for solvent effects offer the advantage that the geometry and orientation of reagents are, to a certain extent, restricted. On the other hand, many clusters are very floppy and undergo large amplitude zero–point vibrational motions which can have an enormous effect on the reaction dynamics. Hence, the role of quantum effects can be of great importance.

Chapter 2

Photo–Induced Stabilization of Collision Pairs

2.1 Motivation

When a pair of colliding atoms or molecules comes in close contact they start to interact and their electron clouds are deforming each other. Apart from the attractive or repulsive forces which govern the collision dynamics [10] the changes in the electronic configuration can also include the development of (permanent or transition) multipole moments of the collision complex. This opens the way to manipulation of the collision dynamics by radiative processes. Out of the variety of possible light–assisted (reactive or non–reactive) scattering processes, we want to study only photoassociative collisions in the present work i. e. the process of stabilization of collision complexes to form a stable compound molecule. For the case of an isolated collision complex, e. g. in a rarified gas, this is the only possible stabilization mechanism. Hence, it is of considerable interest for the chemistry of interstellar clouds [58]. This is in contrast to the situation in compressed gases or in condensed phases where typically molecules are formed by three–body collisions, see Sec. 3.

Apart from spontaneous emission of light which is usually much slower than the typical timescale of collision processes [59], there are two different elementary mechanisms for the formation of a stable molecule from a collision pair which is assumed to be initially in the electronic ground state [40].

1. Stimulated emission of one (or more) photons may induce bound←free transitions yielding molecules in the electronic ground state

$$A + B + \hbar\omega \rightarrow AB(v, J) + (n + 1)\hbar\omega \quad . \tag{2.1}$$

   where the excess energy defined as the energy difference between the collision energy E_0 and the energy of the bound state ($E_{v,J}$) is released by emission of n photons, typically in the infrared (IR) regime. Although this process is, at least in principle, fairly simple it has not been systematically investigated prior to the present work. Note that the photoassociation by stimulated emission competes with absorption leading to acceleration of collision pairs in the ground state. This inelastic scattering event which will be termed here as photoacceleration is also known in the literature as translational spectroscopy or as collision induced absorption [60].

2. Absorption of one (or more) photons may electronically excite the (ground state) collision complex. If a bound excited state is present this may lead to stabilization of the collision complex populating ro–vibrational levels of the excited state AB^*

$$A + B + n\hbar\omega \rightarrow AB^*(v, J) \quad . \tag{2.2}$$

   This is the dominant mechanism for visible (VIS) and ultraviolett (UV) photoassociation. In contrast to the situation for the stimulated emission process there is a number of studies of these reactions in the literature. The choice is dictated by the (experimental) requirement that the ground state potential energy curve has to be repulsive (or only weakly attractive) while there must be a strongly bound excited state potential. One class

are collision pairs of alkali atoms where the excited state exhibits a strong, long–range attraction ($\propto R^{-3}$) between a P and a S state atom [61, 62, 63, 64, 65, 66, 41, 67, 68, 69, 70, 71, 72]. The other group of systems for which photoassociation has been thorougly studied are excimer forming diatomics such as rare gas halides [73, 74, 75, 76, 77] and certain metals in the second column of the periodic table [78, 79, 80, 81].

In all the above–mentioned experimental studies continuous wave light sources have been used. Only recently first pioneering steps to investigate the process of photoassociation in real time have been made. To the best of our knowledge there are only very few publications. One series concerns the femtosecond pump–probe spectroscopy of the mercury dimer Hg_2 [82,83,84,85], the other deals with the observation of shape resonances by pulsed spectroscopy for the rubidium dimer Rb_2 [86,87,88] [1]. On the theoretical side, a one–dimensional wavepacket formalism for pump–probe photoassociative spectroscopy has been developed and applied to the case of the excited state of Na_2 [90]. In another study, also the ground state photoassociation via the excited state has been investigated for this system [91]. Another example is a time–dependent study of femtosecond excimer formation for rare gas hydride systems [92]. Note that a generalization to surface photochemistry has been suggested recently: Using IR laser pulses, molecules can be adsorbed to (or desorbed from) metal surfaces [93].

The above–mentioned femtosecond photoassociation spectroscopy experiments on the mercury dimer are among the first truly bimolecular pump–probe experiments [82, 83, 84, 85]. It is noted that these experiments bear some resemblance with "pseudo–bimolecular" experiments, where a molecule in a cluster is photolyzed and a resulting photofragment reacts with another molecule inside the same cluster [50, 94, 52]. This class of experiments has also been extended from energy into time domain [95, 96].

In the present work we want to deal with the quantum dynamics of photoassociative collisions induced by pulsed lasers. Both the ground state process by stimulated emission and the excited state process by absorption of light will be taken into account. More specifically, we want to focus on two different objectives.

1. First of all, we want to optimize the efficiency of the photoassociation process by variation of the shape of the laser pulses used. Morover, we want to reach a high selectivity with respect to the quantum state of the molecular product. This enables us to prepare a molecule in a well–defined electronic, vibrational, and rotational state. Typically this optimization of both efficiency and state–selectivity involves the control of a large number of competing pathways. In the past few years, a variety of different strategies for the optimal population transfer in molecular systems has been developed. One of them is the optimal control theory where pulses of arbitrary shape are optimized [97, 98, 99, 100, 101]. An

[1] Apart from the studies og photoassociation in neutral states, the real time dynamics photoassociative ionization processes has also been studied [89]

alternative is the coherent control technique, where continuous wave light sources with a specific phase relation are used [102, 103, 104, 105]. In the present work this goal is achieved by one (or more) pulses of a simple analytical shape whereby we are optimizing the parameters of simple analytic pulse shapes such as length, amplitude, frequency, and polarization of the laser pulses. This approach builds on earlier work on vibrational excitation [106, 107, 108, 109, 110, 111], isomerization [112, 113, 114], and ground state photodissociation [115, 116, 117, 118, 119] of molecules.

2. The complementary approach to the objective of populating a stationary state with high (close to 100%) selectivity is the preparation of coherence superposition states in modern pump–probe experiments. Typically a first ultrashort laser pulse is used to excite the system. Subsequent to the excitation process, the non–stationary states evolve in time and can be monitored by a second pulse. In this way, the electronic, vibrational, and/or rotational dynamics of a photochemical event can be traced in real time. One specific feature of these experiments is the formation of wavepackets: If the excitation is short enough, i. e. if the energetic band width of the pulse is much larger than the typical spacing of the molecular energy levels, a localized wavepacket can be formed whose center moves like a classical point mass as long as it remains coherent [27, 120, 37].

2.2 Method

2.2.1 General Dynamical Equations

In general the quantum dynamics of molecular processes can be described by the time–dependent Schrödinger's equation

$$i\hbar\frac{\partial}{\partial t}\left|\Psi(t)\right\rangle = \hat{H}^{\mathrm{tot}}\left|\Psi(t)\right\rangle \tag{2.3}$$

where the state of the molecular system is described by the vector $|\Psi(t)\rangle$ which has to be solved subject to some initial condition

$$\left|\Psi(t=0)\right\rangle = \left|\Psi_0\right\rangle \quad . \tag{2.4}$$

The dynamics is governed by the Hamiltonian operator of the system

$$\hat{H}^{\mathrm{tot}} = \hat{H}^{\mathrm{mol}} + \hat{W}(t) \tag{2.5}$$

where $\hat{H}^{\mathrm{mol}}$ represents the time–independent Hamiltonian of the isolated molecule and the time–dependent part $\hat{W}(t)$ describes the interaction of the molecule through its electromagnetic moments or polarizabilities with external fields.

The usual approach in quantum chemistry is to write the molecular state vector as a sum of products of nuclear and electronic wave functions

$$\left|\Psi^{\mathrm{mol}}(t)\right\rangle = \sum_i \left|\psi_i^{\mathrm{nuc}}(t)\right\rangle \otimes \left|\chi_i^{\mathrm{ele}}\right\rangle \tag{2.6}$$

where the time–dependence of the total state vector is incorporated in the nuclear vector $|\psi_i^{\rm nuc}(t)\rangle$ only and where the summation extends over all electronic states $\left|\chi_i^{\rm ele}\right\rangle$. Inserting this approach into the Eq. (2.3) and left–multiplying by an electronic state $\left|\chi_{i'}^{\rm ele}\right\rangle$ eliminates the electronic degrees of freedom and leads to coupled equations for the time–dependent nuclear state vectors

$$i\hbar\frac{\partial}{\partial t}\left|\psi_i^{\rm nuc}(t)\right\rangle = \left[\hat{T}^{\rm nuc} + V_i^{\rm nuc}\right]\left|\psi_i^{\rm nuc}(t)\right\rangle + \sum_{i'}\hat{W}_{ii'}^{\rm nuc}(t)\left|\psi_{i'}^{\rm nuc}(t)\right\rangle \quad . \tag{2.7}$$

Here $\hat{T}^{\rm nuc}$ represents the kinetic energy of the nuclear motion. We are using an electronically adiabatic representation ($V_{ii'}^{\rm nuc} = 0\,\forall\, i \neq i'$) where $V_i^{\rm nuc} = V_{ii}^{\rm nuc}$ is the potential energy of the nuclei. Note that in the framework of the Born–Oppenheimer approximation kinetic energy couplings between different electronic states have been neglected ($\hat{T}_{ii'}^{\rm nuc} \approx 0$) [121]. Hence, the only terms coupling the nuclear dynamics in the different electronic states are the matrix elements of the coupling to the external fields

$$\hat{W}_{ii'}^{\rm nuc}(t) = < \psi_{i'}^{\rm ele}\left|\hat{W}(t)\right|\psi_i^{\rm ele} > \quad . \tag{2.8}$$

where the scalar product is over the electronic degrees of freedom. In summary we have to solve dynamical equations (2.7) for the nuclei under the influence of external fields. Because the dependence on the electronic coordinates has been eliminated the upper index "nuc" will be dropped in the following. The potential energy functions V_i and the matrix elements of the interaction functions $\hat{W}_{ii'}(t)$ can be derived by solving the time–independent Schrödinger's equation for the electrons using quantum chemical techniques typically based on Hartree–Fock calculations or density functional methods. In the present work, we use both *ab initio* and experimental results for the potential and dipole functions (*vide infra*).

2.2.2 Dynamical Equations for a Diatomic System

For a diatomic system the dynamical equations (2.7) can be further simplified. Using a position space representation for the state vectors, and separating the relative motion of the two nuclei from their center of mass motion, we arrive at

$$\begin{aligned} i\hbar\frac{\partial}{\partial t}\psi_i(\vec{r},t) &= \left[-\frac{\hbar^2}{2m}\Delta_{\vec{r}} + V_i(\vec{r})\right]\psi_i(\vec{r},t) \\ &+ \sum_{i'}\hat{W}_{ii'}^{\rm nuc}(\vec{r},t)\psi_{i'}(\vec{r},t) \end{aligned} \tag{2.9}$$

where the expression $m = M_1M_2/(M_1+M_2)$ for the reduced mass has been used. Next we use the standard technique to reduce the three–dimensional equation to a set of coupled one–dimensional equations. This is accomplished by using spherical coordinates r, Θ, Φ and expanding the angular part of the wavefunction in spherical harmonics

$$\psi_i(\vec{r},t) = \sum_{J=0}^{\infty}\sum_{M=-J}^{J}\frac{\phi_{iJM}(r,t)}{r}Y_{JM}(\Theta,\Phi) \tag{2.10}$$

where the functions $\phi_{iJM}(r,t)$ are radial wavefunctions for the electronic state e and for the angular momentum state specified by J and M.

Inserting representation (2.10) into the coupled equations (2.9) finally yields the dynamical equations for the radial wavefunctions $\phi_{iJM}(r,t)$

$$\begin{aligned} i\hbar\frac{\partial}{\partial t}\phi_{iJM}(r,t) &= \left[\hat{T}+V_{iJ}^{\rm eff}(r)\right]\phi_{iJM}(r,t) \\ &+ \sum_{i'}\sum_{JM} W_{iJM,i'J'M'}(r,t)\,\phi_{i'J'M'}(r,t) \end{aligned} \tag{2.11}$$

where the kinetic energy of the radial motion is represented by $\hat{T}=-\frac{\hbar^2}{2m}\frac{\partial^2}{\partial r^2}$ The following expressions for the matrix elements of the potential energy and the interaction operator have been used

$$\int d\Omega Y_{JM}^*(\Theta,\Phi)W_{ii'}(r,\Theta,\Phi,t)Y_{J'M'}(\Theta,\Phi) =: \hat{W}_{iJM,i'J'M'}(r,t) \tag{2.12}$$

$$\int d\Omega Y_{JM}^*(\Theta,\Phi)\left[V_i(r)+\frac{\hat{J}^2}{2mr^2}\right]Y_{J'M'}(\Theta,\Phi) =: V_{iJ}^{\rm eff}(r)\delta_{J,J'}\delta_{M,M'} \tag{2.13}$$

where central forces and potentials $V_i(r=|\vec{r}|)$ are assumed and where we have defined effective potential curves as the sum of the interaction potential $V_i(r)$ and the kinetic energy associated with the angular motion (centrifugal energy)

$$V_{iJ}^{\rm eff}(r)=V_i(r)+\frac{J(J+1)\hbar^2}{2mr^2} \tag{2.14}$$

Note that the effective potential matrix elements are diagonal in i and in J and that there is no M dependence because of the spherical symmetry of the potential function.

In the next subsection we will specify the interaction operator $\hat{W}(t)$ and consider the specific nature of its matrix elements (2.12). The following three subsections present different techniques to solve the coupled equations and give details on the initial states.

2.2.3 Interaction Operator

The interaction between the molecule and an external electromagnetic wave is treated here in the framework of the usual semiclassical dipole approximation [122]

$$\begin{aligned} \hat{W}_{ii'}^{\rm dip}(\vec{r},t) &= -\vec{\mathcal{E}}(t)\cdot\vec{\mu_{ii'}}(r) \\ &= -\mathcal{E}(t)\mu_{ii'}(r)\cos(\gamma_{ii'}) \quad . \end{aligned} \tag{2.15}$$

Here $\mathcal{E}(t)$ stands for the time–dependent electric field component of the electromagnetic wave. The dependence of the dipole moment on the nuclear degrees $\mu_{ii'}(\vec{r})$ of freedom is obtained by integration of the full dipole moment operator over the electronic degrees of freedom, see Eq. (2.8). The diagonal terms ($i=i'$) represent the permant dipole operator of a molecule while the off-diagonal elements ($i\neq i'$) are the transition dipole operators between different electronic

states. The angle γ represents the angle between dipole moment and electric field.

The matrix elements in the spherical harmonic representation (2.12) are given by

$$W^{\rm dip}_{iJM,i'J'M'}(r,t) = -\mathcal{E}(t)\,\mu_{ii'}(r)\,S_{iJM,i'J'M'} \tag{2.16}$$

where the matrix elements $S_{iJMi'J'M'}$ of the direction cosine of the angle $\gamma_{ii'}$ are termed the Hönl–London factors of the respective transition and the dynamical equations in their final form can be written as

$$\begin{aligned} i\hbar\frac{\partial}{\partial t}\phi_{iJM}(r,t) &= \left[\hat{T} + V^{\rm eff}_{iJ}(r)\right]\phi_{iJM}(r,t) \\ &- \mathcal{E}(t)\sum_{i'}\mu_{ii'}(r)\sum_{JM} S_{iJM,i'J'M'}\,\phi_{i'J'M'}(r,t) \quad . \end{aligned} \tag{2.17}$$

In the present work we always assume the electric field to be linearly polarized along the z–direction. Then the Hönl–London factors for a parallel transition ($\mu_{ii'} \parallel \mathcal{E}$, $\gamma_{ii'} = 0$) reduce to an especially simple form [123]

$$\begin{aligned} S_{JM,J'M'} &= \int_0^{\pi}\sin\Theta d\Theta\int_0^{2\pi} d\Phi Y^*_{JM}(\Theta,\Phi)\,\cos\Theta\,Y^*_{JM}(\Theta,\Phi) \\ &= \sqrt{\frac{(J-M)(J+M)}{(2J-1)(2J+1)}}\delta_{J,J'+1}\delta_{M,M'} \\ &+ \sqrt{\frac{(J-M+1)(J+M+1)}{(2J+1)(2J+3)}}\delta_{J,J'-1}\delta_{M,M'} \end{aligned} \tag{2.18}$$

Hence, only two terms in the summation over J' in (2.17) have to be taken into account ($\Delta J = \pm 1$) and the summation over M' is completely eliminated ($\Delta M = 0$) which greatly reduces the computation effort.

For the time–dependence of the electric field $\mathcal{E}(t)$ we assume a modulated oscillation of the form

$$\mathcal{E}(t) = \mathcal{E}_0 g(t) cos(\omega t) \tag{2.19}$$

where $\mathcal{E}_0$ and ω give the amplitude and the carrier frequency of the pulse, respectively. For the envelope we assume $\sin^2$–shaped laser pulses of the form

$$g(t) = \sin^2\left(\frac{\pi(t-\delta t)}{\tau}\right), \quad \delta t \le t \le \tau + \delta t \tag{2.20}$$

with a pulse duration $\tau = 2T_p$ and a time delay δt. This pulse shape is qualitatively very similar to a Gaussian pulse shape with an FWHM of T_p but offers the advantage of a well–defined duration of the pulse [106].

2.2.4 Grid Representations

Perhaps the most intuitive description of quantum dynamics is achieved by solution of the time–dependent Schrödinger's equation in a coordinate space representation [124,34,15]. Present standard techniques are based on an equidistant grid representation of wavefunctions in coordinate space and rely on the

use of fast Fourier transforms (FFT) for the evaluation of the kinetic energy operation. In this way both the potential and kinetic energy operator can be evaluated in a representation where they are diagonal. There is a rich literature of applications of these class of methods on problems of vibrational wavepacket dynamics, reactive scattering, and also photodissociation which is the subject of Part II of he present work, see also [34, 15, 37]

In the context of the present work we have to solve the coupled time–dependent Schrödinger's equations (2.11) for the radial wavefunctions $\phi_{iJM}(r,t)$ under the influence of a time–dependent Hamiltonian (2.5). This is achieved by a time discretization with time steps Δt which have to be chosen short enough such that the time–dependence of the interaction operator can be neglected. Then the time evolution (2.3) can be simply written as

$$|\Phi(t+\Delta t)\rangle = \exp\left[-i(\hat{T}+V^{\rm eff}+\hat{W})\Delta t/\hbar\right]|\Phi(t)\rangle \tag{2.21}$$

where the vector Φ is composed of all the radial functions ϕ_{iJM}. and long time propagation can be realized by repeatedly applying the short time propagator. The evaluation of the exponentiation is carried out by splitting the exponent into its individual components [29, 125]. Note that the method proposed in Ref. [126] can be generalized to coupled equations without having to diagonalize the matrix represention at every timestep [127].

Typically, in time–dependent quantum calculations of reactive scattering events localized wavepacket are used as initial states [14]. Here we use a Gaussian–type packet of the form

$$\phi_{iJM}(r,t=0) = \left(\frac{2}{\pi a^2}\right)^{1/4} \exp\left[ik_0 r - \left(\frac{r-r_0}{a}\right)^2\right] \quad , \tag{2.22}$$

The initial momentum $< \ k \ >= k_0 < 0$ of the incident wavepacket corresponds to a relative collision energy of

$$E_0 = \frac{\hbar^2}{2m}(k_0^2 + 1/a^2) \quad . \tag{2.23}$$

Our choice of the width parameter a is determined by the following considerations. On the one hand, the momentum (and energy) uncertainty $1/a$ should be relatively small so that our results extrapolate well to the case of a free scattering wave. On the other hand, the position uncertainty $a/2$ should be not too large in order to permit efficient manipulation by very short laser pulses. Here we typically use a value of $a = 10a_0$. Accordingly, the initial position of the wavepacket $< \ r \ >= r_0$ has to be large enough so that at $t = 0$ the collision partners do not yet interact with each other. Such a wavepacket can be realized e. g. in photochemical experiments utilizing van der Waals precursor complexes [50, 94, 52].

2.2.5 Eigenstate Representations

The more conventional alternative is to represent the radial wavefunctions in an eigenstate basis of bound and free eigenfunctions $|\chi_{inJM}(r)\rangle$ of the diagonal

part of the effective Hamiltonian of Eq. (2.17) where n represents a (discrete) vibrational quantum number v or a (continuous) wavenumber k, respectively

$$\left[-\frac{\hbar^2}{2m}\frac{\partial^2}{\partial r^2} + V_{iJ}^{\rm eff}(r)\right] \chi_{inJM}(r) = E_{inJM}\,\chi_{inJM}(r) \tag{2.24}$$

where the energies E_{inJ} are independent of the quantum number M because of the spherical symmetry of the effective Hamiltonian.

Using this basis, the radial wavefunctions $\phi_{iJM}(r,t)$ can be written as

$$\phi_{iJM}(r,t) = \sum\!\!\!\!\!\!\int_n c_{inJM}(t) \exp\left[-iE_{inJ}t/\hbar\right]\, \chi_{inJM}(r) \tag{2.25}$$

where the summation extends over all vibrational states v and the integration extends over all scattering states with wavenumber k. In our simulations bound state wavefunctions are obtained using a Fourier grid Hamiltonian method [128, 129], while free scattering functions are obtained by integrating numerically starting from the classically forbidden region ($r \to 0$) outwards ($r \to \infty$) using a Bulirsch–Stoer method [130].

Inserting representation (2.25) into the coupled Schrödinger's equations (2.17) and left–multiplying with an eigenstate yields a coupled system of integro–differential equations (IDEs) for the time–dependent coefficients c_{inJM} in the representation in the basis introduced above

$$\begin{aligned} i\hbar\frac{\partial}{\partial t}c_{inJM}(t) &= \sum_{i'} \sum\!\!\!\!\!\!\int_{n'} \sum_{J'M'} W_{inJM,i'n'J'M'} \\ &\times\; c_{i'n'J'M'}(t)\, \exp\left[i(E_{inJ} - E_{i'n'J'})t/\hbar\right] \end{aligned} \tag{2.26}$$

where the numbers $W_{inJM,i'n'J'M'}$ are the matrix elements of the interaction operator (2.12) in the radial basis

$$W_{inJMi'n'J'M'} = \int dr\, \chi_{inJM}(r)\, W_{iJM,i'J'M'}(r)\, \chi_{i'n'J'M'}(r) \quad . \tag{2.27}$$

Finally, we substitute the special form of the semiclassical dipole operator (2.16) and obtain in analogy to (2.17)

$$\begin{aligned} i\hbar\frac{\partial}{\partial t}c_{inJM}(t) &= -\mathcal{E}(t) \sum_{i'} \sum\!\!\!\!\!\!\int_{n'} \sum_{J'M'} \mu_{inJM,i'n'J'M'}\, S_{iJM,i'J'M'} \\ &\times\; c_{i'n'J'M'}(t)\, \exp\left[i(E_{inJ} - E_{i'n'J'})t/\hbar\right] \end{aligned} \tag{2.28}$$

where the matrix elements of the dipole operator have been used.

$$\mu_{inJM,i'n'J'M'} = \int dr\, \chi_{inJM}(r)\, \mu_{in,i'n'}(r)\, \chi_{i'n'J'M'}(r) \tag{2.29}$$

the squares of which are the Franck–Condon factors. The integro–differential equations (2.28) offer a simple and interpretation of the dependence of the tansition probability $inJM \to i'n'J'M'$ on internal (molecular) and external (laser pulse) parameters. The corresponding changes in the populations $|c_{inJM}(t)|^2$ of a state $|inJM\rangle$ are proportional to the following quantities:

1. The Franck–Condon factor$|\mu_{in,i'n'}(r)|^2$ which is determined by the overlap of the radial wave functions with each other and with the radial dipole moment function,

2. The Hönl–London factors $|S_{iJM,i'J'M'}|^2$ which, for a given light polarization, determine the transition rules for a $JM \rightarrow J'M'$ rotational transition for a simultaneous electronic transition $i \rightarrow i'$ (where simplifications may apply, see e. g. Eq. (2.18) for a parallel transition), and

3. the laser intensity which is proportional to $\mathcal{E}^2(t)$.

In contrast to the grid representation discussed in the previous subsection, the initial state is not required to be limited in spatial extension. Instead it is advantageous to assume the initial state to be a scattering state which is a continuum solution of the time–independent Schrödinger's equation (2.24) in the absence of an external field. Furthermore, the choice of an eigenfunction of the energy as an initial state provides a realistic description of the situation in experiments with high quality atomic/molecular beams or with laser–cooled atoms where the velocity spread can be extremely low.

Moreover, it is noted that due to the well–known problems with the normalization of the continuum solutions of (2.24), absolute efficiencies for a photoassociation process cannot be given. This is possible only for the wavepacket picture of the previous section. Instead, we give cross sections which are defined in analogy to the standard definitions in scattering theory [10, 131].

These cross sections are defined as the quantum mechanical probability of finding the collision partners, which were initially prepared in a scattering state i, in a final state f. This probability per unit time and per volume in momentum space is the product of the incoming probability current $J_i = \hbar k/\mu$ and a time–dependent partial inelastic cross section for the transition $f \leftarrow i$ (for $f \neq i$). Therefore we can define $d\sigma_{fi}(t)/d\Omega$ (with the dimension of an area),

$$\frac{d\sigma_{fi}(t)}{d\Omega} := \frac{1}{|J_i|} \frac{d}{dt} |c_f(t)|^2 \quad . \tag{2.30}$$

For experiments with pulsed light sources it is practical to define a time–averaged cross section with respect to the duration of the laser pulse

$$\frac{d\sigma^p_{fi}}{d\Omega} = \frac{1}{2T_p} \int_0^{2T_p} \frac{d\sigma_{fi}(t)}{d\Omega} dt = \frac{|c_f(t = 2T_p)|^2}{2T_p|J_i|} \quad . \tag{2.31}$$

For more details, see A.4

2.2.6 Perturbation Theory

In the weak field limit the integro–differential equations (2.28) can be simplified substantially if time–dependent first order perturbation theory is applied [90, 132]. Assuming the light–matter interaction to be very weak, the population transfer is negligible and the coefficients $c_{inJM}(t)$ can be replaced by their initial

values. Upon insertion of the pulse shape (2.20) one obtains (assuming $\delta t = 0$)

$$\begin{aligned}\frac{\partial}{\partial t}c_{inJM}(t) &= -\frac{\mathcal{E}_0}{2i\hbar}\sum_{i'}\int\!\!\!\!\!\!\sum_{n'}\sum_{J'M'}\mu_{inJM,i'n'J'M'}\,S_{iJM,i'J'M'} \\ &\times \sin^2\left(\frac{\pi t}{2T_p}\right)c_{i'n'J'M'}(t=0) \\ &\times \left[\exp(i\Omega^+_{inJ,i'n'J'}t)+\exp(i\Omega^-_{inJ,i'n'J'}t)\right] \end{aligned} \tag{2.32}$$

where the angular frequencies Ω^+ and Ω^- denote the detuning of the carrier frequency ω of the laser pulse with respect to the Bohr frequency of the transition $inJ \rightarrow i'n'J'$ for stimulated emission ang for absorption, respectively.

$$\Omega^{\pm}_{inJ,i'n'J'} = \pm\omega + \frac{E_{inJ}-E_{i'n'J'}}{\hbar} \quad . \tag{2.33}$$

Now it is straight-forward to integrate the decoupled integro–differential equations (2.32) over the duration of the laser pulse $[0,\tau]$, see Ref. [90]

$$\begin{aligned}c_{inJM}(t=2T_p) &= -\frac{\mathcal{E}_0\,T_p}{2\hbar}\sum_{i'}\int\!\!\!\!\!\!\sum_{n'}\sum_{J'M'}\mu_{inJM,i'n'J'M'}\,S_{iJM,i'J'M'} \\ &\times c_{i'n'J'M'}(t=0) \\ &\times \left[G(\Omega^+_{inJ,i'n'J'}\,T_p)+G(\Omega^-_{inJ,i'n'J'}\,T_p)\right] \end{aligned} \tag{2.34}$$

where the functions G are essentially identical to the Fourier transforms of the $\sin^2$–shaped laser pulses

$$G(\Omega^{\pm}\,T_p) = \int_{t=0}^{2T_p} dt\,\sin^2\left(\frac{\pi t}{2T_p}\right)\exp(i\Omega^{\pm}t) = \frac{i\,[\exp(iX)-1]}{2\Omega^{\pm}\,[(X/2\pi)^2-1]} \tag{2.35}$$

for the argument $X = \Omega^{\pm}_{inJ,i'n'J'}\,T_p$.

It is noted that the coefficients $c_{inJM}(t)$ are constant after the end of the laser pulse and the further dynamics is simply determined by the natural time–evolution of the the wavefunctions as given in Eq. (2.25).

As a next step we give equations for a specific initial state. First we assume the reactants to be in an electronic state uniquely corresponding to the molecular state i_0. Then we follow the standard approach of scattering theory [10] and assume the initial state to be a scattering state which asymptotically approaches an incoming plane wave and outgoing spherical waves. Assuming an energy of $E_0 = \hbar^2 k_0^2/(2m)$ and the propagation of the plane wave to be along z, we obtain the following initial values for the expansion coefficients

$$c_{i_0k_0JM}(t=0) = \frac{1}{(2\pi)^{3/2}}\,\frac{1}{k_0}\,i^J\,\sqrt{4\pi(2J+1)}\,\exp(i\delta_{i_0J})\,\delta_{M,0} \quad . \tag{2.36}$$

The scattering phases δ_{iJ} are obtained by numerically integrating the time–independent Schrödinger's equation (2.24) for the state $i = i_0$ and fitting the solution in the asymptotic region to the form $\sin(k_0 r - J\pi/2 + \delta_{i_0J})$. By virtue of the resonance approximation of neglecting Ω^- or Ω^+ for stimulated emission or

for absorption, respectively, we arrive at the final results: For photoassociative bound←free transitions by stimulated emission ($i \leq i_0$ e. g. in the electronic ground state), the coefficients for a bound state at the end of the laser pulse are given by

$$\begin{aligned} c_{ivJM}(2T_p) &= -\sqrt{\frac{4\pi}{(2\pi)^3}}\,\frac{\mathcal{E}_p T_p}{2\hbar}\,\frac{1}{k_0} \\ &\times \sum_{J'} \mu_{ivJM,i_0k_0J'0}\, S_{iJM,i_0J'0} \\ &\times i^{J'}\, e^{i\delta_{i_0J'}}\, G(\Omega^+_{ivJ,i_0k_iJ'} T_p) \end{aligned} \tag{2.37}$$

For photoassociative transitions by absorption ($i > i_0$, e. g. from free ground state collision pairs to a bound level of the electronically excited state) Ω^+ has to be replaced by Ω^-. Similar expressions can also be derived for the photoassociation process, see A.4.

Finally, the regime of validity of our perturbation based *ansatz* has to be discussed. In Fig. 5 of A.4 this is demonstrated for the case of the HCl photoassociation in the electronic ground state. Even for the case of a bound←quasibound transition, for which the Franck–Condon factor is especially large (see Sec. 2.3.6), there is very good agreement between the numerically exact and the perturbative photoassociation probability up to a pulse intensity of 10^{13} W/cm^2. Beyond this limit, the simple two– or three state models are not sufficient, anyway, and higher electronic excitations and ionization starts to play an important role.

2.3 State–Selectivity

2.3.1 Model Systems

In the present work on state–selective photoassociation, we use two simple diatomic hydrides as model systems. Note that the choice of this class of molecules is motivated by the following reason. Apart from their obvious simplicity, the large values of both vibrational frequency and rotational constant result in a relatively low density of states and hence in relatively strong quantum effects.

Hydroxyl Radical

The first model system we are using in our investigations (A.2, A.3) is the OH radical which is often used as a model for the local OH bond e. g. in a water molecule [133, 134]. Furthermore, this choice is motivated by the existence of a relatively low–lying bound excited state $A^2\Sigma^+$ ($i = g$) the well of which is below the dissociation limit of the electronic ground state $X^2\Pi$ (i=e), see Fig. 2.1 (a). Based on the model of Ref. [135], we rely on high quality *ab initio* data for the potential energy curves. Here extended Rydberg functions [136] are fitted to the data points of Ref. [137]. There are 17 and 11 bound vibrational levels for the electronic ground and the excited state, respectively. For the permanent dipole functions of ground ($\mu_g(r)$) and excited ($\mu_e(r)$) electronic state we use *ab initio*

data from the literature [138, 139], see also Fig. 2.1 (b). Also the transition dipole moment ($\mu_{ge}(r)$) coupling the dynamics in the ground and excited state is adapted from first principles calculations [140, 137]. As we will show later it is very important that $\mu_g(r)$ and $\mu_e(r)$ are parallel to the molecular axis while $\mu_{ge}(r)$ is perpendicular.

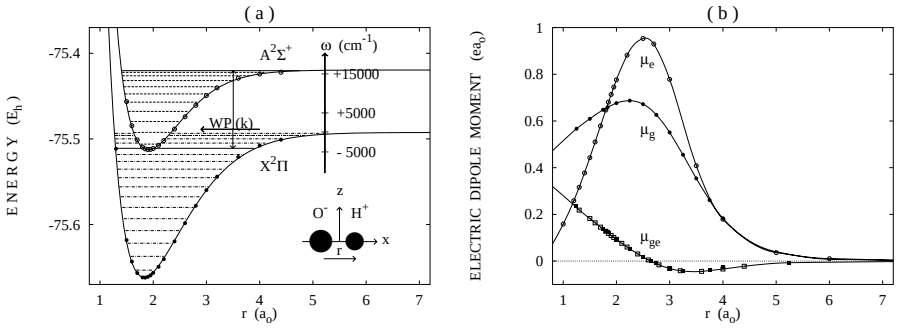

Figure 2.1: (a) Potential energy curves V_g ($X^2\Pi$) and V_e ($A^2\Sigma^+$) for the two lowest electronic states of the hydroxyl (OH) molecule. The curves represent extended Rydberg functions fitted to the *ab initio* data points of Ref. [137]. (b) Ab initio data for the permanent dipole functions of ground state μ_g (solid circles [138]) and excited state μ_e (open circles [139]), and for the transition dipole moment μ_{ge} (solid squares [141] and open squares [137]). From A.3

Note that in our first studies of the ground state photoassociation of OH (A.1 and A.2) we used simple model functions for potential energy and permanent dipole moment. For the former, we used a Morse potential

$$V_g(r) = D\left[e^{-\beta(r-r_0)} - 1\right]^2 - D \tag{2.38}$$

with a dissociation energy $D = 43763$ cm^{-1}, an equilibrium bond length $r_0 = 96.36$ pm, and a range parameter $\beta = 22.47$ nm^{-1} determining the steepness of the potential well [142]. The dipole moment function is represented by a Mecke function [143]

$$\mu_g(r) = q\, r\, e^{-r/r^*} \tag{2.39}$$

with parameters $q = 1.634|e|$ and $r^* = 60$ pm representing OH bonds in the water molecule.

These model functions allow the analytic calculations of dipole matrix elements for bound←bound and bound←free transitions at least for a rotationless model, see our work on photodissociation in the electronic ground state [117]. This allows an analytic treatment of the integro–differential equations (IDE, see Eq. 2.28) in the limit of negligible free←free transitions. However, in contrast to photodissociation where free←free transitions are allowed only to second order, this approximation is not justified here because photoassociation and photoacceleration are directly competing with each other (*vide infra*).

Hydrogen Chloride Molecule

In another study (A.4) we use the hydrogen chloride. As in the case of the OH molecule, the HCl potential energy curve can be represented very well by a Morse oscillator (2.38) but with a dissociation energy $D = 37249.2$ cm^{-1}, an equilibrium bond length $r_0 = 127.5$ pm, and a steepness parameter $\beta = 18.68$ nm^{-1} [144] whereas the dipole moment function is adapted from *ab initio* data published in the literature [145]. Although they are qualitatively very similar to those for the OH radical there is a very important difference. Because there is no other low–lying bound state, electronic transitions can be safely neglected because they would require very high multi–photon transitions for the IR radiation considered here.

2.3.2 Populations and Selectivity

Time–dependent populations of bound states are obtained in two different ways. For the eigenstate representation of Sec. 2.2.5 they are simply defined by $P_{ivJM}(t) = |c_{ivJM}(t)|^2$. For the grid representations proposed in Sec. 2.2.4 populations are obtained by projection of the non–stationary wavefunctions $\phi_{iJM}(r,t)$ on the n_i bound vibrational states of the respective potential

$$P_{v_i}(t) = \sum_{JM} \left| \int dr\, \chi_{ivJM}(r)\, \phi_{iJM}(r,t) \right|^2, \qquad 0 \le v_i \le (n_i - 1) \quad . \tag{2.40}$$

Accordingly, the total population of all the bound states of the potential well and the total population of continuum states are given by

$$\begin{aligned} P_{\mathrm{well_i}}(t) &= \sum_{v_i=0}^{n_i-1} P_{v_i}(t) \\ P_{\mathrm{cont_i}}(t) &= \sum_{JM} \int_0^\infty |\phi_{iJM}(r,t)|^2\, dr - P_{well_i}(t) \end{aligned} \tag{2.41}$$

for each electronic state i. The vibrational state selectivity

$$S_{v_i}(t) = P_{v_i}(t) / P_{\mathrm{well_i}}(t) \tag{2.42}$$

is used to characterize the selectivity of preparation of molecules in a specific vibrational state. In Sec. 2.3.6 we will also consider rotational state selectivity which is be defined in analogy to (2.40) but omitting the sum over rotational states.

2.3.3 Initial States

Collision Energy

As has been detailed in the Introduction, a photodissociation reaction is the reversed process of a photoassociative collision. Therefore, it can be very instructive to consider the light–induced bond breaking before actually studying the process of bond making. This is especially useful for the following two reasons which are connected with the difficulties of using wavepackets as initial state:

1. The final state of a dissociation reaction initiated by a pulsed light source can provide important information on the initial state of an association reaction initiated by the same pulses.

2. The study of the dependence of a photodissociation event on the initial state can be used to learn about the efficiency of a photoassociation reaction as a function of the final (bound) state.

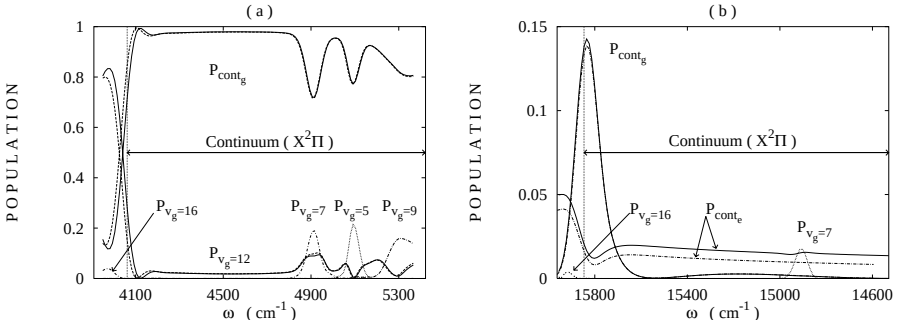

Figure 2.2: Bound and continuum state population after excitation of OH with an IR laser pulse ($\tau = 0.5$ ps, $\mathcal{E}_0 = 0.07E_h/(ea_0)$) for different initial states. (a) $v_g = 12$, electronic ground state. (b) $v_e = 10$, top level of the excited electronic state (note the reversed abscissa). Solid curves for synchronous x and z polarization, dashed curves in part (a) for x polarization, dot–dashed curves in part (b) for z polarization. From A.3

As a first example, let us consider the photodissociation of OH by an ultrashort IR laser pulse of duration $\tau = 0.5$ ps and amplitude $\mathcal{E}_0 = 0.07E_h/(ea_0)$. We use the *ab initio* potential energy and (transition) dipole moment functions shown in Fig. 2.1.

For the time being, we restrict ourselves to a rotationless model. We choose the $v_g = 12$ vibrational level of the electronic ground state. This choice of a relatively high initial state already implies our experiences in ground state vibrational excitation and photodissociation dynamics. On the one hand, the Franck–Condon factors for photodissociation of lower vibrational states are very low, on the other hand vibrational pre–excitation of the very highest vibrational levels is not very state–selective any more [117].

Fig. 2.2 (a) shows our results for the photodissociation probability versus frequency of the laser pulse. Beyond the dissociation threshold there is a sudden increase of continuum population at the end of the laser pulse ($P_{cont,g}$) at $\omega \approx 4050$ cm^{-1}. The dissociation yield remains roughly constant up to $\omega \approx 4800$ cm^{-1}. Beyond this frequency there are dips in this curve in the vicinity of resonance frequencies of down–transitions. At the same time there is a buildup of population in lower vibrational levels caused by stimulated emission of one ($v_g = 9$), two ($v_g = 7$) or three ($v_g = 5$) photons. The implications of the presence of these bound←bound transitions with respect to the ground state photoassociation dynamics are clear. The one–photon processes from a continuum state down to the $v = 12$ target level have to compete with higher–order

processes down to lower levels. This will be elucidated in detail in subsection 2.3.4 on vibrational state selectivity.

Our results for dissociation of electronically excited OH molecules are illustrated in Fig. 2.2 (b) where we choose the top vibrational level $v_e = 10$ as initial state. Assuming a light polarization perpendicular to the molecular symmetry axis, electronic transitions can yield ground state atoms $O(^3P) + H(^2S)$ by stimulated emission. The yield of this dissociation reaction shows two main features. First, there is a narrow, sharp peak centered at $\omega \approx 15,835$ cm^{-1}. Second, there is a much lower and very broad signal around $\omega \approx 15,200$ cm^{-1}. The efficiency of these processes is much lower than for the electronic ground state. The maximum yield for the first peak is only 14%, the yield for the blurred peak is only in the range of 2%. This is caused by the weak transition dipole moment function, in particular by the root of $\mu_{ge}(r)$ at $r = 2.64a_0$ (see Fig. 2.1 (b). It is mentioned that for all lower vibrational states ($v_e < 10$) this yield is even much lower, hence we consider only the top level.

The corresponding photofragment energies can be determined from the excess energy beyond the respective dissociation threshold which are also marked in Fig. 2.2. This helps us to predict the dependence of the photoassociation yield on the energy of an incoming wavepacket. Except for the vicinity of multi–photon process, the yield of the ground state reaction can be expected to be a smooth function of the scattering energy, while the excited state process will be reasonably effective only for $0 < E_0 < 100$ cm^{-1} (sharp peak) and for $400 < E_0 < 1200$ cm^{-1} (broad peak). Hence, we will consider two cases in the following, i. e. very slow collision partners with $k_0 = -0.7a_0^{-1}$ ($E_0 = 31.1$ cm^{-1}) and moderately fast collision partners with $k_0 = -3.5a_0^{-1}$($E_0 = 777.7$ cm^{-1}). As will be discussed later, this strong sensitivity of the photoassociation on the collision energy can be used to control the electronic branching ratio in OH photoassociation reactions.

Relative Timing

Another important issue when dealing with time–dependent wavepacket and time–dependent light sources is the relative timing of the collision event versus the onset of the laser pulse. First of all, the parameters of the initial wavepacket (Eq. 2.22) have to be specified. Once the parameters of the initial wavepacket are fixed, the optimal timing can be estimated most naturally by studying the reference case of elastic scattering of a wavepacket, i. e. without external fields. As the collision partners are approaching each other, they start to interact with each other through the potential energy function. After some time a part of the wavepacket is still ingoing while another part has already been reflected by the repulsive part of the potential and interferes with the former one (see Fig. 1 of A.1). This situation leads to an interference pattern similar to a standing wave which can be considered as a transition state for photoinduced manipulation of a collision pair. The time from the buildup to the decay of this interference suggests a natural timescale for the duration of laser pulses. In the present work, we use $\tau = 1.5$ ps and $\tau = 0.5$ ps for the slow and fast collisions, respectively.

2.3.4 Vibrational State Selectivity

Frequency Dependence of Photoassociation

Fig. 2.3 (a) shows the Morse potential representing the electronic ground state of the OH molecule together with a few high vibrational states. For the while being, we will restrict ourselves to a 1–D (rotation–less) model. This restriction will be lifted later, see Sec. 2.3.6. The most obvious parameter which can be varied to control the dynamics of the photoinduced inelastic collision event is the frequency ω of the laser pulse. For simplicity let us first assume all other parameters to be fixed and let us restrict ourselves to consideration of the ground electronic state only. We choose the higher of the two collision energies ($E_0 = 777.7$ cm^{-1}, $k_0 = -3.5$ a$_0^{-1}$), a pulse length $\tau = 0.5$ ps and a fixed maximum field amplitude $\mathcal{E}_0 = 25.71$ GV/m. The diagram 2.3 (a) shows possible transitions that can be induced by the interaction of the collision pair with infrared laser pulses ($2400 < \omega < 3900$ cm^{-1}). We can see that for this spectral range bound←free transitions by stimulated emission of one ($v = 16, 17$), two ($v = 13, 14$), or three ($v = 11$) photon transitions are eligible. At the same time, emission of one or more photons can lead to acceleration of the (inelastically) scattered atoms.

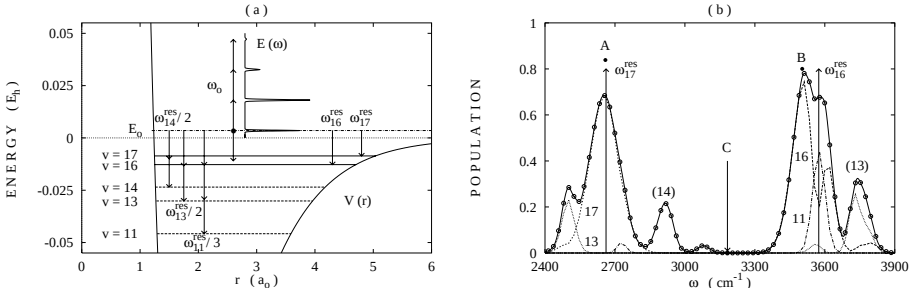

Figure 2.3: Frequency dependence of the ground state photoassociation and photoacceleration. (a) Potential energy curve, free and buond states. The dot–dashed line indicates the energy $E_0 = 777.7$ cm^{-1} of the incoming wavepacket, the vertical arrows show various one– two–, and three photon transitions leading to photoassociation or photoacceleration in the range $2400 < \omega < 3900$ cm^{-1}. (b) Photoassociation spectrum for the same frequency range. The vertical arrows mark the resonance frequencies for one–photon transitions (see text). From A.2

For our model the ideal case of a vibrational state selectivity ($S \approx 100\%$) is realized e. g. for a bound←free transition down to the $v_g = 15$ vibrational level (see A.1). The optimized laser frequency is far off any multi–photon transitions and a vibrational state selectivity of $S \approx 100\%$ is easily achieved ($\omega = 4701$ cm^{-1}, outside the range of Fig. 2.3 (b)). Note that there is a small detuning of $\Omega = +35$ cm^{-1} with respect to the exact energy difference between the initial wavepacket and the $v_g = 15$ state.

Fig. 2.3 (b) illustrates the interplay between one–photon and multi–photon

transitions. For fixed values of k_0, τ and $\mathcal{E}_0$ (see above) the plot shows the total photoassociation probability in the electronic ground state versus carrier frequency ω of the IR laser pulse. First of all, we see that the main peaks in the spectrum correspond to the bound←free transitions down to the $v = 17$ and $v = 16$ state of the Morse oscillator. However, a closer inspection shows the influence of higher–order processes. For the $v_g = 17$ photoassociation the vicinity of the two– ($v_g = 14$) and three–photon ($v_g = 13$) transitions is only marginally felt. In contrast, there is a relatively large detuning Ω between the resonance frequency and the optimal frequency for $v_g = 16$ which is mainly caused by two– ($v_g = 13$) and three–photon ($v_g = 11$) transition.

Population dynamics

The competition of one– and more photon processes is also reflected in the population dynamics induced by the ultrashort laser pulses. This is shown in Fig. 2.4 where the dynamics is illustrated for laser pulses which are optimized for the bound←free transitions down to $v_g = 17$ and $v_g = 16$. The exact values of the parameters are detailed in Ref. A.2.

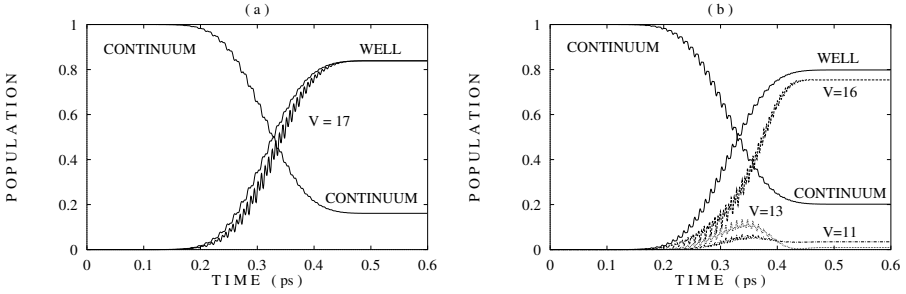

Figure 2.4: Population dynamics of ground state photoassociative collision induced by IR laser pulses. For the exact parameters of the optimized laser pulses, see A.2. Parts (a) and (b) of the figure correspond to the optimized frequencies indicated by the solid circles A and B in Fig. 2.3 (b). From A.2

In the former case, about $P_{cont,g} = 84\%$ of the initial wavepacket can be transferred into bound states of the potential well, see Fig. 2.4 (a). Out of this well population an extremely high fraction of $S_{v_g=17} > 99.9\%$ is found in the $v_g = 17$ at the end of the laser pulse ($t \geq 0.5$ ps). Also at intermediate times, this fraction never drops below 80 to 90%. As can be seen in Fig. 2.4 (b) this situation is different for the photoassociation with the $v_g = 16$ target level. Although the overall efficiency is similar ($P_{cont,g} \approx 80\%$), we find a vibrational state selectivity of only $S_{v_g=16} \approx 90\%$. It is clear that this deterioration is due to the nearby resonance frequencies for two– and three–photon transitions mentioned above. Especially at intermediate times, we have an appreciable fraction of the well population in the $v_g = 13$ and $v_g = 11$ state, the latter one persisting also after the end of the pulse. These near–coincidences of one– and multi(n)–photon processes leading to photoassociation products in the v_{one} or

v_{multi} state, respectively, are characterized by

$$E_0 - E_{v_{one}} \approx (E_0 - E_{v_{multi}})/n \tag{2.43}$$

Of course, these coincidences depend also on the exact choice of the scattering energy. As an example we refer to Fig. 4 of A.2 where a one ($v_g = 12$) and a two ($v_g = 7$) photon transitions are shifted relatively to each other by slight variation of k_0 and where the state selectivity can be brought back to a value very close to 100%.

Competition with Photoacceleration

The process of photoassociation induced by stimulated emission is competing with the process of photoacceleration induced by absorption of one or more photons. The latter process is defined as an inelastic collision where the collision partners are accelerated by the energy absorbed from the electric field of the laser pulse. It is also known as translational spectroscopy or as collision induced absorption [60]. These free←free transitions are most likely when the frequency is sufficiently far from any of the (first or higher order) bound←free transition frequencies, e. g. in the vicinity of region C in Fig. 2.3 (b).

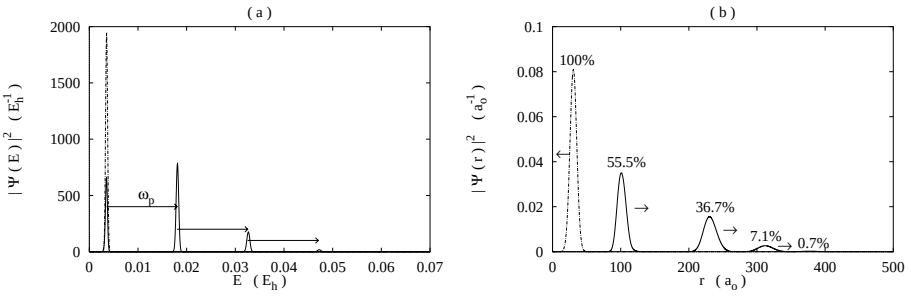

Figure 2.5: Photoacceleration of an OH collision pair in energy (a) and in position (b) space representation. The frequency corresponds to the arrow C in Fig 2.3, the electric field amplitude is $\mathcal{E}_x = 25.71$ GV/m. The dot–dashed curves show the distribution at $t = 0$, the solid curves show the distribution some time after the end of the laser pulse ($t = 1.5$ ps). From A.2

Fig. 2.5 shows an example for free←free transitions. Apart from the buildup of some minor population ($< 1\%$) in the bound states $v_g = 16$ and $v_g = 17$ at intermediate times, the result is a pure free←free transition at the end of the pulse. For the specific laser pulse chosen here we see that about 55% have been scattered elastically. The remaining population has undergone inelastic scattering, with the separation of the peaks in the energy spectrum corresponding to the photon energy. Here up to three photons have been absorbed resulting in accelerations up to ≈ 1 eV. It is noted that the structured spectrum of continuum state exhibits some analogies with above–threshold ionization (ATI) [146] or above–threshold dissociation (ATD) [147, 117]

As has been shown in A.2 the fraction of inelastic scattering can be enhanced to approximately 60% by using higher fields. However, when trying to achieve much higher accelerations there are two principle limitations.

1. In principle, the number of photons absorbed can be enhanced by increasing the amplitude of the pulses. However, this also increases the density of resonances for higher order stimulated emission processes with bound←free transitions leading to photoacceleration.

2. When trying to circumvent this by choosing higher frequencies of the pulses there is a limitation due to the rapidly decreasing matrix elements of the dipole moment operator for free←free transitions which can be qualitatively explained by the energy gap law.

2.3.5 Electronic State Selectivity

Single pulse strategy

As has been mentioned in Sec. 2.3.3 transitions between the continuum of the ground state ($X^2\Pi$) and bound vibrational levels of the excited electronic state ($A^2\Sigma^+$) of the OH molecule are strongly affected by peculiarities of the transition dipole moment function, see Fig. 2.1 (b). In particular, for the collision energies considered here the respective Franck–Condon factors are practically zero for all but the highest level $v_e = 10$ of the excited state. Hence, excited state photoassociation is best achieved using visible laser pulses with carrier frequencies between 15,000 cm^{-1} and 16,000 cm^{-1} .

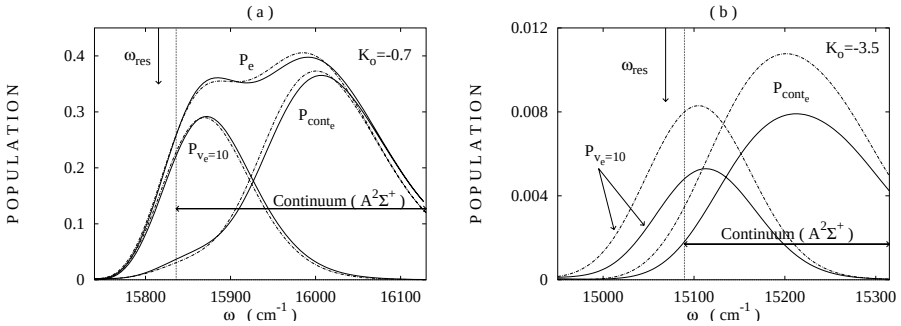

Figure 2.6: Excited state photoassociation of an OH collision pair for low scattering energy ($K_0 = -0.7$ a$_0^{-1}$, $\tau = 1.5$ ps, $\mathcal{E}_0 = 0.16E_h/(ea_0)$) and for high scattering energy ($K_0 = -3.5$ a$_0^{-1}$, $\tau = 0.5$ ps, $\mathcal{E}_0 = 0.18E_h/(ea_0)$). Dot–dashed curves: z–polarization only, solid curves: x and z polarization. From A.3

A typical result is shown in Fig. 2.6. For low collision energies, even a very strong field of $\mathcal{E}_z = 0.16E_h/(ea_0)$ yields a maximum photoassociation probability of only $\approx 30\%$, for the higher collision energy the yield is much lower ($< 1\%$) even for slightly stronger fields. An additional parallel polarization of the laser pulse causes only small frequency shifts in the former case while it causes appreciable changes in the latter case. The decrease of excited state photoassociation

yield for simultaneous x and z polarization might be an indication of free←free or bound←free transitions within the electronically excited state.

Another interesting feature of the spectra of Fig. 2.6 results from the energetic proximity of the top vibrational level ($v_e = 10$) to the dissociation threshold of the $A^2\Sigma^+$ state. At frequencies slightly higher than the maximum of $P_{v_e=10}$ there is another peak in the electronic excitation spectrum indicating the onset of population in the continuum of the $A^2\Sigma^+$ state. This corresponds to re–dissociation of the collision pair with the oxygen atom being electronically excited $O(^1D)+H(^2S)$. Note that the two peaks are partly overlapping so that a population transfer exclusively into the bound states of the electronically excited state is impossible.

The coupling to the electronically excited state has also consequences for the quantum dynamics of the ground state photoassociation process. This has been shown in more detail in A.3 for the region between 4000 cm^{-1} and 5000 cm^{-1} for a simultaneous parallel and perpendicular polarization of the light. Although there is no notable population transfer there are small but distinctive frequency shifts of the peaks. These shifts can be easily explained in a "dressed molecule" picture using light–induced effective potential curves in the presence of a periodic field [148, 149].

Two pulse strategy

The low efficiency of transitions between the continuum of the ground state ($X^2\Pi$) and bound vibrational levels of the excited electronic state ($A^2\Sigma^+$) achieved with a single pulse can be easily remedied by a a two–pulse "dump–pump" strategy. A first, infrared laser pulse ("dump") can be used to accomplish ground state photoassociation as discussed in Sec. 2.3.4. Typically, an efficiency of $\approx 70 \ldots 80\%$ and a very high state–selectivity close to 100% can be achieved. Then a second, visible laser pulse ("pump") is employed to induce a bound←bound transition. The possibility of electronic excitation by use of ultrashort laser pulses has been recently discussed for the same model of the OH molecule [135]. Our results are illustrated in Fig. 2.7. The population transfer to the electronically excited state is close to 100% efficient, however there are losses in the order of 10% due to re–dissociation into the continuum of the $A^2\Sigma^+$ state. Nevertheless, compared with the single–pulse result of Fig. 2.6 (b) the yield of electronically excited OH molecules from a slow OH collision pair ($k_0 = -3.5a_0^{-1}$) has increased by two orders of magnitude.

The "dump–pump" strategy developed in the present work can be regarded as a complementary approach to the work of Vardi et al. on the sodium dimer [91]. In order to achieve photoassociation in the ground state for a homonuclear diatomic with $\mu_g(r) = 0$ these authors suggest a "pump–dump" strategy: First a collision pair is pumped to bound levels of an excited electronic state which is subsequently dumped to a ro–vibrational level of the ground state. The concept of "counter–intuitive" order of the two pulses is not applied in the present work because there is no substantial fluorescence from the intermediate state on the timescales considered here.

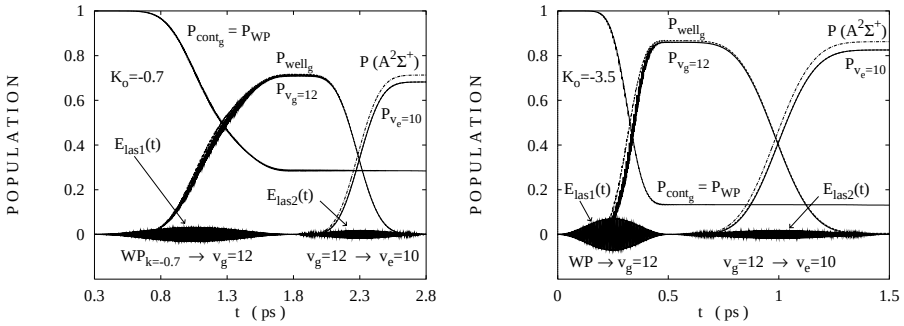

Figure 2.7: Two–pulse strategy for excited state photoassociation of a slow (a) and a fast (b) OH collision pair. The first infrared pulse ("dump") transfers the O + H collision pair to the $v_g = 12$ level, the second visible pulse ("pump") excites the OH molecule to the $v_e = 10$ bound state. From A.3

Conclusions

Apart from the aspect of vibrational selectivity already discussed in Sec. 2.3.4 the results of this section shed light on the question of selectivity of the electronic state of a photoassociation product. This is of particular interest for a molecule like the OH radical where due the presence of a low–lying bound excited state ground and excited state photoassociation can in principle occur in the same frequency range. The results obtained here suggest several ways of controlling the electronic branching ratio of photoassociation reactions for the O + H collision pair.

- Regardless of the laser pulses used, one way to control the electronic branching ratio is given by its dependence on the initial state, i. e. the strong sensitivity on the initial scattering energy. Because excited state photoassociation is only effective for very slow collision energies, this process can be practically excluded for collision pairs with higher initial momenta. However, at low scattering energies both channels are in principle possible.

- Another very simple control mechanism is feasible for experiments with oriented molecules which is due to the different orientation of permanent and transition dipole moments. In this case the electronic branching ratio of the OH photoassociation reaction of oriented molecules can be very easily controlled via the polarization of the light pulses.

- Finally, there is a slightly more sophisticated way to control the branching via the wavelengths of the light pulses. The specific shape of the transition dipole moment function of OH restricts the excited state process to the $v_e = 10$ level and hence to a narrow range of carrier frequencies around $15,700 \ldots 16,100$ cm^{-1}. Since there are no resonances for bound←free transitions in the ground state molecules can be formed only in the excited electronic state. On the other hand, the photon energy

in the low frequency regime eligible for ground state photoassociation ($\omega = 4000 \ldots 5000$ cm^{-1} would suffice only for excited state photoassociation into low vibrational levels v_e for which, however, the Franck–Condon factors are practically zero.

2.3.6 Rotational State–Selectivity

Introduction

All the results on vibrationally and/or electronically state selective photoassociation presented so far have been obtained for a rotation-less model. In the following we want to investigate how the efficiency and the state–selectivity are changed by including rotational effects in our model. In particular, we want to study the possibility of creating molecules in a specific ro–vibrational state (photoassociation) or to prepare a collision pair at a specific energy and angular momentum. Here the ^{1}H^{35}Cl molecule is chosen as a model system. Although qualitatively very similar to the OH radical, this choice simplifies our work because there are no other low–lying bound electronic states apart from the ground state ($X^1\Sigma$).

Quasi-bound States

For non–zero angular momenta J, there is also a qualitatively new feature, i. e. a local maximum (centrifugal barrier) of the effective potential energy curves (2.14) at relatively large distances which separates the attractive potential well from the asymptotic region. This barrier may give rise to quasi-bound states of the effective potential [150, 10] which are also termed shape resonances or orbiting resonances since they can be considered a quantum analogy of the classical orbiting phenomenon. Although they are found at energies above the dissociation limit, shape resonance bear many resemblances with bound states. Typically, the probability amplitude $|\psi(r)|^2$ corresponding to these quasi–bound states exhibits a high probability amplitude in the region of the well of the effective potential. Hence, the amplitude roughly coincides with the range of permanent or transition dipole moments. As a consequence, these states should be very suitable for manipulation by external fields and we expect their contribution to largely exceed that of free states. Indeed, shape resonances [86, 87] have been observed in photoassociative collisions of ultracold Rb atoms [2].

Due to the similarity with bound states, shape resonance states can be considered as a continuation of the vibrational progression of the bound states towards higher energies in the continuum. Accordingly, the number of nodes increases by one from the highest bound state to the lowest quasi-bound states etc. This behaviour provides an easy means of computationally detecting shape resonances. When scanning the scattering phase $\delta_J(E_0)$ versus scattering energy E_0, one finds a sudden increase of the phase by an amount of π whenever the number of nodes of the wavefunction increases by one [131]. In practice we locate shape resonances in two different ways. First, we integrate the radial

[2] The same authors recently also reported the detection of Feshbach resonances [151, 152]

Schrödinger's equation numerically using a Bulirsch–Stoer method [130]. Second, we use a semiclassical Airy function method [153]. The results are found to be in very good agreement with each other. The energetic widths can be obtained from

$$\Gamma = \left(\frac{d\delta J}{dE_0} \right)^{-1} \tag{2.44}$$

where the derivative is to be taken at the centre of the resonance.

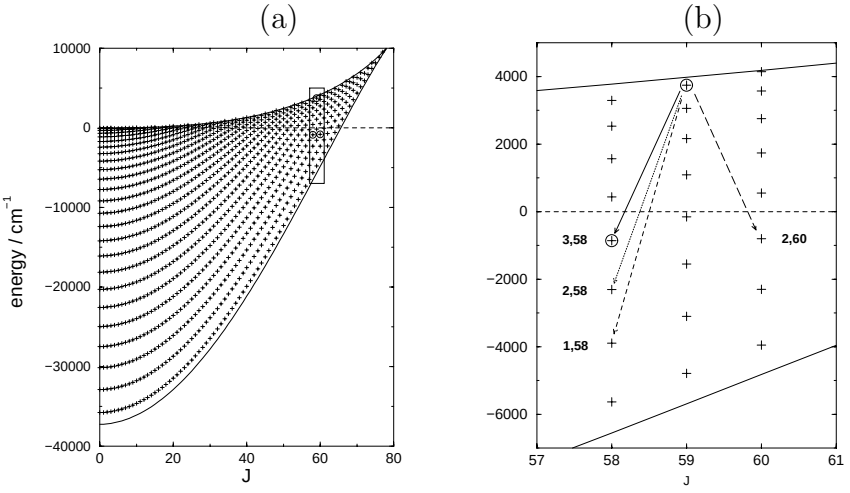

Figure 2.8: (a) Bound and quasi-bound states (shape resonances) of the HCl molecule. The lower and upper envelopes correspond to the minimum of the well and to the maximum of the centrifugal barrier, respectively. (b) Enlarged section (see rectangle in part (a)) together with the arrows indicating possible photoassociation processes (see text). From A.4

Bound and quasi-bound states of the HCl molecule are illustrated in Fig. 2.8 (a). For increasing angular momentum J, the bound states are gradually shifted upwards until they finally become unstable ($E > 0$). Here the number of bound states decreases from 24 for the rotation-less Morse oscillator ($J = 0$) down to a single bound state for $J = 66$ yielding a total of 984 bound states. At the same time, 176 quasi-bound states appear with their energy between the minimum and the local maximum of the effective potential for $9 \leq J \leq 77$.

In contrast to bound states, shape resonance states exhibit some probability amplitude outside the barrier, too. This is a consequence of the metastable nature of the quasi–bound states. Their lifetime corresponding to tunnelling through the centrifugal barrier in the effective potential is determined by the height and the width of the centrifugal barrier as well as by the reduced mass of the system. For the HCl molecule the resonance widths are typically $\Gamma \leq 1$ cm^{-1} which corresponds to lifetimes $\hbar/\Gamma$ of the order of one picosecond or more. However, in a few cases where there is a quasi-bound state just below the centrifugal barrier there are shorter lived resonances. Here the extreme is the $(v = 10, J = 53)$ state with a lifetime of 150 fs.

State Selectivity

As a first step on our way to achieve high efficiency and high state selectivity in a photoassociation reaction, we have to choose an appropriate initial state. In order to achieve realization in an experiment with limited energy resolution, it is advisable to select the quasi-bound state which is energetically most separated from the others. In our example this is the $(v = 7, J = 59)$ state which is separated by 120 cm^{-1} from its neighbours and which serves as a reference case in the following.

Second, we have to choose a final state. Since it is well–known that the efficiency of a bound←bound transition rapidly decreases with increasing difference Δv in the number of nodes we define the highest bound states for each allowed value of the angular momentum J as our target levels. With the selection rule $\Delta J = \pm 1$ for dipole transitions, there is a choice of two different transitions, i. e. P and R branch. We choose the P branch transition because for lower values of J the highest bound state may have more radial nodes. Indeed, this is the case for our example where we prefer the (3,58) over the (2,60) state because of the better overlap with the initial (7,59) state, see Fig. 2.8 (b).

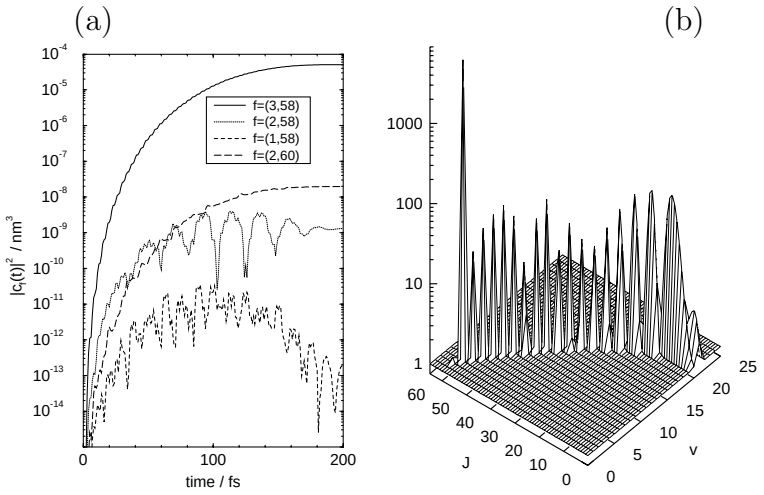

Figure 2.9: (a) Population dynamics during a HCl photoassociation reaction induced by a laser pulse optimised for the $(3, 58) \leftarrow (7, 59)$ transition (for the parameters, see A.4). The initial state is assumed to consist of the $J = 7$ partial wave only. (b) Final state population after the same photoassociative collision using the same laser pulse but for a plane wave (superposition of all partial waves) as initial state. The truncated peak value for (3,58) is 5670 pm^2. From A.4

Once initial and final states are chosen, we have to optimise the shape of the laser pulse in order to achieve maximum population transfer for the $(3, 58) \leftarrow (7, 59)$ transition considered here. For simplicity we assume here that

the initial state consists of the $J = 7$ partial wave only. Similar to the work presented in the last two subsections, the duration of the laser pulse is fixed. Dictated by the requirement that the pulse has to be considerably shorter than the lifetime of the quasi-bound state (here 5 ps), we choose a value of $\tau = 200fs$. For a not too high amplitude of 514 MV/m the optimal frequency is found to be 4605.9 cm^{-1} representing a detuning of $\Omega = -6.6$ cm^{-1} with respect to the Bohr frequency for the bound←quasibound transition.

The resulting population dynamics is shown in Fig. 2.9 (a). We find a remarkably high state selectivity with respect to both rotational and vibrational states of the molecular product. The cross section for the P branch transition (3,58) is more than three orders of magnitude larger than the R branch transition (2,60). Moreover, the transition to the highest vibrational level (3,58) is four orders of magnitude more effective than transitions to the second highest (2,58). Note that the latter result is compatible with results of our first study of photoassociation using a rotation-less model of the OH collision pair (see A.1). It is noted that these results also confirm the validity of the perturbative *ansatz* presented in Sec. 2.2.6. The probability of the first–order processes is considerably larger than that for any of the second–order processes.

Finally we want to lift the restriction of the initial state consisting of a single partial wave. Instead we consider a plane wave with contributions of all angular momentum states but with the collision energy exactly coinciding with the (7,59) shape resonance, see Fig. 2.9 (b). As anticipated above the contribution of the resonant $J = 7$ partial wave is by far the largest because of the overlap of the probability density with the dipole moment function (see Fig. 6 of A.4). The contributions of the other partial waves are at least 50 times smaller. The final states can be found along an isoenergetic curve in the (v,J) plane. In total, the final population caused by all the non–resonant partial waves is a factor of four smaller than the contribution of the resonant partial wave.

Cross Sections

In a realistic experimental situation it is typically more difficult to control the scattering energy of the collision pair than the frequency or intensity of the laser pulses. In order to investigate the sensitivity of the photoassociation and photoacceleration on the former, we want to consider in this section the dependence of the collision cross sections for the two photo–induced inelastic scattering processes versus scattering energy. For the definition of cross sections for laser pulse induced process, see Chap. 2.2.5 and A.4. The parameters of the laser pulse are kept fixed to the values optimised for the $(3, 58) \leftarrow (7, 59)$ transition.

Our results are displayed in Fig. 2.10. The photoassociation spectrum (left) exhibits a few very sharp peaks corresponding to bound←quasibound peaks. Because of the pulse optimisation the $(3, 58) \leftarrow (7, 59)$ transition is the strongest one. Although the scattering energy covers almost all of the shape resonance states shown in Fig. 2.8 there are only a few other pronounced bound←quasibound transitions in the spectrum. This is because stabilisation

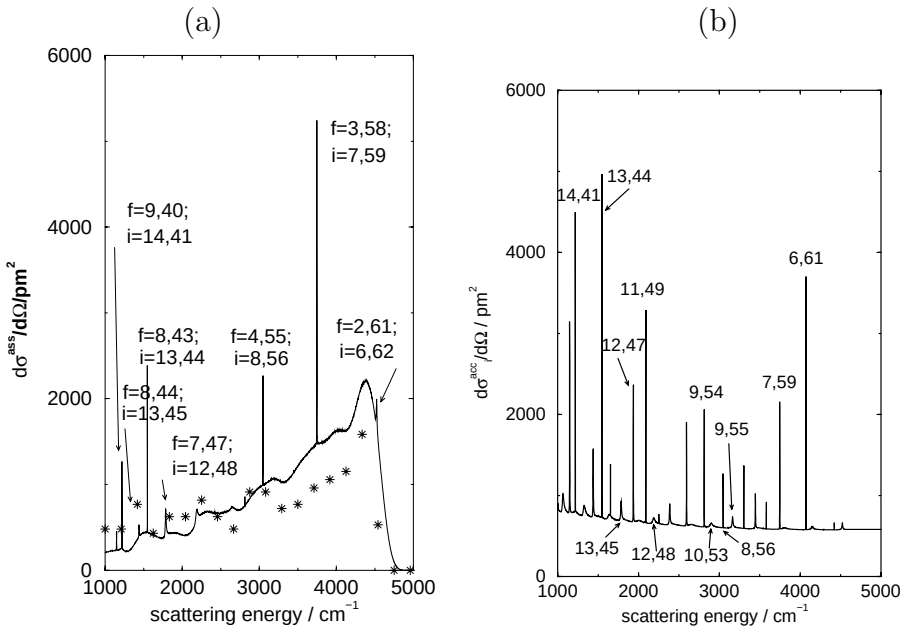

Figure 2.10: Cross sections (in pm^2) for photoinduced association (a) and acceleration (b) of HCl collision pairs versus scattering energy. The main peaks in the association spectrum are labelled by initial (i) and final (f) state, the stars indicate the density of bound states where the energy is shifted by the photon energy. The labels in the acceleration spectrum are labelled by the initial states only.

of a shape resonance state is only effective if the photon energy matches the Bohr frequency for a transition down to a bound state level within the width of the effective line shape.

Apart from the sharp peaks there is also a broad background in the photoassociation spectrum of Fig. 2.10 (a). It is caused by bound←free transitions with non–resonant initial states. Because of the large number of non–resonant partial waves, details of the Franck–Condon factors such as the undulations in Fig. 2.9 (b) are averaged out and the contribution of free initial states to the photoassociation signal is a smooth function of the scattering energy. It qualitatively follows the density of bound states accessible in one–photon transitions which is continuously rising up to a sudden fall–off at the dissociation limit.

A photoacceleration spectrum is shown in Fig. 2.10 (b) for the same laser pulse as for the photoassociation spectrum. It can be seen that the shape resonances cause sharp peaks corresponding to free←quasibound in the spectrum. As far as the energy is concerned, all shape resonances are eligible for photoacceleration. Nevertheless, only a relatively small fraction of the quasi-bound states give rise to a peak. In this case the crucial selection criterion is the lifetime of the quasi-bound state. In particular, for a given spectroscopic resolution ΔE long lived states with a lifetime $\gg \hbar/\Delta E$ cannot be detected. For example, in the HCl spectrum in Fig. 2.10 (b) which has been calculated with

$\Delta E = 1$ cm^{-1} there are only the fingerprints of 25 shape resonances.

2.3.7 Summary and Outlook

In the present section 2.3 photoassociative collisions of two colliding atoms are treated. By stimulated emission of light, a collision pair can be stabilized to form a ground state molecule. Alternatively, a collision pair can be stabilized by absorption of light to form a molecule in an electronically excited state. The special emphasis in the studies presented here is – apart from the efficiency – on the selectivity with respect to the quantum state of the molecular product.

The work in A.1 and in A.2 represents the first studies of ground state photoassociation by infrared picosecond light pulses. By simultaneous optimization of the incoming wavepacket and of the laser pulse, photoassociation can be achieved with a high efficiency of $> 80\%$ for a rotation–less model of an O + H collision pair. At the same time, an extremely high vibrational state selectivity close to 100% is achieved. The problem of near–coincidence with higher–order transitions can be circumvented by careful tuning of the scattering energy versus the laser frequency.

The high efficiency and state–selectivity also persists if rotational degrees of freedom are taken into account, see our work in A.4, where the effect of shape resonances on photoassociation reactions is treated for the first time. The high scattering cross section of shape resonance states can lead to considerably enhanced efficiency of photoassociation reactions. At the same time, preparation of molecules in specific ro–vibrational states is possible because the condition for a shape resonance is only met for one specific partial wave. It is also predicted in A.4 that these effects can be observed in high–quality molecular beam experiments.

To drive our investigations of photoassociation dynamics one step further, we have also addressed the question of electronic state–selectivity upon photoassociation. This is especially interesting for molecules where low–lying bound electronic states exist and where ground and excited state processes are eligible in a similar frequency regime. It is demonstrated in A.3 for the example of the OH radical that even in these cases various control mechanisms exist. Apart from the different polarization of permanent and transition dipole moments, effective control can be exerted through variation of the scattering energy of a collision pair.

So far, we have considered photoassociation with molecular products in relatively high ro–vibrational states. The possibilitiy to populate also lower states in a direct one–photon process are limited because of the competition with multi–photon processes which become abundant for higher fields. An elegant alternative is the use of sequences of several laser pulses to descend the ladder of ro–vibrational levels in analogy to our work on vibrational excitation [117]. This strategy is expected to finally render the production of ultracold–molecules possible [91]. Also the problem of unfavourable Franck–Condon factors for excited state photoassociation can be circumvented in this way (A.3).

In principle, the process of ground state photoassociation by stimulated emission competes with photoacceleration induced by absorption of photons.

In these inelastic free←free transitions, the collision pair is accelerated in the field of the laser pulse. In analogy to the phenomena of above–threshold ionization and above–threshold dissociation the increase of kinetic energy corresponds to the energy of one or more photons and leads to sharp peaks in the energy distribution of the scattered particles. In A.2 and A.4 this process is explored for the first time. Despite of some limitations the process of photoacceleration provides an efficient means of radiation–induced acceleration of neutral atoms. Acceleration of molecules can also be achieved by rotational or vibrational excitation and subsequent RT or VT energy transfer [154]. For atoms without internal degrees of freedom this channel is not at our disposition and the process of photoacceleration presents the only alternative for IR light if electronic transitions are not eligible. Hence it represents a method to produce fast atoms with narrow and well–defined energy–distributions.

2.4 Wavepacket Dynamics

2.4.1 Model System

As a model system for our work on the wavepacket dynamics of photoassociative collisions we choose the exciplex formation of molecular mercury Hg_2. This choice was motivated by the first femtosecond photoassociation spectroscopy (FPAS) experiment by Marvet and Dantus [82, 83]. Utilising this novel experimental technique the quantum dynamics of the formation of a chemical bond in a photoassociative collision could be detected in real time by means of a pump–probe technique.

A first (pump) laser pulse excites a collision pair of two ground state mercury atoms (6^1S_0) which are interacting through a potential with an extremely shallow van der Waals well from a continuum level to a ro–vibrational bound state of the first electronically exited state ($D^3\Sigma_u^+$). The subsequent dynamics of the newly formed molecule in the exciplex state can be monitored by excitation of the Hg_2 with a second (probe) pulse to an electronic state which results from the avoided crossing of a $^1\Pi_g$ and a $^3\Sigma_g^+$ state [155] causing a depletion of the fluorescence signal from the $D^3\Sigma_u^+$ state.

The potential energy curves of the electronic ground state and of the two excited states are illustrated in Fig. 2.11. For reasons of simplicity, these states will be termed here as $|0\rangle$, $|1\rangle$, and $|2\rangle$. Our data are taken from *ab initio* calculations [156, 157, 158, 159] and from analysis of experimental continuous wave photoassociation spectra in Refs. [155, 79, 80]. The transition dipole moment for the $|0\rangle \rightarrow |1\rangle$ transition is adapted from the first principles calculations [156] while for the $|1\rangle \rightarrow |2\rangle$ transition we have to resort to the Condon–approximation of assuming a constant value (2.54 D) because reliable data are not available.

2.4.2 Excitation probability

As has been demonstrated in Sec. 2.2.6 the dynamics of a molecular system subsequent to excitation with an ultrashort laser pulse is completely determined

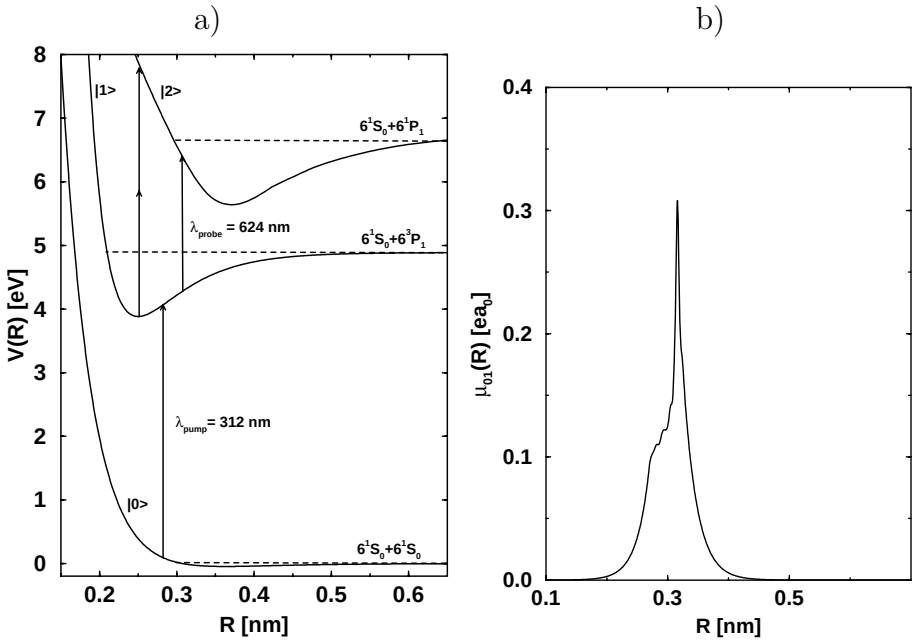

Figure 2.11: a) Potential energy curves used for the wavepacket simulations of the femtosecond photoassociation of Hg_2. A pump pulse (312 nm) excites a continuum wavefunction of the electronic ground state $|0\rangle$ to bound ro–vibrational level of the first electronically excited state $|1\rangle$. A probe pulse (624 nm) is used to further excite the system to the state $|2\rangle$. b) Transition dipole moment for the pump transition $|0\rangle \rightarrow |1\rangle$. From A.5.

by probabilities $|c_{inJM}(2T_p)|^2$ of exciting certain molecular eigenstates at the end of the laser pulse. Apart from the Franck–Condon factors and the Hönl–London factors in Eq. (2.34), the excitation probability is essentially determined by the energtic band width of the laser pulseas specified in Eq. (2.35).

This dependence is illustrated in Fig. 2.12 for the photoassociative transition $|0\rangle \rightarrow |1\rangle$ of the mercury molecule. For the while being let us neglect rotational effects and let us consider only $|0E_000\rangle \rightarrow |1v10\rangle$ transitions (using the $|inJM\rangle$ notation of section 2.2.5) where E_0 specifies the (initial) scattering energy and v specifies the (final) vibrational state.

1. For the pulse length of $T_p = 65fs$ adapted from the experimental work of Marvet and Dantus [82, 83], the width of the main peak of the effective line shape function (2.35) encompasses several vibrational spacings of the system (see below). Equivalently, the classical vibrational period of the $Hg_2(D^3\Sigma_u^+)$ equals several times the pulse length of the $Hg_2(D^3\Sigma_u^+)$ state.

2. The Franck–Condon factors exhibit an oscillatory behaviour which is typical for bound←free transition which is more commonly known as the reflection principle for the reversed process, i. e. photodissociation [160,47].

3. The excitation probability is non–zero only within the frequency regime

a) $E_0 = 93$ meV b) $E_0 = 125$ meV

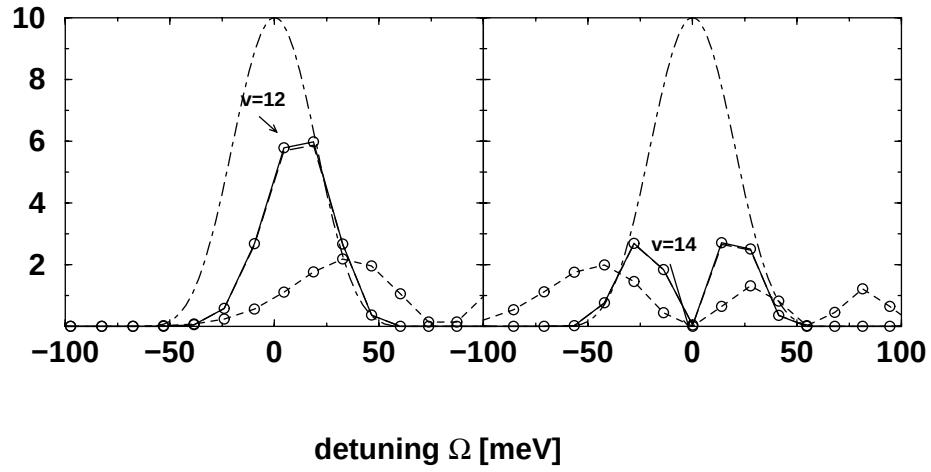

Figure 2.12: Excitation probabilities (arb. units) for photoassociative bound←free transitions of the mercury collision pair by a pump laser pulse (312 nm, 65 fs, 8.85 MV/cm). The solid curves show the result for $|0E_000\rangle \rightarrow |1v10\rangle$ excitation versus the detuning $\Omega_{0E_000,1v10}$ for two different initial energies E_0. Dotted curve: Fourier transform of the laser pulse. Dashed curve: Franck–Condon factors. From A.5.

of the line shape function and exhibits the undulatory behaviour of the Franck–Condon factors. By variation of the scattering energy, these two functions can be shifted with respect to each other. In principle, two different cases can arise: (a) If the maximum of the former one is close to a maximum of the latter one, the excitation probability has one peak. (b) If, however, the maximum of the former one is close to a minimum of the latter one, the excitation probability exhibits a bimodal feature.

2.4.3 Vibrational Coherence

As has been pointed out above, the ultrashort pulses excite a coherent superposition of a few vibrational levels of the electronically excited state. For the two representative scattering energies of 93 meV and 125 meV (see Fig. 2.12) we find excitation of four adjacent levels or of two times three adjacent levels, respectively. This means that these laser pulses are relatively close to the vibrationally abrupt limit. In agreement with the work of Machholm et al. [90] the coherent excitation of three to four adjacent states is just wide enough to create localised wavepackets in the excited state close to the Condon point ($V_1(r) - V_0(r) = \hbar\omega$) of the respective transition. Hence, we obtain one or two localised wavepackets for the two collision energies considered.

Subsequent to the excitation, these superposition states evolve in time. Initially, the wavepackets remain localised and their centres follow a classical tra-

jectory. Only at the turning points of the oscillatory motions weak interferences between ingoing and outgoing portions of the wavepackets occur. A first order estimate of the vibrational period is given by the correspondence principle

$$T_{\mathrm{vib}}(v) = \frac{h}{E_{v+1} - E_v} \tag{2.45}$$

which is in the order of 300 fs. Illustrations of the wavepacket dynamics can be found in Fig. 3 of Appendix A.5.

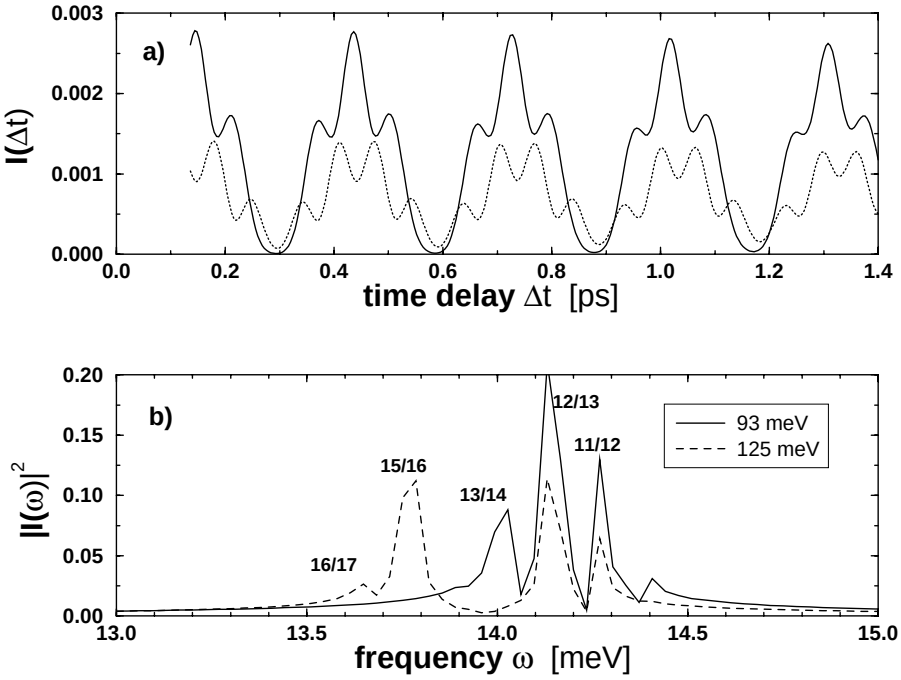

Figure 2.13: Simulated pump–probe spectra of the mercury photoassociation dynamics for different collision energies. Pump pulse: see caption of Fig. 2.12. Probe pulse: 624 nm, 65fs, 88.5 MV/cm. a) Population of second excited state versus pump–probe delay time. b) Power spectrum. From A.5

The vibrational dynamics of the photoassociated Hg_2 molecule in the first electronically excited state can be probed by excitation to a second state which does not contribute to the fluorescence thus depleting the spectroscopic signal. Fig. 2.13 (a) shows the population of the highest state as a function of the delay time between pump and probe pulse. First of all, we see periodic undulations with a period of 292 and 296 fs corresponding to semiclassical vibrational period for $v = 12$ and $v = 14$, respectively. There is also a fine structure leading to a splitting of the peaks into three or four peaks. This structure of the transient can be easily explained by considering the Condon points for one photon ($V_2(r) - V_1(r) = \hbar\omega$) and two photon ($V_2(r) - V_1(r) = 2\hbar\omega$) processes for a probe wavelength of 624 nm. Because the former one is far outside the classically allowed region, we have only to take the second one into account.

Then the fine structure of the pump–probe transients can be easily understood by considering the passing of the wavepacket through the Condon region.

A deeper insight into the wavepacket dynamics is provided through a power spectrum of the transient. In the energy/frequency domain there is a clear signature of the excitation process by the pump pulse. The example of Fig. 2.13 (b) exhibits a series of peaks corresponding to the energy differences between those vibrational states that were initially excited. These are the well–known quantum beats typically arising for expectation values of superposition states (see e. g. Eq. (2.25) in Sec. 2.2.5.

At longer times, however, the anharmonicity of the potential starts to play a role. Because the vibrational period (2.45) depends on the vibrational state v, the different vibrational states comprising the wavepacket oscillate with slightly different periods which leads to a smearing of the wavepacket in space until it becomes completely delocalised. However, this behaviour is not irreversible and after some time we expect the different states to be in phase again and the wavepacket to regain its original (localised) shape. A reasonable approximation for the time of such a "revival" of a wavepacket is given by [161]

$$T_{\mathrm{rev}} = \frac{2T_{\mathrm{vib}}}{|\partial E_v/\partial E|} \tag{2.46}$$

Inserting the first order difference

$$\partial E_{v,J}/\partial E \approx \frac{E_{v+1} - E_v}{E_{v,J}} \tag{2.47}$$

yields a revival time of 67.24 ps for the mercury system.

Also at shorter times there can be a re-phasing of some part of the vibrational states, see our results for Hg_2 in Fig. 4 of A.5. At integer fraction of T_{rev} this leads to characteristic splittings of the wavepackets and, correspondingly, to frequency doubling, tripling, etc., of pump–probe signals. This phenomenon of "fractional revivals" [161, 162, 163, 164] was detected for the first time for Rydberg atoms. Meanwhile their universality in time–dependent spectroscopy is well established, see e. g. the work on diatomic molecules [165, 120] and on triatomic molecules [166].

2.4.4 Rotational Coherence

Up to now, we have only considered purely vibrational coherence phenomena, i. e. we have assumed that the initial state is a single partial wave with well–defined angular momentum J. According to the quantum–classical correspondence principle, this is equivalent to a collision with a given impact parameter. However, in order to simulate a realistic experimental situation, we have to take contributions from all partial waves comprising a plane wave into account.

In principle, rotational coherence effects can be treated in the same way as vibrational coherence effects. The pump laser pulse excites a manifold of different rotational states of the mercury molecule in the first electronically excited state all of which have a different time evolution according to Eq. (2.25). Assuming the rotational selection rule $\Delta J = \pm 1$ to be valid, the pump–probe

signal from each partial wave should exhibit quantum beats due to the interference of P and R branch. In analogy to the equation for the vibrational timescale (2.45) this leads to

$$T_{\mathrm{rot}}(J) = \frac{h}{E_{J+1} - E_{J-1}} = \frac{h}{B(4J+2)} \tag{2.48}$$

For a rotational constant of $B = 3.3\mu$eV for ^{202}Hg, this leads to timescales between a few hundred picoseconds ($J = 1$) and a few picoseconds ($J = 100$). We see that there is a strong quantitative difference to the vibrational result because here we have a superposition of a very large number of states with greatly varying frequencies. As a consequence, on the timescale considered here the effect of vibrational coherence leads to a monotonically decreasing signal similar to a Gaussian curve [167, 168, 169]. The decay time is found to be in good agreement with the experimental result (see below).

2.4.5 Thermal averaging

Up to this point we have only considered bound←free transitions originating from an initial scattering state with well–defined collision energy E_0. In the following, we want to simulate the situation in a thermal experiment in order to compare our results with the experimental ones of Refs. [82, 83] which were obtained for a temperature of $T = 433$ K.

- First of all, it is not *a priori* clear that the experimental signal is only caused by bound←free transition. However, it turns out that bound←bound transitions from van der Waals precursor complexes can be excluded for two reasons. First, the ratio of dimers versus monomers is only 3.5×10^{-5} [82, 170]. Moreover, the spectral signal arising from bound←bound transitions is much smaller than that from bound←free transitions because of the limited range of the transition dipole moment function which is already very small for the typical bond length of a vdW Hg_2 molecule in the electronic ground state, see Fig. 2.11 (b). Hence, the dimer contribution can be safely neglected we and conclude that the experiments are of truly bimolecular nature [171].

- Second, a Maxwell–Boltzmann averaging over the free initial states has to be performed. Before considering the averaged spectra it is very instructive to investigate the excitation probabilities for a photoassociative transition $|0\rangle \rightarrow |1\rangle$ versus angular momentum J and collision energy E_0. As can be seen from Fig. 2.14 (a), this probability is only large in a very limited range of the two independent variables. Basically these limitations can be explained by the shape of the effective potential energy curves 2.14 and by the reflection principle [172,47] governing the Franck–Condon factors for bound←free transitions, see Ref. [84] and App. A.5. We can conclude that, together with the Boltzmann weighting factor, photoassociative excitations are only possible for a relatively narrow region of the E_0, J plane.

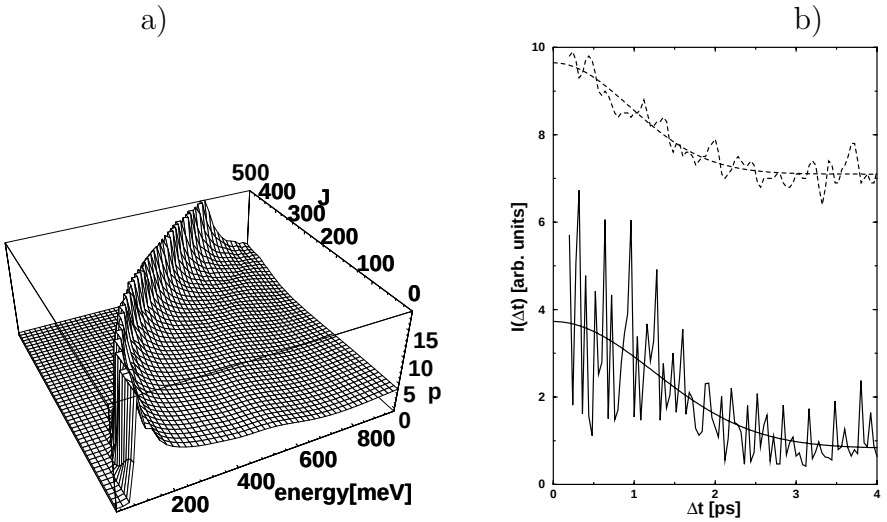

Figure 2.14: Averaged pump–probe photoassociation spectra of mercury. (a) Probability of a photoassociative transition versus collision energy and angular momentum. (b) Averaged pump–probe transients for $T = 433$ K. Solid curve: Simulated spectrum. Dashed curve: Experiments [82]. The smooth curves are fitted Gaussians. From A.5.

Our result for an averaged pump–probe spectrum is presented in Fig. 2.14 (b). Despite of the averaging over the collision energy E_0 and the summation over all partial waves J, there is still a pronounced vibrational structure in the simulated transient. However, the structure is more irregular than that of the transients in Fig. 2.13. Note that the vibrational structure of the simulated transient cannot be quantitatively compared with the experimental transient because of the insufficient time resolution of the latter, but the qualitative picture, i. e. the Gaussian–like decay due to the rotational dephasing is nicely reproduced. Note that we could not compare the Fourier transforms of the transients either because the length of the experimental transients (6 ps) limits the resolution to 0.7 meV.

2.4.6 Summary and Outlook

In the present work (A.3) a fully three–dimensional model for the theoretical description of pump–probe experiments on photoassociation reactions is developed. Based on the approach of Machholm et al. [90] our *ansatz* additionally includes the role of rotations which proves crucial for the explanation of the rotational coherence phenomena. It is shown that for the experimental conditions considered here a perturbational approach and use of the rotating–wave approximation are fully justified and lead to considerable simplifications of the equations to be solved.

In agreement with our earlier results [171], we find that the photoassociation events observed in the experiments by Marvet and Dantus on the process of

exciplex formation of Hg_2 [82, 83] are indeed due to bound←free transitions, i. e. originate from free collision pairs (Hg+Hg), while the role of bound←bound transitions from preformed complexes (Hg_2) can be neglected. Thus we have shown that the femtosecond photoassociation spectroscopy is a truly bimolecular process not involving van–der–Waals precursors. Another remarkable finding is that even for a model including hundreds of partial waves and accounting for the thermal averaging in a cell experiment at relatively high temperature, a pronounced vibrational structure persists. A comparison of measured and simulated pump–probe signals shows satisfactory quantitative agreement with the experiment.

Another interesting aspect is the sensitivity of femtosecond photoassociation spectroscopy on the potential functions and dipole moment functions. It has been demonstrated that both the probability for photoassociation and the subsequent vibrational dynamics sensitively depend on the Franck–Condon factors for bound←free transitions and hence on the shape of the transition dipole moment. Moreover, Fourier transforms of the transients reveal the underlying quantum beats of the ro–vibrational states comprising the wave packet created in the pump process. These beats are a direct measure for the level structure of Hg_2 in the $D^3\Sigma_u^+$ state. In summary, photoassociation can serve to refine both potential energy functions and transition dipole moment functions for excimer systems.

So far, the only severe limitation of our model is the restriction to only three electronic states. In order to reach a quantitative agreement between measured and simulated transients, we would have to account for fluorescence depletion by other electronic states which are accessible by probing from the $|1\rangle$ state. Moreover, also non–adiabatic coupling between these states has to be taken into account. As has been demonstrated in Ref. [84], this could explain the lower modulation depth of the experimental pump–probe spectra.

As has been shown in Fig. 2.14 (a), the excitation probability depends crucially on energy and impact parameter of the collision pairs. Equivalently, there is a strong correlation of the wavelength of the pump pulse and the impact parameter. This allows a limited control the impact parameter in photoassociative collisions by variation of the wavelength [84, 85]. Another interesting control mechanism arises when studying the total photoassociation yield versus pulse length of the pump pulse. Decreasing the pulse length leads to wider line shape functions and the association yield increases until all ro–vibrational states are accessible at around 10 fs. For even shorter pulses, the yield decreases again [173].

Chapter 3

Solvent–Induced Stabilization of Collision Pairs

3.1 Motivation

In this section we want to treat the stabilisation of collision complexes by interaction with a solvent. In order to form a stable molecule from an intermediate collision complex in the absence of radiative processes, the excess energy has to be removed by the solvent particles. In principle there are two different dynamical mechanisms, through which an association reaction can be affected by the presence of a solvent.

1. The interaction with the solvent can serve as a dissipative mechanism that removes energy from the collision complex in order to bring it below its dissociation limit and further down to lower states in a series of cascading steps. Clearly, the efficiency of such electronic, vibrational and/or rotational relaxation processes depends on the energy transfer from the solute to the solvent which acts as a local heat bath. Hence both kinematic aspects and the interaction potential determine the reaction dynamics.

   While this process is ubiquitous in liquids [46] it represents a relatively rare event in gases since it requires (at least) a ternary collision [2,44,45]. If a third particle removes enough energy from the collision complex to prevent re-dissociation on a timescale faster than the decay time of the complex, it can lead to permanent association. This is the well known "third body" or "chaperon" effect which shall be investigated here for the extreme case of only a single solvent atom in a van der Waals dimer.

2. The other prominent solvent effect which shall be studied in the present work is the cage effect where solvent particles may shield the reactants from each other thus preventing the formation of a collision complex. Note that the cage effect in the context of a truly bimolecular collision event has rarely been studied (see below). However, the underlying mechanism of caging is in close analogy to the cage effect observed for photodissociation in condensed matter which is well characterised both in experiment and in theory.

Obviously it is very advantageous to study these solvent effects on association reactions in the framework of clusters [174,55]. The simple framework of a van der Waals (vdW) cluster makes the theoretical treatment very promising. In particular, it allows us to vary the size of the "micro-solvation" step by step from the one extreme of a "single atom solvent" via one (or more) complete solvation shells to the other extreme of molecules embedded in a rare gas liquid or matrix. Apart from being able to control the solvent size we also benefit from the restricted geometries provided by the vdW cluster.

There are only relatively few studies of bimolecular "cluster–catalyzed" reactions in the literature. In the following we list a few examples of reactions where one of the reagents is solvated in a vdW cluster. Reactions of O atoms with clusters of NO [175], CO [176], and with hydrocarbon–argon clusters [177] have been investigated in crossed beam experiments. On the theoretical side, there are classical trajectory simulations of CH_3 + HAr_n [178] as well as of I + IAr_n ($n = 12, 54$) where the chaperon effect, caging and trapping of reagents

have been explored [179,180,181,182]. Another stimulating example is provided in the trajectory study of association reaction between non–stoichiometric NaCl cluster cations complexed with Ar and Cl anions [183].

A closely related field are associative cluster–cluster collisions where two clusters unite to form a compound cluster. Due to the large number of internal degrees of freedom, redistribution of the energy can temporarily stabilise the reaction products. Even in the absence of a solvent compound clusters may survive a relatively long time before they finally stabilise themselves by loosing particles. This mechanism of evaporative cooling [184, 185] of cluster–cluster collision complexes can also be regarded as solvent induced stabilisation in which the internal degrees of freedom of the product are acting as its own solvent. Examples are fusion reactions of sodium clusters [186] or studies of fullerene fusion [187,188,189,190,191,192].

Another mainly unexplored aspect is that apart from using the vdW environment to modify the reaction dynamics, studies of reactions in clusters can also be used as a tool to probe structure and dynamics of the vdW host cluster. Thus they can represent a complimentary approach to the spectroscopy of guest molecules embedded in vdW clusters. In particular, the issue of isomerisations and melting-like transitions of finite size clusters has been much debated in the last few years [193, 194, 195, 196, 197, 198, 199, 200, 201]. Here we intend to investigate the question of structural transitions of a van der Waals cluster on the reactivity in collisions with atoms.

In the present work we study the solvent induced stabilisation of collision pairs for two different classes of model systems:

1. In our work on **atom–cluster–collision** (B.2, B.1) we investigate diatomic association reactions where one of the reagents is bound to a heterogeneous van der Waals clusters. For the model system

$$H + Cl \ldots Ar_n \rightarrow HCl \ldots Ar_{n-m}, \quad m \leq n \tag{3.1}$$

   we simulate solvation processes on association reactions in the environment of a vdW cluster. In our studies we consider two cases. First, the "chaperon" effect shall be investigated for the extreme of the "single atom solvent" ($n = 1$) . Second, the cage effect shall be studied for the case of the first complete solvation shell ($n = 12$). In particular, we are interested in the effect of structural ("melting-like") transitions of the shell on the cage effect and the reactivity.

2. In our work on **cluster–cluster–collision** (B.3) we choose homogeneous potassium chloride clusters as a model for the cluster growth from the gas phase. Here our special interest is in the stabilisation of the compound clusters by redistribution of energy in the many internal degrees of freedom, and finally the evaporation of particles.

3.2 Computational Details

3.2.1 Introductory Remarks

In general, the dynamics of a molecular scattering process has to be described by the time–independent or time–dependent Schrödinger's equation, see the previous section on photoassociation. For larger bimolecular systems, however, this is not possible with today's computational means. At the present time, the largest systems for which a full quantum description of reactive collision events is feasible are limited to three or four atoms, see recent publications in Ref. [39].

Hence, in the present work we restrict ourselves to a classical description of the atom–cluster and cluster–cluster collisions under investigation. This is, at least partly, justified for not too low collision energies and/or for not too low temperatures. Furthermore, many quantum effects such as the occurrence of resonances tend to get smeared out in systems with many degrees of freedom. Moreover, we are interested in global observables such as total reactive cross sections (*vide infra*) which are highly averaged quantities. Nevertheless quantum effects do play a role in the field of reaction dynamics, see e. g. the review by G. C. Schatz [202]. We have to be aware that due to the presence of the light hydrogen reagent, the HCl association reaction might be affected by quantum effects which we are neglecting here. However, we refer to Part II of this thesis where quantum effects on photodissociation are treated in detail.

3.2.2 Cross Sections

The standard techniques for calculating cross sections and rate constants for bimolecular reactions shall be only briefly reviewed here, for a detailed description see Ref. [203]. The most important ingredient of a classical investigation of reaction dynamics is the averaging over a large number of trajectories. The probability P_Λ for a given reactive event Λ is simply given by the number N_Λ of trajectories leading to the desired products divided by the total number N

$$P_\Lambda = \frac{N_\Lambda}{N} \tag{3.2}$$

This probability is a function of all the variables describing the initial conditions of the collision event, i. e.

- the relative energy $E_{\mathrm{rel}} = \mu v_{\mathrm{rel}}^2$ of the collision, where μ is the reduced mass of the collision pair
- the impact parameter b of the collision,
- the orientation of the collision partners, and
- the vibrational $\mathbf{v}_1, \mathbf{v}_2$ and rotational degrees $\mathbf{J}_1, \mathbf{J}_2$ of freedom of each of the molecular collision partners

The parameters describing the initial conditions are also illustrated in Fig. 3.1. Hence the reaction probability can be written as

$$P_\Lambda = P_\Lambda(E_{\rm rel}, b; \Phi_1, \Theta_1, \Psi_1; \Phi_2, \Theta_2, \Psi_2; \mathbf{v}_1, \mathbf{J}_1; \mathbf{v}_2, \mathbf{J}_2) \tag{3.3}$$

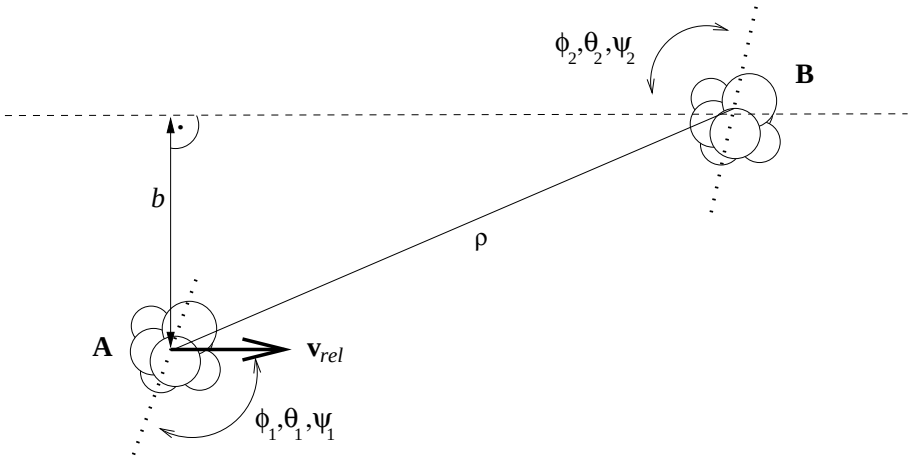

Figure 3.1: Initial conditions of a molecular collision

Based on this definition of the reaction probability, it is straight–forward to obtain cross sections of a reactive event for a given scattering energy $E_{\rm rel}$ by statistically averaging the reaction probability

$$\begin{aligned}
\sigma_\Lambda(E_{\rm rel}) &= \int_0^\infty 2\pi\, b\, db \\
&\times \int_0^{2\pi} \frac{1}{2\pi} d\phi_1 \int_0^{\pi} \frac{1}{2} \sin\theta_1 d\theta_1 \int_0^{2\pi} \frac{1}{2\pi} d\psi_1 \\
&\times \int_0^{2\pi} \frac{1}{2\pi} d\phi_2 \int_0^{\pi} \frac{1}{2} \sin\theta_2 d\theta_2 \int_0^{2\pi} \frac{1}{2\pi} d\psi_2 \\
&\times \int d\mathbf{v}_1 \int d\mathbf{J}_1 F_1(\mathbf{v}_1, \mathbf{J}_1) \int d\mathbf{v}_2 \int d\mathbf{J}_2 F_2(\mathbf{v}_2, \mathbf{J}_2) \\
&\times P_\Lambda(E_{\rm rel}, b; \Phi_1, \Theta_1, \Psi_1; \Phi_2, \Theta_2, \Psi_2; \mathbf{v}_1, \mathbf{J}_1; \mathbf{v}_2, \mathbf{J}_2) \quad . \qquad (3.4)
\end{aligned}$$

The first line of the equation stands for the integration over a ficticious plane perpendicular to the direction of approach of the collision partners. Note that the integral converges because any reaction probability approaches zero for increasing impact parameter ($P_\Lambda \to 0$ for $b \to \infty$). The following two lines indicate the averaging over the relative orientation of the collision partners. Normally, these orientations are given in terms of the three Euler angles of rotation Φ, Θ, Ψ commonly used in rigid body dynamics [204]. Finally, the fourth line of Eq. (3.4) is the integration over a distribution function in the vibrational ($\mathbf{v}$) and rotational ($\mathbf{J}$) degrees of freedom. Note that a few simplifying assumptions are made in the following sections: In all cases the rotational degrees of

freedom are frozen because their typical timescale is much slower than the typical timescale of a collision event. For the case of the H + $ClAr_n$ system, the integration over the internal degrees of freedom of the relatively floppy $ClAr_n$ cluster is carried out by sampling from a molecular dynamics (MD) simulation. In contrast, for the KCl_n + KCl_m system the relatively stiff internal degrees of freedom are considered rigid, which reduces Eq. (3.4) to a 7–dimensional integral.

The numerical evaluation of the multidimensional integral (3.4) presents a formidable challenge. For any but the smallest systems these integrals are typically carried out by means of Monte–Carlo (MC) techniques [205]. In this approach, a large number of individual sets of trajectories is propagated starting from initial conditions sampled randomly from the respective distribution functions. This method has the advantage of being independent of the number of degrees of freedom. Although the numerical error

$$\Delta_{\mathrm{MC}}\, \sigma_\Lambda \sim N^{-1/2} \tag{3.5}$$

converges relatively slowly, this method presents the only viable approach to truly high–dimensional integrals.

The calculation of (reactive) cross sections σ_Λ versus (relative) collision energy E_{rel} is tailored to the description of atomic or molecular beam experiments which indeed have contributed considerably to the understanding of chemical reaction dynamics [12]. Once having obtained cross sections $\sigma_\Lambda(E_{\mathrm{rel}})$, it is straight–forward to convert these data to (thermal) rate constants by simply averaging over a thermal energy distribution

$$k_\Lambda(T) = \int dE_{\mathrm{rel}} E_{\mathrm{rel}}^{3/2} \sigma_\Lambda(E_{\mathrm{rel}}) \exp\left[-\frac{E_{\mathrm{rel}}}{2k_b T}\right] \tag{3.6}$$

where T is the temperature and k_B is Boltzmann's constant.

3.2.3 Classical Trajectories

Initial Conditions

All simulations are carried using a frame of reference fixed at the centre–of–mass of the colliding particles. The initial separation of the collision partners has to be chosen large enough so that their interaction becomes negligible. For the H + $ClAr_n$ systems we choose $1 \ldots 1.5$ nm, for the alkali halide systems with their long range multipole interactions the distance is increased to 5 nm. The impact parameter b is the component of the separation perpendicular to the direction of the relative velocity. The integration is extended up to a maximum value b_{max} of $1 \ldots 2$ nm. The random orientation of the molecular collision partner(s) is achieved by randomly picking numbers $\Phi_{1,2}$, $\Psi_{1,2}$ from the interval $[0, 2\pi[$ and by selecting $\cos\Theta_{1,2}$ from $[-1, 1[$.

Integration of the Equations of Motion

For each of the randomly chosen initial conditions one set of trajectories for the participating atoms has to be propagated in time. To solve Newton's equations

of motion numerically, we choose a six–point predictor–corrector scheme developed by Gear [206]. It is noted that the accuracy required for simulations of molecular collisions is higher than for thermal molecular dynamics (MD) calculations where typically a Verlet or a "leap frog" algorithm is sufficient [207,208].

Another feature typical of the numerical simulation of collision processes is the drastic change of the forces. Both before and after the collision event, the collision partners experience relatively weak interactions, while the intermolecular forces are strong during the short phase of the close encounter of the reagents and the rearrangement of the atoms to form the products. Consequently, the use of a time-step adapted is highly advantageous. Here the time-step is scaled according to the maximum components of the forces. Typically, in the course of a reactive trajectory, the time increment is reduced from 10 fs down to 0.1 fs and back to 10 fs again.

Final Conditions

The propagation of trajectories is continued until either one of the following two conditions is fulfilled: (1) The propagation is truncated if the reagents did not rearrange and their final separation exceeds the initial separation. In this case, the respective trajectory is considered non–reactive. (2) If a product is formed (HCl or $(KCl)_{n+m}$ in the atom–cluster or in the cluster–cluster collisions, respectively), the trajectory is continued until either the rare gas solvent atoms have all evaporated from the HCl product (typically a few ps) or until the $(KCl)_{n+m}$ has survived for the duration of a few rotational periods.

In the case of the HCl formation we are also interested in the efficiency of the evaporative cooling. As a measure, we calculate also partial cross sections for association reactions for individual ro–vibrational states of the product HCl molecule. A box quantisation is used to assign approximate quantum numbers v and J using the equations

$$E_{vib}(v) = \hbar\omega_0(v+\frac{1}{2}) - \hbar\omega_0\chi(v+\frac{1}{2})^2 \quad (3.7)$$

$$E_{rot}(J) = BJ(J+1) - D[J(J+1)]^2 \quad (3.8)$$

where the effect of vibration–translation coupling has been neglected. The harmonic frequency $\omega_0 = 3002$ cm^{-1}, the anharmonicity constant $\omega_0\chi = 60$ cm^{-1} are calculated from the Morse parameters for the electronic ground state given on page 25. The rotational constant is $B = 10.7$ cm^{-1} and the centrifugal distortion is $D = 0.00054$ cm^{-1}.

3.2.4 Potential Energy Surfaces

The total potential energy function is constructed as a sum of pairwise interactions between the atoms which is a reasonable approach at least for the closed shell atoms and ions considered here.

Van der Waals (vdW) interactions

The Ar–Ar interaction is one of the most thoroughly studied atom–atom interactions, and the evolution of the respective potential function is intimately connected with the history of molecular dynamics simulations [209, 207]. Here we choose the HFD–B2 potential obtained by Aziz and Slaman from a multi-property–fit. It exhibits a minimum of $\epsilon = 1.19$ kJ/mol at an internuclear separation of $r_m = 376$ pm [210]. The Ar–Cl interaction is slightly stronger but very similar in range. Neglecting the weak anisotropy of the open shell system (^2P state of the Cl atom), we make use of the $V_{3/2,1/2}$ potential curve of Ref. [211] with $\epsilon = 1.44$ kJ/mol and $r_m = 378$ pm. This potential as well as the model for the Ar–H interaction is determined from (integral and differential) crossed atomic beam scattering experiments. The latter one has an extremely shallow well ($\epsilon = 0.45$ kJ/mol at $r_m = 354$ pm) which is irrelevant for the collision energies considered in the context of the present work.

Note that it would be desirable to include three–body effects, in particular to use a true atom–molecule potential for the Ar–HCl interaction. Indeed, there exists a highly sophisticated atom–molecule potential in the work of J. M. Hutson [212] based on infrared and microwave spectroscopy [213], see Sec. 4.2.1. However, this potential energy surface does not explicitly depend on the H–Cl distance but is given in a vibrationally adiabatic formulation, i. e. as a function of the HCl vibrational quantum number v. Furthermore, it has been fitted to spectroscopic data for $v = 0$ and $v = 1$ only. As will be shown in Appendix C.1 this potential function already shows considerable deficiencies for $v = 3$.

Ionic interactions

The interaction of alkali halogenides can be approximated relatively well as a sum of pairwise interionic potential functions which are independent of cluster size and shape. To describe the interaction between a pair of ions i and j at distance r_{ij}, we use a simple Born–Mayer potential of the form

$$V_{ij}(r_{ij}) = \frac{1}{4\pi\epsilon_0}\frac{q_i q_j}{r_{ij}} + A_{ij}\exp\left(-\frac{r_{ij}}{\rho}\right) \tag{3.9}$$

where the first term gives the Coulomb interaction assuming $|q_+| = |q_-| = e$ and where the second term stands for the repulsion caused by the overlap of the electron clouds. In each case, the range parameter is the same ($\rho = 33.7$ pm). The parameters A_{ij} giving the steepness of the repulsion were determined by Tosi and Fumi [214]. The values are $A_{++} = 1555.21$ eV, $A_{--} = 1924.80$ eV, and $A_{+-} = 1786.91$ eV.

Note that the neutral K–Cl potential is not taken into account here because the collision energies considered are clearly below the energy of the neutral KCl pair potential. Furthermore, polarisation effects are neglected.

3.3 Atom–Cluster Reactions

3.3.1 One Atom Acting as a Solvent

Introduction

As a first step in our investigation of solvent–induced stabilization of collision pairs, we want to focus our attention on the simplest possibility, i. e. the case of an association reaction in a three body collision. In particular, we want to study the HCl formation in the presence of a single Ar atom which is assumed to be attached to the Cl atom before the collision event takes place

$$H + Cl \cdots Ar \rightarrow HCl(v, J) + Ar \tag{3.10}$$

Based on this simple model, we mainly want to study the "third body" or "chaperon" effect. Apart from general aspects of the reaction dynamics of this exotic exchange reaction, we are interested in the following questions.

1. How efficient is the "evaporation" of the Ar atom in stabilizing the nascent HCl molecule, and what is the partitioning of the energy release between the three degrees of freedom, i. e. vibration and rotation of the HCl and translation of the Ar?

2. What are the reaction mechanisms, and how are they reflected in the internal or external degrees of freedom of the reaction products?

3. Finally, are there any long–lived HCl$\cdots$Ar complexes, and what role do they play?

In passing we note that our model system (3.10) has many analogies to the H + F_2 reaction which has been the "drosophila" of chemical reaction dynamics over the last few decades, see the book by Levine and Bernstein [13] as well as a recent review [215]. While the reduced masses are very similar, the disparity of the reagent vs. product bond strength and hence the excess energy is even more extreme for the system considered here.

Cross Sections

Total reactive cross section for the HCl formation are shown in Fig.3.2 (a) for a range of different collision energies $E_{\rm rel}$. It can be seen that the results for $\sigma_{\rm ass}(E_{\rm rel})$ strongly decrease with increasing collision energy $E_{\rm rel}$. While for the slowest collisions ($E_{\rm rel}$ = 1 kJ/mol) we observe very large cross sections of 17.5×10^{-20}, the reactivity declines down to 2×10^{-20} m^2 at a collision energy of $E_{\rm rel}$ = 50 kJ/mol. This monotonic decrease of $\sigma_{\rm ass}(E_{\rm rel})$ is typical for the reaction dynamics on a potential energy surface exhibiting no barrier between product and reagent region. Hence, this type of reaction is mainly governed by dynamical considerations. More specificially, the centrifugal barrier rules the capture of the H atoms by the attractive HCl potential. In the framework of a Langevin model it can be shown that the cross section decreases like

$$\sigma_{\rm ass}(E_{\rm rel}) \sim E_{\rm rel}^{-2/s} \tag{3.11}$$

if a power law $V(r) \propto r^{-s}$ is assumed for the long range attraction [13]. In the present case, our cross sections cannot be fitted exactly to such a model function which points to the more complicated details of the reaction dynamics considered here, in particular to the role of the "microsolvation".

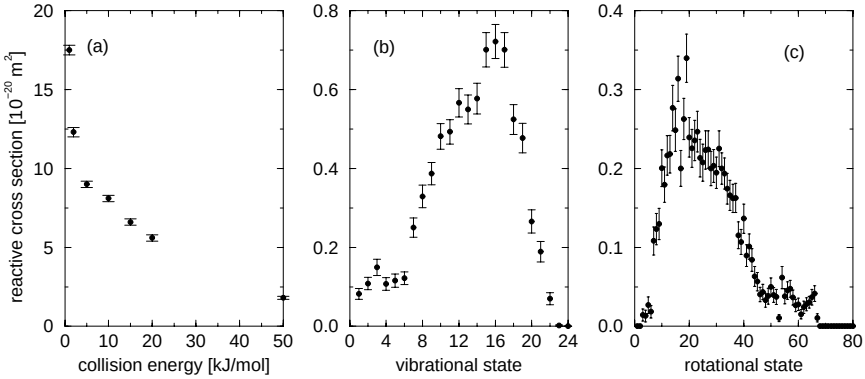

Figure 3.2: Total and partial cross sections for the HCl formation in the $H + Cl \cdots Ar \rightarrow HCl(v, J) + Ar$ reaction. Panel (a) shows the total cross section versus collision energy. Panels (b) and (c) show partial cross sections vs. vibrational (v) or rotational (J) state, respectively, for a fixed collision energy of 10 kJ/mol. The error bars indicate the Monte Carlo error, see Eq. (3.5). From B.1

Although the cross sections are large enough to be detected in typical beam experiments, they are nevertheless relatively small compared with the range of the attractive HCl forces. This behaviour is caused by the following two reasons. First, the potential energy coupling between the H–Cl and the Ar–Cl motion is very weak. Second, there are also kinematic restrictions for the H + Cl...Ar system. In a light–heavy–heavy system the energy transfer from a light–heavy mode to a heavy–heavy mode is typically not very effective [216]. In principle, this energy transfer can be enhanced by replacing the light collision partner, e. g. we found that replacing H by D increases the reactive cross sections by about 20%. Consequently, the reactivity can be expected to be much higher for the association of dihalogenides.

The energy transfer to the Ar solvent atom can be characterized in a more quantitative way by considering partial cross sections for the HCl(v, J) formation with respect to a specicific vibrational or rotational state of the product molecule, see Fig. 3.2 (b,c). For a fixed collision energy ($E_{\mathrm{rel}} = 10$ kJ/mol) the vibrational distribution is highly inverted with a maximum at $v = 16$. The corresponding vibrational energy of 395.5 kJ/mol represents 87% of the dissociation energy of the HCl molecule. Another intriguing feature of Fig. 3.2 (b) is that the distribution of product vibrational states is very broad reaching from the third highest state ($v = 22$) down to the second lowest state ($v = 1$). The distribution of product rotational state is shown in Fig. 3.2 (c) for the same collision energy. It shows a steep rise up to $J \approx 20$ and a long tail reaching

up to $J \approx 70 \cdots 80$. The rotational energy of 53.6 kJ/mol corresponding to the maximum at $J = 20$ is equivalent to 12% of the dissociation energy. With a few exceptions the data points can be fitted very well by a Boltzmann–type distribution. This leads to a fictitious temperature of more than 13 000 K.

We can conclude that on average the cooling by evaporation of a single weakly bound solvent atom is not very efficient. However, there is a small probability that the HCl molecule is cooled also to very low quantum states. As a rule of thumb we can state that in the order of 90% and 10% of the excess energy is found in vibration and rotation, respectively. Only about 1% can be expected for the translation of HCl and Ar relative to each other.

Reaction mechanisms

Although the portion of excess energy that is found in product translational energy is very low, it can be one of the most powerful tools in determining the underlying reaction mechanism [12, 13]. A first interesting hint is found in Fig. 3.3 (a). The distribution of final velocities in the center of system shows a bimodal behaviour, with two maxima at approximately 0.2 km/s and 0.7 km/s. Also the angular distribution of the HCl molecular product exhibits a bimodal behaviour with a main peak for backward scattering and small secondary maximum representing forward scattered molecules. The correlation between velocity and angular distribution is revealed in a two–dimensional velocity map (not shown). It turns out that the forward–scattered HCl moieties are faster than the backward–scattered ones.

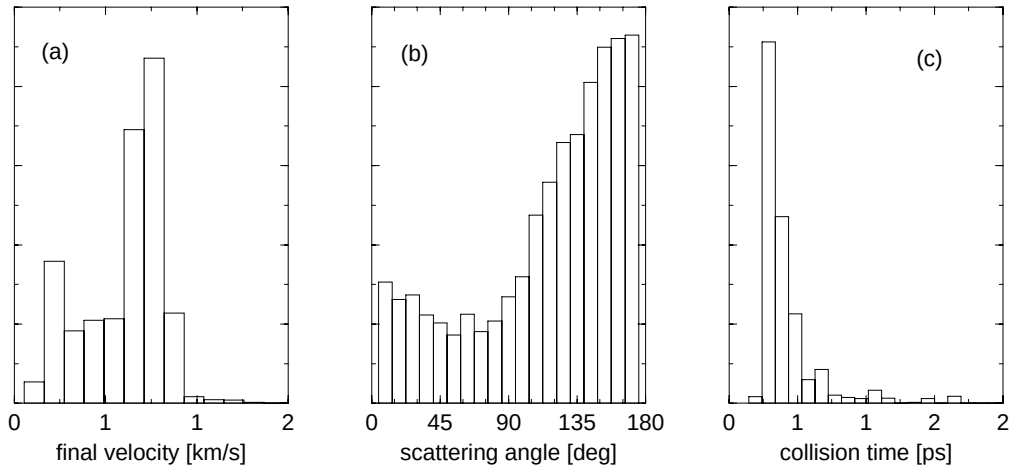

Figure 3.3: Panels (a) and (b) show the velocity and angular distribution of HCl molecules formed in $H + Cl \cdots Ar \rightarrow HCl(v, J) + Ar$ reactions at a collision energy of 10 kJ/mol. Panel (c) shows the distribution of collision times. From B.1

A further inspection of a large number of individual trajectories ($E_{\mathrm{rel}} = 10$

kJ/mol) reveals the following details on the reaction mechanism (see Fig. 4 of B.1). First of all, the H atom is attracted in the well of the HCl ground state interaction and is forced onto a rosette–like orbit with the Cl atom at its center. This corresponds to extremely highly excited or metastable HCl. In the coarse of this spiraling motion the H atom collides one or more times with the Ar atom. These collisions can be direct ("hard") collisions, but grazing ("soft") collisions are observed more often. Note that the temporal order of capture and cooling represents a key issue for the process. In order to understand this we have to consider the maximum energy transfer in a hard collision

$$\frac{\Delta E_{\max}}{E} = 4\frac{m}{M} \tag{3.12}$$

where m and M are the masses of the light and heavy collision partner, respectively. For a mass rations of 1:35 or 1:40 the relative energy transfer is limited to $\approx 10\%$. Hence, the larger energy transfers of a few ten up to a few hundred kJ/mol resulting in HCl molecules in low (v, J) states can be traced back to situations where a considerably accelerated H atom collides with the Ar atom.

Second, the scattering direction of the HCl molecules is mainly dictated by the initial orientation of the Cl$\cdots$Ar aggregate. This is not too surprising when one compares the mass of hydrogen with that of chlorine or argon. Also the timescale of the Cl$\cdots$Ar rotation is much slower than that of the H atom collision.

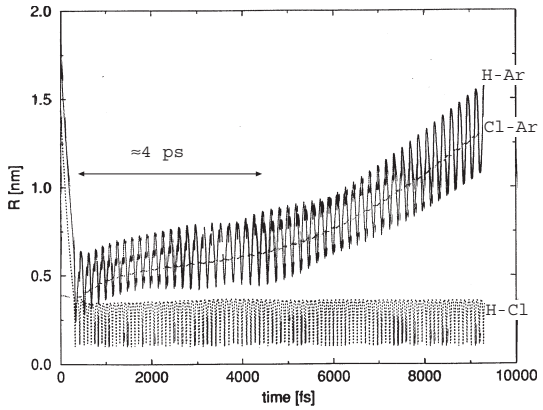

Figure 3.4: Formation of a long–lived complex in a H + ClAr collision for $E_{\text{rel}} = 10kJ/mol$

An interesting situation arises when the initial orientation of the Cl$\cdots$Ar cluster is perpendicular to the direction of the incident H atom and when the collision energy is such that it nearly coincides with the height of the centrifugal barrier. Under these favourable circumstances metastable rotating HCl$\cdots$Ar complexes can be formed with the HCl bond rotating in a plane perpendicular to the Cl$\cdots$Ar axis, see Fig. 3.4. In this geometry, the coupling between the HCl vibration/rotation and the Cl$\cdots$Ar degrees of freedom is minimized thus resulting in relatively long lifetimes. Results from our MC averaging over a

large number of trajectories are shown in the right part of Fig. 3.3. While the majority of the collision events is over after $\approx$ 0.5 ps, there are quite a few long–lived events up to 1.7 ps. Even collision times of 10 ps and more have been observed for individual cases. However, due to the complicated steric restrictions, resonance–like states are much less important here than for the case of the diatomic photoassociation, see Sec. 2.3.6 on the role of shape resonances.

3.3.2 The First Solvation Shell

Introduction

After having considered the extreme case of a single atom acting as a solvent we nowproceed to investigate the case of a first complete solvation shell. It can be rationalized by closest packing arguments, that twelve Ar atoms are needed to form the first complete solvation shell around the Cl atom at the central position. In order to form a HCl molecular product, the H atom will have to penetrate the cage formed by the first solvation shell where one or more Ar atoms may evaporate

$$H + Cl \cdots Ar_{12} \rightarrow HCl(v,J)Ar_{12-m} + Ar_m, \quad m \leq 12 \quad . \tag{3.13}$$

Hence, our main questions will be the following:

1. How efficient are the twelve Ar atoms in shielding the Cl atom from the H atom colliding with the cluster, or how important is the cage effect on the HCl association reaction?

2. How does the efficiency of caging depend on the cluster temperature and on the cluster structure?

3. Finally, how effective is the cooling induced by a complete solvation shell compared with the case of a single solvent atom, and how many of the solvent particles are kicked out of the cluster?

Reaction Mechanisms

In the following we want to discuss two different events in collisions of hydrogen atoms with the $ClAr_{12}$ cluster occuring at totally different collision energies. First let us restrict ourselves to the situation at $T = 0$, and let us postpone the question of temperature effects to the following subsections.

At very low impact energies physisorption of the H atom on the surface of the cluster is the dominating process, see Fig. 3.5 (a). An incoming H atom is attracted by the cluster through the vdW forces. For a collision energy of $E_{\rm rel} = 0.1$ kJ/mol the cross section for this process can be very large (3×10^{-18} m^2) which is twice as large as the geometrical cross section of the cluster.

Upon trapping on the surface, the H starts to move almost freely on the cluster surface but avoiding the corners of the icosahedron (C_5 axes). In the course of this motion the H is slowly loosing energy. When its energy is not sufficient any more to overcome the small barriers ($\approx$ 0.5 kJ/mol) at the edges

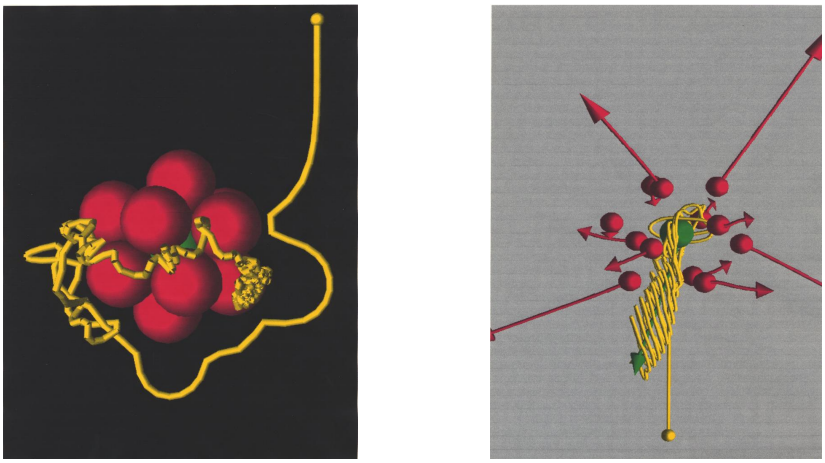

Figure 3.5: Typical reactive trajectories for the $H + ClAr_{12}$ collision pair for two drastically different collision energies. (a) Adsorption of H atoms on the surface of the cluster at extremely low collision energies ($E_{\rm rel} = 0.01$ kJ/mol). (b) Penetration of the Ar cage at much higher collision energies ($E_{\rm rel} = 100$ kJ/mol). The HCl collision pair is stabilized by evaporation of the complete solvation shell.

of the icosahedron (C_2 axes), it becomes trapped at a site at the center of one of the faces (C_3 axes). This physisorbed state is quite stable, and evaporation of the hydrogen occurs on a timescale of 100 ps to 1 ns. During this lifetime of the complex, there is no diffusion of the hydrogen atom to the interior of the cluster. Hence, hydrogen chloride cannot be formed. It remains to be seen, whether quantum–mechanical tunneling could play a role to yield reactivity on a timescale faster than the decay of the complex.

It is clear that the above process of physisorption is limited to relatively low collision energies. In our simulations we have shown that the collision energies must be less than the strength of the vdW attraction between H and $ClAr_{12}$ which is of the order of 1 kJ/mol. For a detailed investigation of the atom–cluster potential, see Fig. 6 of B.1.

At higher energies the cluster becomes partly "transparent" for the incident H atoms, see Fig. 3.5 (b). The lowest threshold value for cage penetration is found for an approach of the H projectile along the C_3 axes. For a collision energy of 100 kJ/mol, there are windows of about 10^{-20} m^2 at each of the 20 faces of the icosahedron. An incoming H atom can penetrate the cage upon an almost central collision ($b \approx 0$). Inside the cage formed by the Ar atoms, the H atom is strongly attracted by the chemical forces. The nascent HCl diatomic molecule is in a highly excited ro–vibrational state. In the course of its large–amplitude motion the H atom pushes the Ar atoms away with fragment energies between 0.2 and 20 kJ/mol. After a typical timescale of 2 ps all the solvent particles have evaporated where sometimes Ar dimers or trimers may be formed. It is not too surprising that the stabilization of HCl collision complexes by evaporation of twelve Ar atoms is more effective than by evaporation of a

single Ar atom as discussed above.

It has to be emphasized, however, that this type of reactive event is limited to almost central collisions and to favourable orientation of the cluster. It can be seen from the weighting factor b in equation 3.4 on page 54 that central collisions are negligible. Hence this type of reaction does not play a role in the averaging procedure to obtain reactive cross sections. We will, however, come back to the question of cage penetration for finite temperatures ($T > 0$) after having discussed the thermal properties of the $ClAr_{12}$ cluster in the following subsection.

It is interesting to compare our findings with other work on reactive atom–cluster collisions: In their work on I_2 formation in I + IAr_{12} collisions Hu and Martens find no cage effect [178, 180, 182]. Similar findings were also made in more recent work by Jungwirth on Cl_2 formation from reactive Cl + $ClAr_{12}$ collisions [217]. This apparent contrast can be resolved by simple kinematic considerations. The incident halogen atom is much heavier than the H projectile. Hence, it can push solvent atoms aside such as to undergo geminate recombination. Another difference stems from the atom–cluster potentials involved. Iodine atoms are attracted by the Ar solvent much stronger than H atoms [181]. Hence, the solvent actually increases the rate of capture [180] and leads to large cross sections, e. g. 36.6×10^{-20} m^2 for a collision energy of 104.6 kJ/mol.

Thermal and Structural Properties of the $ClAr_{12}$ Cluster

In analogy to the case of pure Ar clusters, where icosahedral packing is well established both in experiment [218,219] and theory [220,221], we find an icosahedral minimum energy structure for the $ClAr_{12}$ aggregate where 12 Ar atoms form an icosahedral shell around the central Cl atom (I_h). Based on the pair potentials introduced above, the binding energy corresponding to the global minimum energy of this aggregate (–53.9 kJ/mol) is slightly lower than that of the pure Ar_{13} cluster. It is noted that the potential energy surface for the heterogeneous system has a local minimum (–52.7 kJ/mol) corresponding to a configuration with the Cl atom located at one of the corners of the icosahedron (D_{5h}).

In order to characterize the thermal behaviour of the $ClAr_{12}$ we perform standard molecular dynamics (MD) simulations for various temperatures proceeding in the following steps [207]. (1) As initial configuration for the MD runs we choose the I_h global minimum energy structure and slowly heat (or cool) the system by performing MD simulations while scaling the velocities. This is done until the kinetic energy E_{kin} corresponds to the desired temperature

$$T = \frac{2}{3N-6}\,\frac{E_{\mathrm{kin}}}{k_B} \tag{3.14}$$

where $N = 13$ is the total number of atoms and k_B stands for Boltzmann's constant. (2) To allow the system to equilibrate after this heating or cooling, we continue to propagate the trajectories for another 50 ps. (3) Subsequently,

statistical averaging can be performed. We run the trajectories over a long period of 10 ns (or 1 ns for the highest temperatures) and sample various thermal or structural properties of interest at regular intervals. Assuming ergodicity, these time averages should be equivalent to microcanonical ensemble averages. Again Eq. (3.14) is used to assign temperatures which, however, do not deviate considerably from those adjusted before the equilibration.

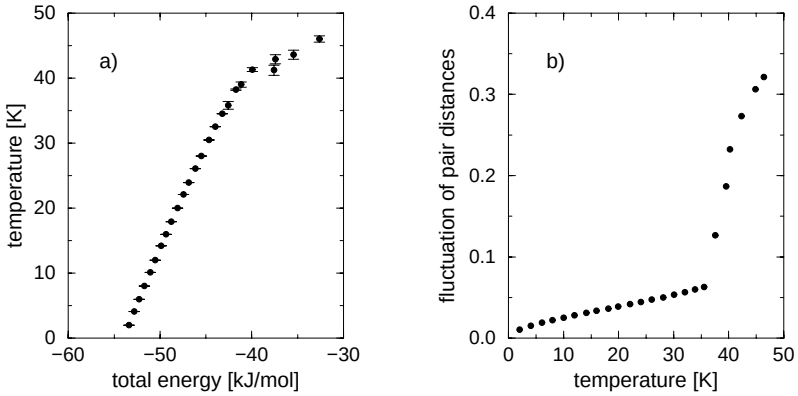

Figure 3.6: Thermal and structural properties of the $ClAr_{12}$ cluster obtained from MD simulations. (a) Caloric curve, see Eq. (3.14). (b) Relative rms fluctuations of all pair distances, see Eq. (3.15). From B.1

As a first means to characterize the thermal behaviour of the cluster we want to consider the caloric equation of state. It is obtained as the temperature (3.14) vs. the total cluster energy. It can be seen in Fig. 3.15 (a) that this function rises linearly up to a temperature of 36 K. This indicates a constant heat capacity which can be obtained as the inverse of the slope $c = \partial E_{\mathrm{tot}}/\partial T$. At higher temperatures, the slope appears to decrease and the statistical fluctuations increase suddenly. For $T > 46$ K evaporation of single atoms from the cluster becomes dominant.

In order to characterize the transition occuring at $T \approx 36$ K more in detail, we consider a structural quantity, i. e. the root–mean–square (rms) fluctuation of pair distances of the N atoms in the cluster

$$\delta = \frac{2}{N(N-1)} \sum_{i \neq j} \frac{\sqrt{< r_{ij}^2 > - < r_{ij} >^2}}{< r_{ij} >} \tag{3.15}$$

where $< r_{ij} >$ and $< r_{ij}^2 >$ stand for the time average of a pair distance r_{ij} or its square, respectively, and where the summation extends over all pairs of atoms i and j. This (dimensionless) number is often used as a measure for the mobility of particles. In particular, for bulk matter there exists an empirical criterion claiming that solid and liquid state can be distinguished by $\delta < 0.1$ or $\delta > 0.1$, respectively [222]. Fig. 3.15 (b) shows our MD results for the $ClAr_{12}$ cluster. We see a slow rise of δ proportional to the temperature reaching $\delta = 0.06$

at $T = 36$ K reflecting the thermal expansion of the system. Beyond this temperature, there is a sudden rise of this quantity finally reaching $\delta = 0.32$ at $T = 46$ K.

This dramatic rise of the flexibility of the cluster can be regarded as an analogue to the melting transition of condensed matter which is further confirmed by inspection of a number of snapshots of cluster configurations in the course of the MD simulations (see Fig. 8 of B.1) as well as radial distribution functions (see Fig. 2 of B.2). It turns out that for a temperature of 40 K ($\delta = 0.23$) the Ar atoms have already gained some mobility and undergo large–amplitude vibrational motion around their equilibrium positions but the icosahedral structure basically remains intact. For $T = 45K$ ($\delta = 0.31$) this picture completely changes. Now there are sometimes atoms ejected from the first solvation shell which then occupy a position in the second shell. For this reason, the remaining eleven atoms in the first shell can almost freely rearrange. In particular, we also observe configurations with the Cl atom at the outside of the cluster similar to the local minimum of D_{5h} symmetry mentioned above.

We conclude that there is a structural transition from a solid–like phase to a liquid–like phase between $T = 40$ K and $T = 45$ K of $ClAr_{12}$. Similar observations of a melting–like transition have also been made for the analogous homogeneous Ar_{13} cluster where a transition temperature of 34 K was found [223, 224]. The lower transition temperature is caused by the use of a different interaction potential with a lower well depth. The question of a phase coexistence of solid and liquid behaviour which has been proposed for Ar_7 [225] and for Ar_{13} [196] has not been addressed here due to less extensive data.

Temperature Effects on the Reactivity

Once having characterized the thermal and structural properties of the $ClAr_{12}$ cluster, we now want to discuss the reactivity in collisions with H atoms as a function of the cluster temperature. This is achieved by using a sample of configurations from our MD simulations as input for the MC integration $\int d\mathbf{v}$ to obtain reactive cross sections, see Eq. (3.4). Our results for the temperature dependence of the total reactive cross section for HCl formation is shown in Fig. 3.7. Let us first consider the case of $E_{\mathrm{rel}} = 10$ kJ/mol represented in the left part of the figure. This energy is well below the threshold for cage penetration at $T = 0$. Consequently, we detect no reactivity for $T = 0 \ldots 20$ K. The data points for $T = 30 \ldots 40$ K indicate finite but extremely low reactivity with cross sections below 10^{-20} m^2 which is due to the thermal motion of the Ar atoms around their equilibrium possibilities. This situations completely changes for temperatures above the melting–like transition of the $ClAr_{12}$ aggregate. At these temperatures the large cross section of 11.4×10^{-10} m^2 indicates the breakdown of the cage effect. This is caused by the free mobility of the Ar atoms in the liquid–like cluster. It is clear that configurations with holes in the first solvation shell and, in particular, configurations where the Cl atom resides on the outside of the cluster contribute to the high reactivity.

This sudden onset of the reactivity at the transition temperature has to be contrasted with the situation for higher impact energies. A typical result for

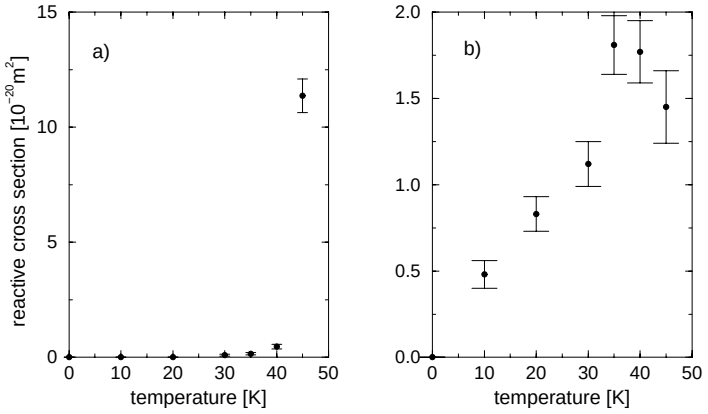

Figure 3.7: Temperature dependence of the total reactive cross section for the $H + ClAr_{12} \rightarrow HCl + 12Ar$ association reaction for two different collision energies of the reactants. (a) $E_{\rm rel} = 10$ kJ/mol. (b) $E_{\rm rel} = 100$ kJ/mol. Note the different scales of the ordinates. From B.2.

$E_{\rm rel} = 100$ kJ/mol is shown in Fig. 3.7 (b). It has been mentioned previously that this collision energy is well above the threshold for cage penetration for the rigid cluster, but the negligible statistical weight of central collisions results in a vanishing reactive cross section. Heating of the cluster results in a steady rise of reactivity up to $1.5 \ldots 2 \times 10^{-20}$ m^2. However, within the uncertainty associated with the Monte Carlo error there is no further increase of the reactivity beyond the transition temperature. This can be explained by a steric effect. On the one hand, the exposure of the Cl atom on the outside of the cluster is expected to lead to enhanced reactivity for H atoms approaching from favourable directions. On the other hand, there is increased shielding for H atoms colliding from the opposite side. The trade–off of these two effects leads to approximately equal reactivities for temperatures just below and above the transition.

3.3.3 Summary and Outlook

In the present subsection, the (radiation–less) stabilization of collision pairs in the presence of a solvent has been studied. Our emphasis has been on the effect of a "microsolvation" which was modelled by attaching a rare gas "microsolvation" to one of the reagents, see B.1. For the example of the H + Cl$\cdots$Ar system the existence and the extent of the third–body or "chaperon" effect is demonstrated. Already a single solvent atom can stabilize a collision pair by removing some energy from it such as to keep it from redissociating. The corresponding cross sections for associative collisions are certainly large enough to be detected in experiments. In view of the strong attraction on a barrier–less potential energy surface, however, they are moderate which is due to kinematic constraints for the energy transfer from the H–Cl mode to the Cl–Ar mode. Consequently, we find ro–vibrationally very hot products while only a very small fraction of the available energy is found in product

translation. Among the most interesting predictions is the discovery of very long–lived orbiting resonances with lifetimes in the order of picoseconds.

To explore the transition from gas to condensed phase dynamics, the cage effect on association reactions was studied in B.2 for the H + Cl$\cdots$Ar$_{12}$ system where a first complete solvation shell shields the Cl reactant. First of all, structural and dynamical properties of this aggregate were investigated as a function of temperature. We found a pronounced structural transition between $T = 40$ K and $T = 45$ K in MD simulations of ClAr$_{12}$. The reactivity to form HCl molecules in collisions with a H atom can be extremely sensitive to the melting–like transition. Provided the collision energy is not too high, there is a dramatic break–down of the cage effect upon the strucural transition of the solvent cluster. This novel approach can serve to elucidate more on the much debated question of "phase transitions" in finite systems. In this way, reactive collisions could provide an alternative to the spectroscopy of chromophores embedded in solvent clusters.

Future work could be directed along the following directions

1. How does the cage effect and its dependence on the cluster temperature depend on the size of the microsolvation? Investigation of H + ClAr$_n$ collisions with $n = 2 \ldots 11$ could shed light on the onset of the cage effect. Furthermore when approaching the reaction dynamics in bulk matter, one might be interested in the case of more than one solvation shell. Another closely connected question is what would happen if both reactants were "solvated" in a cluster.

2. Another extremely important question is the issue of quantum effects in the nuclear dynamics. For the systems considered her one might wish to know whether tunneling reduces the cage effect. Also the energy transfer from the nascent HCl molecule to the "microsolvation" during the process of vibrational and rotational energy might be affected by quantum effects, especially for the lowest states.

   This type of question could be treated most conveniently using a quantum–classical molecular dynamics (QCMD) approach where the H atom is treated by wavepacket mechanics and the much heavier remaining atoms are treated as classical particles, see our treatment of photodissociation dynamics in Part II of the present thesis.

3. Furthermore, the electronic dynamics of the open–shell ^2P state of the Cl atom has been neglected here. However, in recent work, methods to treat the ^2P state dynamics of halogen atoms in rare gases have been devised [226, 227, 228, 229, 230].

3.4 Cluster–Cluster Reactions

3.4.1 Introduction

This section deals with associative collisions of molecules with clusters and of clusters with clusters to investigate the process of cluster growth from the

gas phase. As a model we choose alkali halides which have also been used in a fairly large number of other studies due to the simplicity of their interaction. In particular, the questions of existence of different isomers, structural transitions, and the transition from clusters to crystals have been studied extensively for this class of systems [231, 232, 233, 234, 235, 236, 237]. Because of the approximately equal size of anion and kation constituents, we choose potassium halide here and we want to focus our attention on two different growth mechanisms. The first one will be the cluster growth by addition of a single KCl molecule to an existing small KCl cluster

$$KCl + (KCl)_n \rightarrow (KCl)_{n+1}\,, \quad n = 1 \ldots 4 \quad . \tag{3.16}$$

which will be termed $n + 1$. The second class of association reactions involves reactive collisions of small clusters of equal size

$$(KCl)_n + (KCl)_n \rightarrow (KCl)_{2n}\,, \quad n = 1 \ldots 4 \quad . \tag{3.17}$$

which will be referred to as $n + n$ associations. Note that the mechanisms of monomer addition $(n + 1)$ and cluster fusion (symmetric growth $n + n$) are the reversed processes of fragmentation and fission common both in nuclear physics and in the chemical physics of clusters [192, 188, 190, 238]. Again we will use the classical trajectory methods to simulate reactive collisions. The statistical averaging procedure (3.4) to obtain reactive cross sections will be employed. In order to facilitate a comparison of the results for different cluster sizes, binding energies as well as collision energies will be given as energies per ion. The latter one will be varied up to a limit of 0.5 eV/ion to guarantee that processes on the neutral potential energy surfaces can be neglected.

3.4.2 Cluster Structures

This subsection discusses the structures of small $(KCl)_n$ $(n = 2 \ldots 4)$ clusters serving as initial conditions for our study of associative cluster collisions. The structures were obtained from randomly chosen initial configuration by simulated annealing. In this procedure, the cooling and finally the freezing of a liquid is simulated by a standard MD computer simulation where the temperature is reduced by periodically scaling down the velocities of the particles until the cluster becomes trapped in the "catchment area" [232] of one of the minima of the potential energy hypersurface.

As a consequencce of the long–range interaction between the ions, the structures of alkali halide clusters differ considerably from those of rare gas clusters which are mostly dictated by closest packing arguments. In particular, the smaller clusters tend to favour less compact structures in order to minimize the repulsion of second nearest neighbours. The most stable KCl dimer is a (near square) rhombic arrangement (–2.8809 eV/ion) , while the most stable trimer is a regular hexagonal ring–like structure (–3.0189 eV/ion). An octagonal tetramer structure is also possible (–3.0655 eV/ion), but a cube–like structure is found to be slightly more stable (–3.1208 eV/ion) which is in agreement with earlier predictions [233, 239]. Moreover, there is also a rectangular

structure of the tetramer which is a little less stable (–3.0614 eV/ion). Hence the tetramer is the critical cluster size where the advantages of compactness becomes more important than the minimization of repulsion. Below this cross–over even chain–like structures are only a few percent less stable than the ring–like arrangements [232]. However, for finite temperatures also for the tetramer less compact structures can become more abundant than more compact ones which was indeed found for $(NaCl)_4$ [232,240] as well as for $(KCl)_4$ [241] where the transition occurs between 600 and 700 K.

3.4.3 Lifetimes of Collision Complexes

In order to assess which collision complexes can be regarded associated into a relatively stable aggregate we first consider the lifetimes of the compound states. Our results for the $n+1$ and $n+n$ cluster collisions are shown in Fig. 3.8 (a) and (b), respectively. In each case, the reagent clusters are assumed to be initially in their most stable configuration. After the first three or four picoseconds the distribution of lifetimes falls off roughly linearly in the semilogarithmic plots indicating an exponential decay law. Furthermore we see that the result for the $1+1$ reaction falls off much faster than the other $n+1$ reactions. Qualitatively, this is in accord with the RRK or RRKM theory [3,5,1]. Based on considerations of statistical deviations from the equipartition of the excess energy among the degrees of freedom, these theories predict the probability that a certain amount of energy is accumulated in a "critical" mode which then leads to decay of the complex. According to these arguments, longer lifetimes should be expected for larger complexes. This trend, however, does not apply to the larger clusters, since the lifetimes of the $2+1$, $3+1$, and $4+1$ collision complexes appear to equal within the statistical errors. This points to the limited predictive power of statistical theories for these relatively small cluster systems. For the symmetrical cluster growth the trends observed in Fig. 3.8 (b) seems even reversed. The lifetime for the $2+2$ complex is by far the longest while the other ones are practically indistinguishable. In this case, the unusual stability of the $(KCl)_4$ complex can be traced back to formation of the especially stable cube–like tetramer.

Another interesting aspect is the dependence of the lifetime of the collision complexes on energy and angular momentum (impact parameter) of the collision event. For this purpose, we define (somewhat arbitrarily) short– and long–lived complexes by having a lifetime of less than or more than 17 ps, which is equivalent to the first few rotational periods. For a detailed analysis we chose the example of the $(2+1)$ collision, see Figs. 2 and 3 of B.3. It is shown that long–lived complexes are formed preferentially for low energy *and* small impact parameters. where the borderline exceeds further towards higher impact parameters for the lowest collision energies. This indicates that the main decay mechanism is centrifugal distortion. Upon forming an initially compact collision complex, the compound cluster is stretched into a chain–like configuration until finally one of the bonds breaks apart.

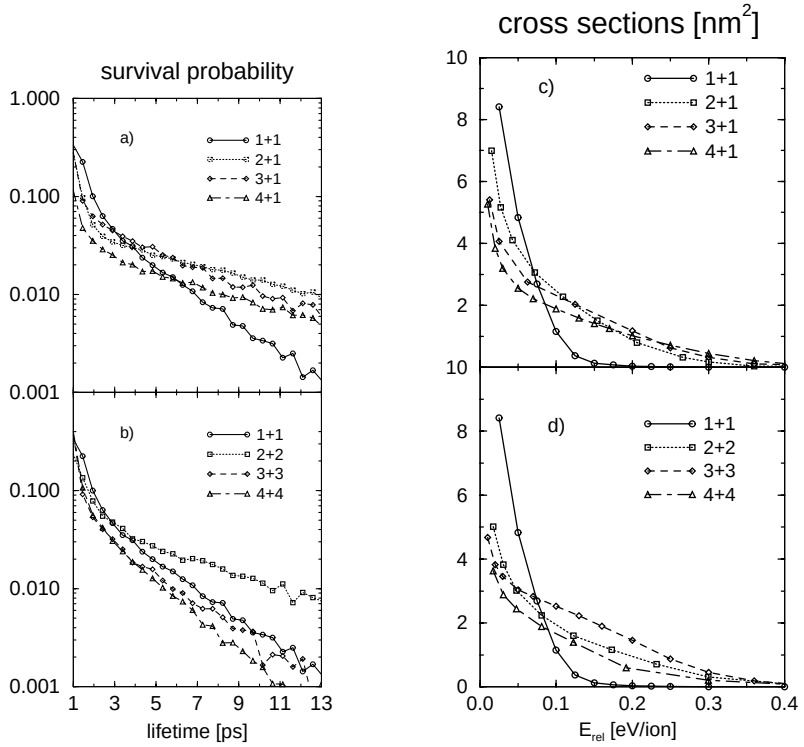

Figure 3.8: Product survival probabilities and associative cross sections for various $KCl_n + KCl_m$ cluster–cluster collisions. The left panel shows distributions of lifetimes of collision complexes for $n + 1$ (a) and $n + n$ (b) additions for $E_{\rm rel} = 0.3$ eV/ion. The right panel shows the energy dependence of the reactive cross sections for the same collision pairs. From B.3

3.4.4 Association Cross Sections

In this subsection we restrict ourselves to the formation of long lived complexes (> 17 ps) which can be considered as models for permanent associations if an additional cooling mechanism were present. Again, we assume that the clusters are initially prepared in their energetically lowest configuration. Reactive cross sections versus collision energy are shown in Fig. 3.8 (c,d). The cross sections are very large for the lowest energies. For $E \approx 0.01$ eV/ion, they adopt values of $10 \times^{-18} \ldots 10\times^{-17}$ m^2. For larger energies, the cross sections are rapidly falling off. This feature is similar to the behaviour of the H + ClAr reaction studied previously where the reactivity is only limited by the centrigugal barrier [13]. Hence we can conclude that although the reagents are electrically neutral, association takes place where the orientation of the collision partners is such that interaction of the higher electrostatic moments (dipole, quadrupole, ...) is attractive. When analyzing the cross sections for the $n+1$ and $n+n$ reactions in more detail, we find that they are controlled by two opposing trends.

1. For low collision energies ($E < 0.1$ eV/ion) we find huge cross sections for small collision partners and decreasing cross sections for increasing size of

the reagents. This can be intuitively understood by considering the nature of the interaction between the reagents. In particular, the cross section for the initial capture of the collision partners to form a complex is determined by the lowest non–vanishing electrostatic multipole moment. For example, consider the smallest collision system $1 + 1$. For not too small cluster–cluster distances and for favourable orientations, the attrative dipole–dipole interaction scales as $-r^{-3}$. This has to be compared with the largest collision pairs in the n+1 and n+n class considered here. Assuming the cube–like configuration of the tetramer, the dipole–octupole attraction for the $4 + 1$ system and the octupole–octupole attraction for the $4 + 4$ system decrease as $-r^{-5}$ or $-r^{-7}$, respectively. When considering the rectangular tetramer instead of the cube–like one, we obtain larger cross sections for the $4 + 1$ due to the dipole–quadrupole interaction ($-r^{-4}$), see Fig. 5 in B.3.

2. For high collision energies ($E > 0.1$ eV/ion) this trend is reversed. Here the influence of the capture cross section is less important than the stability of the collision complex with respect to decay during the period of 17 ps. For the smallest system $(1 + 1)$ the cross section practically vanishes for $E > 0.2$ eV/ion. The larger systems show much larger cross sections because they have more internal degrees of freedom among which the excess energy can be redistributed. However, the validity of this type of statistical arguments is again limited. Considering the $n + 1$ and $n + n$ systems for $n = 2 \ldots 4$, we find that the ordering of the cross sections does not exactly correspond to the size of the collision partner.

3.4.5 Summary and Outlook

Associative collisions of alkali halide molecules and clusters are studied in B.3 as a model of cluster growth from the gas phase. In contrast to the atom–cluster systems investigated previously the collision complexes treated here are large enough to redistribute the excess energy among their abundant internal degrees of freedom for a much longer time before they finally are stabilized by evaporation. The cluster sizes considered here (up to the tetramer) are on the border of the validity of statistical RRKM models. While general trends can be explained in terms of these models, a detailed microscopic study is necessary to understand the quantitative effects. In particular, the nature of the mutual attraction of the reactants plays an important role.

The present study represents a first attempt to characterize the process of cluster growth and cannot be very exhaustive, by any means. In particular, the following points should deserve attention in future work.

1. The Born–Mayer potentials used here are a relatively crude model for the interaction in an ionic cluster. In particular, polarization effects have been neglected. However, on the basis of previous studies [241] we expect the changes by including this mechanism to be very small and not to change the overall picture of the reaction dynamics.

2. An interesting question is that of other mechanisms of stabilization. Apart from the particle loss which was considered here, collision complexes could also be cooled in third–body collisions, see our work on atom–cluster–collisions in the previous subsection. Another possible stabilization mechanism could be spontaneous emission of electromagnetic radiation. Although this process is usually considered to be very slow, see the work on H_3^+ complexes [59], spontaneous emission could be more important for the alkali halide clusters with their relatively strong electrostatic moments.

3. Finally, in this list of questions it is intriguing to find out for which size of the system is a statististical RRKM treatment valid?

To further illustrate the dynamics of cluster–cluster collisions investigated here we produced computer animations which can be viewed as MPEG movies in the *World Wide Web* on the authors homepage (http://userpage.chemie.fu-berlin.de/∼bschmidt).

Chapter 4

Photodissociation of Molecules in Clusters and Matrices

4.1 Motivation

After having investigated the photo–induced "making of molecular bonds" (photoassociation reactions) in Chap. 2, we now want to study the reversed process, i. e. the light–induced "breaking of molecular bonds". In analogy to the studies of solvent–induced "making of molecular bonds" in chapter 3 of this thesis, we want to study the reaction dynamics of photodissociations at the transition from gas phase to condensed phase. In particular, our model systems shall be guest–host systems, where a (small) solute molecule is embedded in a cluster or a matrix of solvent particles. In analogy to the cage effect on association reaction, where the reactants may be shielded from each other by the presence of the solvent, there is also a cage effect on photodissociation reactions whereby the separation of photofragments is delayed or even hindered. The notion of this cage effect dates back to the 1930s [49]

The description of permanent bond breaking is, for the most part, controlled by the cage exit dynamics of the photofragments. Here and in the following we want to use the following classification of cage exit processes:

1. A **direct cage exit** is defined as an elastic process where photofragments escape from a solvent cage without notably deforming it. Depending on the orientation of the molecule to be photolyzed, the cage exit can be either **immediate** or **delayed**. In the latter case, the photofragments undergo "rattling" oscillations within the cage before finding the exit.

2. If there is considerable energy transfer during these "rattling" vibrations we define this event as an **indirect cage exit** where the cage deformations lead to enlargement of "windows" through which the fragments eventually escape.

In the following we want to focus our attention on a prototypical class of systems for which the photodissociation dynamics has been thoroughly studied over the past few years, namely hydrogen halide molecules in a rare gas environment. For further reading, we refer to review articles on photodissociation in rare gas clusters [174, 55, 242] and in rare gas matrices [243, 244, 245]. The motivation for the choice of these systems mainly stems from two reasons.

1. Owing to the simple electronic structure of the guest molecules as well as to the transparency of the host rare gas systems in the eligible frequency regime, the spectroscopy of these systems is very well understood and most of the theoretical studies so far rely on model systems constructed from relatively few and well–known electronic states[1]. As a matter of fact, the availability of precise pair potentials is one of the most important criteria for choosing rare gas–hydrogen halide systems as model systems in a large number of studies of solvent effects on molecular spectroscopy and dynamics.

[1]Note that we do not consider He or Ne because we want to restrict the investigation of quantum effects to the solute molecule only.

2. Due to the presence of the light hydrogen photofragment, quantum effects can be expected to play an important role in the nuclear dynamics which is the main focus of our interest. Because of the smallness of the hydrogen photofragment, these systems represent possible candidates for the effect of direct cage exit (immediate or delayed) on a relatively short time scale, so that models not accounting for electronic relaxation and recombination can be used, at least within certain limitations. Hence, this class of systems is complementary to another protypical system commonly used for the study of solvent effects on photochemistry, i. e. molecular iodine in rare gas environments. For the latter, quantum effects on the nuclear dynamics are much less pronounced, and the photodissociation dynamics is dominated by indirect cage exit mediated by inelastic collisions of photofragments with the solvent. On the other hand, non–adiabatic transitions between a substantial number of electronic states involved determine the dynamics of these system to a large extent [246, 247, 248, 249, 250, 251, 252, 253, 254, 255, 256, 257, 258].

Even the smallest system with only a single rare gas atom has received considerable attention in recent years in the context of the effect of a "single atom solvent" [259,260,261,262,263,264,265,266,267,268,269,270]. Furthermore, the attractiveness of these systems stems from a methodological aspect: The photodissociation dynamics of hydrogen halides in rare gas clusters has also become a reference system for the development of various exact or approximate models of quantum molecular dynamics (QMD) that allow also simulations of larger systems, i. e. with a larger number of rare gas atoms up to the limit of a rare gas matrix. These include classical [271], quasi–classical [272, 273], quantum–classical (QCMD) [274,259,261,262], quantum–semiclassical (QSMD) [263] and density matrix [275] studies. In other work, a full quantum treatment with separability assumption (TDSCF) [266] has been used. Yet another approach is the use of statistical theories to describe the cage exit [276]. Finally, we also mention the non–adiabatic molecular dynamics models based on classical trajectories with "surface hopping" allowing the treatment of non–adiabatic transitions induced by the effect of spin–orbit coupling [226, 230, 277, 278].

All of the studies quoted above assume the guest molecules to be in their ro–vibrational ground state prior to the excitation into the disscociative state. With very few exeptions, the photodissociation dynamics of rare gas hosts with ro–vibrationally excited guest molecules represents a virtually unexplored field. The emphasis of the present chapter will be on the dependence of the photodissociation dynamics on the initial ro–vibrational quantum state of the guest molecule and on possible control mechanisms resulting from it.

The work presented here is related to the concept of vibrationally mediated chemistry where specific branching ratios of competing reaction channels are controlled by vibrational pre–excitation of certain modes of the reactant(s) [279,280,281,282,283,284,285]. An especially promising approach which shall be followed here is the generalization of this concept to the large amplitude librational/rotational motion of the guest molecules with respect to the rare gas solvent. It is known from infrared spectroscopy that – in contrast to most larger

molecules [2] – matrix isolated hydrogen halide molecules are only very weakly hindered in their rotational degrees of freedom [287, 288, 289, 290]. For the smallest clusters of a hydrogen halide molecule with one or two rare gas atoms there are large amplitude librational (bending) motions of the guest molecule. It is intuitively clear, that by preferential orientation of guest molecules towards "walls" or "windows" of the surrounding solvent cage, the quantum yield of photodissociation should be controllable. So far, there is only indirect evidence from matrix experiments: The anomalous temperature effects which were observed for Cl_2 in Xe [291], F_2 in Kr [292], and for O_3 in Ar [293] have been interpreted in terms of orientational locking of the guest molecules at low temperatures which is overcome by librational/rotational excitation at higher temperatures.

The material presented in the subsequent sections is organized in the following way. After presenting our models and methods (Sec. 3.1), we make an excursion into the field of vibrational (Sec. 3.2) and rotational (Sec. 3.3) spectroscopy of molecules in clusters and matrices. Based on this knowledge of the initial state, we then proceed to the quantum dynamics of photodissociation reactions (Sec. 3.4).

4.2 Model and Interactions

4.2.1 Ground State

The interaction of a hydrogen halide molecule (HX, X = F, Cl) and the n rare gas atoms (Rg) in our model systems is relatively weak and is known to be dominated by pairwise interactions of the (closed shell) constituents. Hence, it can be approximated as a sum of pairwise solvent–solute and solvent–solvent interactions. This greatly facilitates the construction of the total potential energy surface (PES) for the electronic ground state which is represented by

$$V_g(v) = V_{HX(v)} + \sum_{i=1}^{n} V_{Rg_i HX(v)} + \sum_{i<j} V_{Rg_i Rg_j} \quad . \tag{4.1}$$

It is noted that there are a few recent reports pioneering also the effect of three–body interactions beyond the pairwise approach. These include the Axilrod–Teller–Muto term for the Ar–Ar–Ar interaction [294] as well as further contributions to the induction of Ar_2HX [295, 296, 297]. In any case, the effect of these interactions on the vibrational frequency shifts investigated in Sec. 4.4 are relatively small. Furthermore, they seem to decrease for increasing cluster size [294].

To model the solvent–solvent interaction $V_{Rg_i Rg_j}$, a reliable Ar–Ar potential is required. There has been a long history of determining this particular potential function, during which the Ar–Ar interacton has become the most widely studied prototypical system. In particular, the goal was to find a single (and unique) function which is able to reproduce all available experimental microscopic (i. e. spectroscopy, total and differential scattering cross sections)

[2] Note that there is a transition regime between quasi–freely rotating and non–rotating molecules in matrices, where molecules induce pseudo–rotations of the cage [286].

and macroscopic (i. e. thermodynamic, virial coefficients, transport properties) data at the same time, for an overview see Ref. [209, 207]. In the present work, we use the HFD–B2 model for the Ar–Ar pair potential function from the literature which is based on very sophisticated multi–property fits [210].

Moreover, we can benefit from the fact that the solute–solvent interactions $Rg_iHX(v)$ for the systems Ar–HF and Ar–HCl are among the most accurately known atom–molecule potentials. Here we use the anisotropic H6 (4,3,2) Ar–HF potential [298] and the H6 (4,3,0) Ar–HCl potential [212]. These functions have been determined by fixing the long–range part (dispersion and induction) using known dispersion coefficients and polarizabilities. The short and medium range (minimum energy contour) have been determined by fitting a highly flexible model function to a plethora of infrared and far–infrared spectroscopic data of the Ar–HX complexes [213]. In particular, 22 parameters have been used to fit the H6 (4,3,2) function to the data for HF ($v = 0, 1, 2$) and DF ($v = 0, 1$). The 19 parameters of the H6 (4,3,0) function are fitted to the data for HCl ($v = 0, 1$)and DCl ($v = 0, 1$). Both these potential energy surfaces are given as a function of the distance $|\vec{R}|$ between the atom and the center of mass of the molecule and the orientational angle θ between the molecular axis and the vector $\vec{R}$. Note that these potentials are formulated adiabatically with respect to the HX vibrational coordinate. They parametrically depend on the quantum number v of the vibrational state of the HX molecule, see also our comment in Sec. 3.2.4. Finally, the solute energy $V_{HX(v)}$ is calculated as a vibrational bound state energy of the HCl ground state Morse oscillator with parameters specified in Sec. 2.3.1.

The atom–molecule potentials for Ar–HF and Ar–HCl are illustrated in Fig. 4.1. For the linear Ar–HX arrangement ($\theta = 0$) we find the global potential energy minimum of 220 cm^{-1} or 176 cm^{-1} at an atom molecule separation of $R = 343.4$ pm or 400.4 pm, respectively, for the vibrational ground state ($v = 0$). In addition, there are secondary local minima for the linear Ar–XH geometry ($\theta = \pi$) with a well depth of 107.5 cm^{-1} or 148.3 cm^{-1} at very similar (HF) or at shorter (HCl) separations. Between the two minima there is a saddle with a barrier height of 139.4 cm^{-1} or 71.0 cm^{-1}. We conclude that the angular anisotropy of the interaction with the argon atom is much stronger for HF than for HCl. This tendency further increases when going to higher vibrational states where especially the global Ar–HF minimum is becoming deeper while the secondary minimum remains roughly unchanged. For example, the global minimum of the Ar–HF system for $v = 2$ is found at 259.5 cm^{-1}while the Ar–HCl minimum energy for $v = 2$ is lowered by less than 10 cm^{-1} in comparison with the $v = 0$ state.

4.2.2 Excited State

Due to the absence of sophisticated atom–molecule potential functions, the potential energy surface for the first electronically excited state is constructed

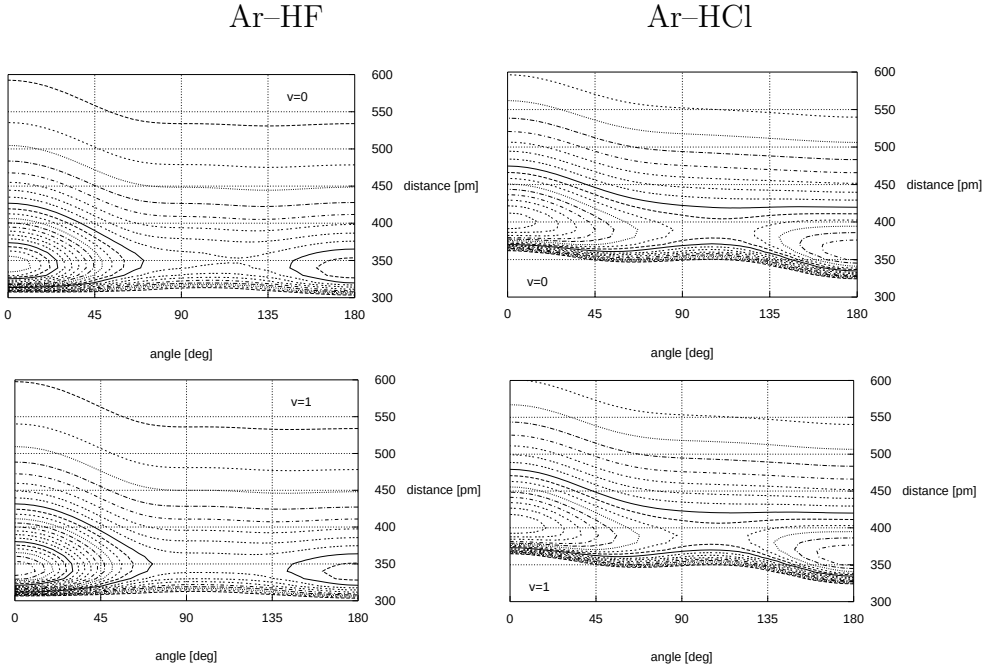

Figure 4.1: Atom–molecule ground state potentials potentials for Ar–HF (left, from Ref. [298]) and Ar–HCl (right, from Ref. [212]). The contour diagrams show the potential energy versus distance R and angle θ for a progression of vibrational states of the HX molecule (top: $v = 0$, bottom: $v = 1$). The contour spacing corresponds to 10 cm^{-1}.

as a sum of pairwise additive atom–atom potentials (see Fig. 4.2)

$$V_e = V_{HX} + \sum_{i=1}^{n} V_{Rg_iH} + \sum_{i=1}^{n} V_{Rg_iX} + \sum_{i<j} V_{Rg_iRg_j} \tag{4.2}$$

where *ab initio* data for the repulsive $^1\Pi$ state of the HF [299] or the HCl [300] guest molecule are adapted from the literature.

The most crucial ingredient when treating the direct cage exit dynamics, however, is the Ar–H interaction. Previous work (see citations in Sec. 4.1) relied either on a potential determined from total scattering cross sections [303] or on a semi–empirical potential [304]. Because these two potentials do not agree very well with each other in the repulsive regime we obtained a new potential energy curve from quantum chemical MP2 calculations the details of which will be published soon [301].

The rare gas–halide interaction potential is derived from differential scattering experiments with magnetically state–selected halide atoms which allow determination of potentials for each J, M_J state and the spin–orbit coupling between them [305]. In the present work we restrict ourselves to the ground state potential ($V_{3/2,1/2}$) of Ar–X thus neglecting the anisotropy of the effective adiabatic potentials and the orbital dynamics of the ^2P state. For Ar–F, the potential curve exhibits a minimum with $\epsilon = 0.84$ kJ/mol and 331 pm [302].

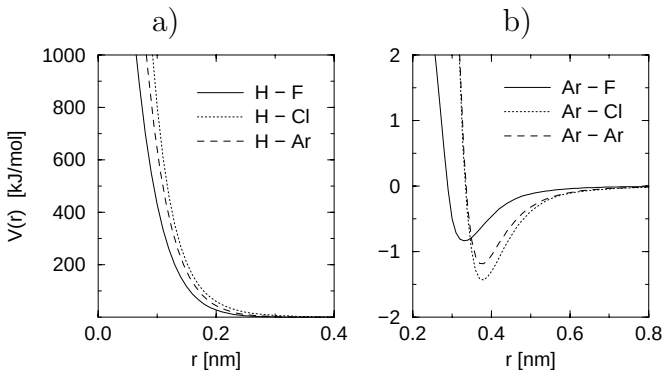

Figure 4.2: Atom–atom excited state potentials for the Ar–HF and the Ar–HCl system. a) Repulsive $^1\Pi$ states of the hydrogen halides together with our MP2 potential for the Ar–H interaction [301]. b) $V_{3/2,1/2}$ potential curves for Ar–F [302] and Ar–Cl [211] and the HFD-B2 model of the Ar–Ar interaction [210]

For Ar–Cl, the $V_{3/2,1/2}$ potential curve of Ref. [211] with $\epsilon = 1.44$ kJ/mol and $r_m = 378$ pm is used, see also Sec. 3.2.4.

This simple *ansatz* of pairwise additive atom–atom potentials can be improved in the framework of the diatomics–in–molecule (DIM) approximation which allows the systematic construction of many–body interactions from potentials for the diatomic fragments. In particular, for the photodissociation of HCl in Ar clusters and matrices, such an approach has already been pursued for the basis of the three p–orbitals of the Cl atom. The potential energy surface was constructed from the $^1\Sigma$, $^1\Pi$, $^3\Sigma$, and $^3\Pi$ potentials of the HCl and from the V_0 and V_2 components of a Legendre expansion of the Cl–Ar interaction. Inclusion of the spin–orbit interaction of the Cl atom and diagonalization finally yields twelve adiabatic surfaces and their respective coupling elements [230, 277, 278]. However, in these studies, the nuclear dynamics was treated semi–classically using a surface–hopping approach [306, 307]. Quantum dynamical investigations of the HX photodissociation in a rare gas environment based on DIM potentials are currently under work in our laboratory [301].

Note that DIM potentials have recently also been used to determine the structure of HF monomers and dimers in Ar clusters in the electronic ground state. Although the details of the atom–molecule interaction do not precisely coincide with the H6 potentials [298, 212] or with the high quality MP4 *ab initio* data [308], they nevertheless allow a quantitative calculation of vibrational frequency shifts if also ionic states are included [309, 310].

4.2.3 Model Systems

In our studies put forward in the following subsections we want to study the gradual transition from gas phase to condensed phase spectroscopy and/or dynamics. Hence, we simulate the shell–wise cluster growth from a first complete solvation shell surrounding the guest molecule up to ten complete shells of

guest atoms. It is well–known from both experiments [218, 219] and theoretical considerations of closest packing [220, 221] that pure (homogeneous) rare gas clusters of a few hundreds of constituents nucleate in an icosahedral symmetry[3] (I_h, see Fig. 4.3(a)). Only after reaching a critical aggregation size which is currently estimated to be in the range of a few thousand particles, bulk effects gain influence over surface effects. A transition to octahedral (O_h) packing occurs and finally the rare gas crystal belongs to the face–centered cubic (fcc) group, see Fig. 4.3(b).

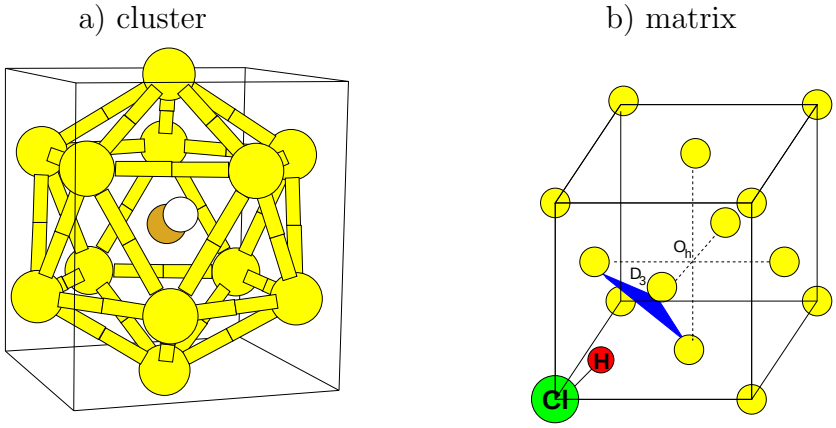

Figure 4.3: Guest–host model systems: HX (X = F, Cl) molecule at a mono–substitutional site of an icosahedral rare gas cluster (a) or an fcc matrix (locally octahedral).

For the systems under investigation here, the comparable van der Waals radii of HF, HCl, and Ar suggest that the guest molecules occupy a single substitutional site in an Ar cluster or matrix. Hence, in our simulations of the shell–wise growth of clusters, we assume a single molecule in the center of a perfectly symmetric icosahedral or octahedral cluster. However, the HF molecule may also occupy a distorted interstitial site which is not considered here [311]. As has already been mentioned in Sec. 3.3.2 for the related $ClAr_{12}$ aggregate, there is a preference for the guest particle to be located at the center of a finite aggregate if (1) guest and host are of similar size, and (2) the guest–host attraction is stronger than the host–host interaction. Based on the atom–molecule potentials mentioned above, this is clearly the case for the Ar–HF system. For the Ar–HCl system, however, the (spherically averaged) attraction is slightly weaker while at the same time the minimum energy contour is found at slightly larger atom–molecule distances than for the Ar–HF system. In total this leads to a slight preference of finding HCl on the outside of an Ar cluster (-4550 cm^{-1}) over the inner site (-4400 cm^{-1}) [312]. However, in the present work, we focus on the latter geometry because (1) the energetic difference of the two structures is relatively small and because (2) we want to be consistent with the Ar–HF system. Furthermore, in modern beam experiments guest–host

[3]Note that ten complete icosahedral shells correspond to approx. 2000 rare gas atoms.

systems can be selectively produced, e. g. using pick–up techniques [313, 314]. Another possibility of forming preferentially the cluster with a guest molecule at its center could be the re–neutralization of a rare gas cluster formed around a negatively charged molecular ion which interacts more strongly with the rare gas atoms due to its higher polarizability [277].

4.3 Method

4.3.1 General Approximations

A full quantum–mechanical treatment of the systems considered here is far beyond the capacity of today's computational means. Even the smallest system to be investigated here, i. e. a hydrogen halide molecule with the first complete solvation shell comprising of 12 atoms, has 39 nuclear degrees of freedom which cannot be treated exactly. Hence, for our treatment of the stationary ground state wavefunctions and the excited state quantum dynamics (see the following two subsections) we have to rely on two basic assumptions.

1. In most of the work presented here, the rare gas atoms in the cluster or the matrix are assumed to be frozen, i. e. we neglect the dynamics of the Ar cluster vibrations or the Ar matrix phonons, respectively. This is essentially equivalent to treating the system like a dimer consisting of a frozen Ar subunit on the one hand and a diatomic molecule with its six degrees of freedom on the other hand [315]. The validity of this approximation depends strongly on the details of the system under investigation as well as on the observables considered. For a discussion, see our remarks in 4.6.4 where we also present results of calculations for a flexible cage using the quantum–classical molecular dynamics (QCMD) approximation proposed in Sec. 4.3.4. An outlook towards a fully quantum–mechanical treatment based on the CSP approximation of the photodissociation dynamics is given in Sec. 4.6.6.

2. The position of the center of mass of the diatomic guest molecule is fixed at a substitutional site of the rare gas cluster or matrix, i. e. we neglect any effects of rotation–translation coupling (RTC) [316, 317]. Of course this approximation is limited to the case of relatively small diatomic hydride molecules which fit well into a mono–substitutional site and are close to the limit of a free rotor. A discussion of the validity of this approximation can be found in Sec. 4.4.3.

4.3.2 Ground State Wavefunctions

Within the framework of the two approximations given above, the problem of finding ground state energies and wavefunctions reduces to solving a three–dimensional time–independent Schrödinger's equation for the relative motion of the diatomic molecule in the field of the surrounding rare gas atoms. In a

position space representation using spherical coordinates r, Θ, Φ we obtain

$$\left[-\frac{\hbar^2}{2m}\frac{\partial^2}{\partial r^2} + \frac{\hat{J}^2(\Theta,\Phi)}{2mr^2} + V_g(r,\Theta,\Phi)\right]\psi_g(r,\Theta,\Phi) = E_g\psi_g(r,\Theta,\Phi) \qquad (4.3)$$

where the first two terms represent the radial and angular part of the kinetic energy of the H–atom, respectively, with m standing for the reduced mass of the diatomic and V_g describes the potential energy surface for the ground electronic state. This equation is the time–independent analogue to Eq. (2.9) on page 16 but for vanishing external field. Note that here the potential depends on all three degrees of freedom. As a further approximation let us assume that the vibrational coordinate r can be separated from the angular degrees of freedom and that the eigenvalues $E_{g,v,i}$ represent the i–th rotational eigenenergy for a given vibrational state v of the molecule in the ground electronic state. This is justified by the large discrepancy of vibrational and rotational time/energy scales for this class of molecules. Finally, the angular dependence of the wavefunctions ψ_g is expressed in a basis of spherical harmonics

$$\psi_{g,v,i}(r,\Theta,\Phi) = \frac{\phi_{g,v}(r)}{r}\sum_{J=0}^{\infty}\sum_{M=-J}^{J} c_{g,v,i,JM}\, Y_{JM}(\Theta,\Phi) \qquad (4.4)$$

where the coefficients $c_{g,v,i,JM}$ are eigenvectors corresponding to the eigenvalues $E_{g,v,i}$ of the secular equation

$$\left|H_{g,v,JMJ'M'} - E_{g,v,i}\right| = 0 \quad . \qquad (4.5)$$

The matrix elements of the rotational Hamiltonian are given by

$$\begin{aligned} H_{g,v,JM,J'M'} &= B\,J\,(J+1)\,\delta_{JJ'}\,\delta_{MM'} \\ &+ \int d\Omega\, Y^*_{JM}(\Theta,\Phi)\,\bar{V}_{g,v}(\Theta,\Phi)\,Y_{JM}(\Theta,\Phi) \end{aligned} \qquad (4.6)$$

with $B = \hbar^2/(2mr_v^2)$ being the rotational constant for the vibrationally averaged bond length r_v. The vibrationally adiabatic potential energy function is defined as an average over a vibrational wavefunction $\phi_{g,v}(r)$ of the ground state HX molecule

$$\bar{V}_{g,v}(\Theta,\Phi) = \int dr|\phi_{g,v}(r)|^2 V_g(r,\Theta,\Phi) \quad . \qquad (4.7)$$

Note that these integrals do not have to be evaluated explicitly and that Eq. (4.1) can be directly inserted for $\bar{V}$ into Eq. (4.6) because the atom–molecule potentials of Refs. [298, 212] are already defined in a vibrationally adiabatic formulation.

4.3.3 Excited State Dynamics

The photodissociation dynamics is assumed to be initialized by instantaneous excitation of the hydrogen halide from its $^1\Sigma$ ground electronic state to the repulsive $^1\Pi$ state, i. e. by an ultrashort light pulse which is close to the limit

of a δ pulse. In order to describe the wavepacket evolution on the corresponding potential energy surface, we have to solve a three–dimensional time–dependent Schrödinger's equation for the relative motion of the hydrogen and the halide atom

$$i\,\hbar\,\frac{\partial}{\partial t}\,\psi_e(r,\Theta,\Phi;t) = \left[-\frac{\hbar^2}{2m}\frac{\partial^2}{\partial r^2} + \frac{\hat{J}^2(\Theta,\Phi)}{2mr^2} + V_e(r,\Theta,\Phi)\right]\psi_e(r,\Theta,\Phi;t) \quad . \tag{4.8}$$

Here V_e stands for the excited state potential energy surface of Eq. (4.2). Again it is noted that this equation is analogous to Eq. (2.9) for the photoassociation-dynamics but without coupling to a time–dependent external field. The above equation has to be solved subject to an initial condition ($t = 0$) of the form (4.4). In particular, this allows to investigate the dependence of the photodissociation dynamics on the initial ro–vibrational state of the diatomic molecule, see Sec.4.6.

In analogy to the "close–coupled wavepacket" (CCWP) method commonly used in diatom–surface scattering theory [318,319], the angular part of the 3–D wavefunction is expanded in terms of spherical harmonics using the *ansatz*

$$\psi_e(r,\Theta,\Phi;t) = \sum_{J=0}^{\infty}\sum_{M=-J}^{J}\frac{\phi_{eJM}(r,t)}{r}\,Y_{JM}(\Theta,\Phi) \tag{4.9}$$

where the time–dependence of the wavefunction is cast into the radial functions $\phi_{e,JM}(r,t)$, see also Eq. (2.10) in the chapter on photoassociation. Inserting Eq. (4.9) into the time–dependent Schrödinger's equation (4.8) and projection on one of the angular functions yields the following set of coupled equations for the radial wavefunctions

$$\begin{aligned} i\,\hbar\,\frac{\partial}{\partial t}\,\phi_{eJM}(r,t) &= \left[-\frac{\hbar^2}{2m}\frac{\partial^2}{\partial r^2} + \frac{J(J+1)\hbar^2}{2mr^2}\right]\phi_{eJM}(r,t) \\ &+ \sum_{J'M'} V_{e,JMJ'M'}(r)\,\phi_{eJ'M'}(r,t) \end{aligned} \tag{4.10}$$

where the matrix elements of the potential energy are defined as the integrals over the surface of the unit sphere

$$V_{e,JMJ'M'}(r) = \int d\Omega\, Z_{JM}(\Theta,\Phi)\, V_e(r,\Theta,\Phi)\, Z_{J'M'}(\Theta,\Phi) \tag{4.11}$$

These effective potentials are most practically calculated by first expanding V_e for each value of the radial coordinate in spherical harmonics and then employing the spherical harmonics addition theorem in order to calculate integrals over products of three spherical harmonics from Clebsch–Gordon coefficients [320, 321, 322] [4]. The expansion coefficients of the potential function in spherical harmonics are obtained by a direct product scheme using Gauss–Legendre integration in $\cos\Theta$ and Φ. Typically, 100×200 integration points are employed for $J \leq 25$.

[4] Note that the numerical advantage stems from the fact that the Clebsch–Gordon coefficients have to be calculated only once and can be tabulated for later use.

The coupled equations (4.10) are solved numerically using a Fourier collocation scheme for discretization of the radial coordinate r [31, 34]. The grid consists of 1024 equidistant points in the range 0 to 4 nm. To avoid unphysical reflection from the edge of the grid, a negative imaginary potential is used in the range beyond 3 nm [323]. It is noted that the relatively small distance of the grid points is caused by the high excitation energy of the $^1\Pi$ state in the order of a few hundred kJ/mol.

In contrast to our numerical solution of the coupled equations for the photoassociation induced by time–dependent fields in Sec. 2.2.4 using a split–operator scheme, the dynamics is governed here by a time–independent Hamiltonian. Hence we can make use of a global propagation scheme permitting long time steps. In the present work, the exponential in the time evolution operator is approximated by expansion in a series of (complex) Chebychev polynomials. Apart from the uniform distribution of the error, this expansion offers the advantage of an exponential fall–off of the expansion coefficients beyond a certain expansion order [324, 31, 32, 34, 325]. For the problem investigated here we are typically using 100 polynomials permitting a time step of 5 fs.

4.3.4 Quantum–Classical Molecular Dynamics (QCMD)

After having outlined a three–dimensional fully quantum–mechanical treatment of the relativ motion of the diatomic molecule (which is essentially identical to the motion of the hydrogen atom) in a frozen rare gas environment, we want to come back to the question of the full dynamics of the system. Owing to the separation of the mass scales, we want to introduce here a quantum–classical molecular dynamics (QCMD) model. Such an approach has been first introduced into the field of chemical physics in the early 1980s [326, 327]. Since then this technique has been applied to numerous problems such as proton transfer [328, 329, 330, 331, 332], absorption spectroscopy of particles trapped in zeolites [333], and reaction dynamics [334, 335]. In the last few years years, there are also a few articles dealing with the rigorous mathematical justification and the approximation properties of the QCMD model [336, 337, 338, 339, 340].

The basic idea is to divide the complete system into one sub–system with (typically few) degrees of freedom $\vec{r}$ which are treated quantum–mechanically while treating the remaining sub–systems with its (typically many) degrees of freedom $\vec{R}$ classically. Here the separation of the mass scales naturally suggests a quantum mechanical treatment of the hydrogen atom dynamics using the CCWP formalism in the basis of spherical harmonics introduced above, and a classical treatment of the halide and the rare gas atoms. The quantum–mechanical and the classical sub–system are coupled self–consistently through effective time–dependent potentials. The time–dependence of the potential governing the H atom dynamics is obtained by inserting the trajectories of the heavy atoms into the full potential function $V(\vec{r}, \vec{R})$. The forces acting on the heavy atoms are taken as the derivatives of an effective potential which is the expectation value of the total potential energy function $V(\vec{r}, \vec{R})$ with respect to

the wavefunction of the light particle

$$\begin{aligned} F_{\rm class}(\vec{R},t) &= -<\psi(\vec{r},t)\left|\frac{d}{d\vec{R}}V(\vec{r},\vec{R})\right|\psi(\vec{r},t)> \\ &= -\int d\vec{r}\left|\sum_{JM}\phi_{eJM}(r,t)\,Y_{JM}(\Theta,\Phi)\right|^2\frac{d}{d\vec{R}}V(r,\Theta,\Phi;\vec{R}) \quad . \end{aligned}$$

A variety of practical algorithms to solve the coupled quantum–mechanical and classical equations of motion has been developed recently. Based on the canonical structure of the QCMD model, a sympletictic integrator called PICK-ABACK has been developed which basically consists of a suitable indention of a classical "leap frog" and a quantum–mechanical "split operator" scheme [341]. In model calculations for the photodissociation of a colinear Ar$\cdots$HCl cluster, we have demonstrated the accuracy and stability of this discretization scheme. This algorithm has also been used for the simulations presented in Sec. 4.6.4. In more recent work other schemes permitting the use of different time steps for the integration of the quantum–mechanical and the classical parts have been developed [342, 341, 343].

4.3.5 Symmetry Adapted Spherical Harmonics (SASHs)

When performing the calulations of ground state wavefunctions or excited state wavepacket dynamics as explained in the previous two subsections, the effort to solve the coupled time–independent equations (4.5) or the time–dependent equations (4.10), depends crucially on the number of rotational basis functions involved. It is obvious that both the computational effort and the memory requirement depend quadratically on the number of rotational basis functions in our *ansatz*. In this section we will demonstrate how the high symmetry of the problem under consideration can be exploitet to substantially reduce this number by using linear combinations of spherical harmonics which are symmetry adapted. Note that these symmetry adapted spherical harmonics (SASHs) are also known as surface harmonics or lattice harmonics [344].

The technique of forming symmetry adapted linear combinations of any kind of basis functions by use of projectors is well–known [345, 346]. When dealing with spherical harmonics, however, the evaluation of the projectors becomes more difficult because it requires a complete map of the basis functions under the influence of each of the symmetry operations comprising the point group. While this is normally straight–forward for vibrational or electronic basis functions in molecular physics, this is not obvious for spherical harmonics of all but the very lowest order. The mapping of spherical harmonics under a symmetry operation is described by Wigner's law [320, 321]. The direct numerical implementation, however, poses severe numerical problems. A recursive formula to circumvent these problems is given in Ref. [344]. That work also contains tables of SASHs of the O_h point group but only up to $J \leq 12$. The icosahedral point group I_h, however, has been long neglected due to its irrelevance for crystallography. Early exceptions are the works by Cohan [347] and by McLellan [348]. Stimulated by a renewed interest in this symmetry in the 1990s, SASHs have

been calculated in a number of more recent publications [349, 350, 351, 352]. However, the results of all of these studies are either restriced to relatively low values of $J \leq 12$, or they are restriced to the totally symmetric irreducible representation A_g only. For the present work SASHs had to be calculated for many irreducible representations of both the O_h and the I_h point group, see the Appendix of C.2.

4.4 Vibrational Energy Shifts

4.4.1 Solvent Structure

It is well known that the vibrational frequency shifts of molecules in a solvent environment depend sensitively on the exact geometry of the solvent, see for example the study of the isomer dependence of $HFAr_n$ ($n = 1 - 14$) [353]. The icosahedral and octahedral clusters with closed solvation shells are much more rigid due to the close packing than the smallest clusters with a few solvent atoms which undergo large–amplitude–motions [55]. Anticipating one of the results of Sec. 4.5, i. e. that the rotational ground state wavefunction is very close to an isotropic distribution, the only solvent degree of freedom governing the vibrational frequency shift here is the size of solvation cage. In other words, in the optimizations we are employing a spherically averaged atom–molecule potential. Hence we are minimizing the potential energy of the complete system as defined in Eq. (4.1) with respect to the distance between the guest molecule and its nearest, second–nearest, etc. neighbour rare gas atoms while conserving the I_h or O_h symmetry.

The qualitative result of such a minimization can already be guessed from the contour plots of Fig. 4.1. Depending on whether the minimum energy contour is found at smaller (HF) or at larger (HCl) distances than the nearest neighbour distance of a pure Ar crystal of 376 pm [354], the atom–molecule interactions have the tendency to shrink or to expand the cage, respectively. In competition with the Ar–Ar interactions, this leads to small ($< 0.5\%$) but significant changes of the cage radii (for details, see C.1). Despite of the identical number of twelve nearest neighbour atoms, these changes are different for the icosahedral and the octahedral symmetry because of the different number and distances of Ar–Ar pair interactions.

4.4.2 Results

Once the cluster geometry has been determined, the time–independent Schrödinger's equation (4.5) has to be solved assuming the guest molecule with its center of mass at a substitutional site in a frozen rare gas environment. Then it is straightforward to calculate vibrational frequency shifts from the differences of ro–vibrational energy levels

$$\Delta_{v \to v+1} = E_{g,v+1,0} - E_{g,v,0} \tag{4.12}$$

where the difference is taken between different vibrational states but for identical rotational states (here: ground state, $i = 0$). Our results for the fundamental

transition $v = 0 \rightarrow 1$ are depicted in Fig. 4.4. Our findings are summarized as follows:

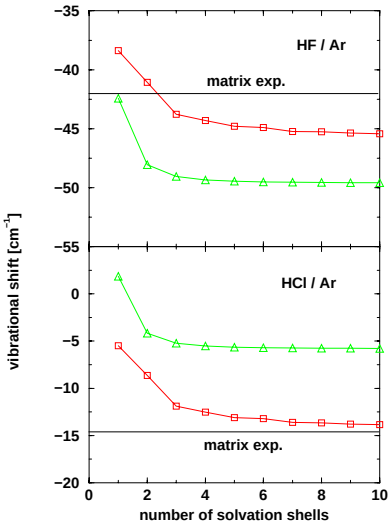

Figure 4.4: Vibrational frequency shift for the fundamental excitation of HX (X = F, Cl) in an argon environment versus number of solvation shells. Squares: Octahedral solvation. Triangles: Icosahedral solvation. The horizontal lines indicate the experimental shift in an fcc matrix. From C.1

1. In general the lowering of the excitation frequency ("red shift") is much larger for HF than for HCl. This is because of the stronger polarity and polarizability of the HF molecule which increases much more strongly with v than for HCl.

2. The frequency shifts for icosahedral and octahedral environment are distinctly different. This difference is correlated with the radius of the solvation shell formed by the nearest neighbours. For example, the very small red shift (or even blue shift) of HCl in Ar(I_h) compared with Ar(O_h) is caused by the insufficient cage expansion for the former case. In any case it is important to note that the exact solvent geometry is crucial for the frequency shifts and that simulations for an unrelaxed solvent can lead to completely different results. For more details, see C.1.

3. The most exciting aspect of our results, however, is the dependence of the frequency shift on the number of solvation shells. Unlike stated in the literature [355], the frequency shift is by no means converged after the completion of the first solvation shell. This is because the decreasing contribution of particles in the outer shell atoms is partly compensated by the larger number of atoms. Due to the different radii of the shells and due the different number of rare gas atoms per shell, a different number of solvation shells is needed to obtain converged results. For the icosahedral cluster, it takes about three shells to reach convergence within

1 cm^{-1} while for the octahedral cluster growth five shells are needed. In principle, the latter values should be expected to converge towards the experimental matrix shift. In agreement with earlier work [311], we reach very good agreement with the measurements of Refs. [356, 357, 358, 311] for HF. Note that also the frequency shift for the icosahedral $HFAr_{12}$ is close to the matrix value which we regard, in contrast to the assessment of Refs. [359, 360, 361, 315] as a mere fortuitousness. For HCl, where matrix shifts have been calculated for the first time, the values of Refs. [362,363,364,365] could only be reproduced qualitatively. Here the exact value of the cage expansion has proved crucial in calculating the frequency shift. Hence, it might be very promising to explore the effect of three–body forces on this shift.

4.4.3 Discussion

Finally, we want to comment on the importance of quantum effects. In the work presented above, vibrational frequency shifts have been determined for an isotropic rotational ground state wavefunction while freezing both the center of mass motion of the diatomic molecule and the motion of the rare gas atoms completely. It is interesting to compare our results with those of Refs. [359, 360, 361, 315, 353] on $HFAr_n$ ($n = 1 \ldots 14$) where also the three degrees of freedom of molecular translation have been incorporated in 5–dimensional quantum calculations. For the icosahedral $HFAr_{12}$ our result is exactly identical with their finding of -42.46 cm^{-1}. This indicates that our simplified model is justified for close solvation shells. This is, however not the case for smaller clusters where large–amplitude motions govern the dynamics. For the cluster sizes $n = 1 \ldots 4$ classical calculations (i. e. completely neglecting quantum effects) overestimate the redshift by a factor of two, see e. g. the comparison in Fig. 3 of Ref. [312]. It has recently been shown that this discrepency is reduced in the picture of the above 2–D quantum calculations using Eq. (4.5) [366]. Hence, the remaining discrepancy is essentially traced back to the translational motion of the molecule.

An even more rigorous approach is to calculate the wavefunctions of the system in full dimensionality. At present, there are two classes of computational methods to perform such calculations. Using *Monte Carlo* techniques, energies and wavefunctions could be obtained for $HFAr_n$ ($n = 1 \ldots 4$) clusters [294,367]. Although the contribution of the solvent degrees of freedom to the HF vibrational frequency shift is marginal, these calculations provide full wavefunctions. Also vibrational self–consistent–field techniques [368, 369] have been used for cluster bound state calculations, see e. g. the recent work on Ar_{13} [370]. Alternatively, also path integral techniques can be applied, see e. g. Ref. [371] on icosahedral rare gas aggregates.

4.5 Rotational Energy Shifts and Wavefunctions

4.5.1 Introduction

In order to motivate the studies of rotational wavefunctions of hydrogen halide molecules in rare gas clusters and matrices, we want to give emphasis to their role as initial states for a photodissociation events, see the following Sec. 4.6. To get a first impression, let us consider purely classical simulations of the photodissociation of HCl in an Ar (fcc) matrix [372]. The photodissociation is modeled here by simply switching the interactions from the ground electronic state (4.1) to the electronically excited state (4.2) and, subsequently, integrating the resulting equations of motion for all participating atoms using Gear's predictor–corrector scheme [206] and assuming periodic boundary conditions [207].

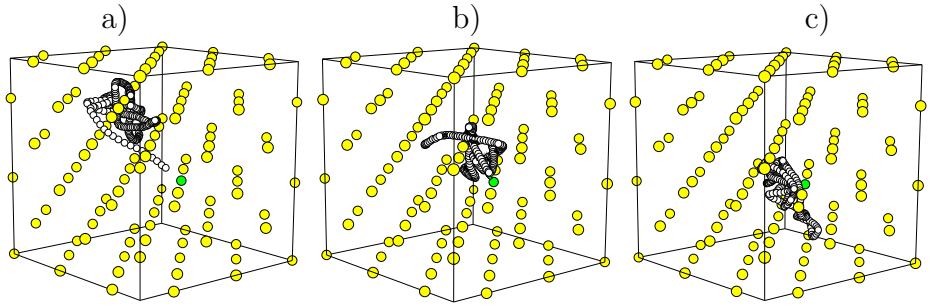

Figure 4.5: Classical trajectories for HCl photodissociation in an argon matrix. a) Immediate cage exit, b) delayed cage exit, and c) trapping of the photodissociated hydrogen photofragment. Note that only the trajectory of the H atom is represented because the vibrational amplitudes of the heavy atoms are very small. From [372].

The trajectories in Fig. 4.5 illustrate the strong dependence of the reaction dynamics on the initial orientation of the molecule: In case of a favorable orientation close to the $< 111 >$ direction we observe a immediate cage exit during which the hydrogen atom can penetrate two of the closest packed (111) planes, see part (a) of the figure. However, if the initial orientation is less favorable, the hydrogen atom rattles forth and back inside a cage formed by the adjacent (111) planes. In the course of this oscillatory motion, it gradually looses some of its excess energy during the collisions with the heavier atoms and either one of two events can occur: As long as the energy is still sufficient to overcome one of the barriers along the $< 111 >$ axes, the hydrogen atom still has some chance for a delayed cage exit process, see part (b) of the figure. Once the energy has dropped below a certain threshold, this channel is closed and the H atom becomes trapped and will eventually recombine with the Cl atom.

These exemplary trajectory studies are intended to elucidate the influence of the initial orientation of the guest molecule on the photodissociation dynamics. According to the quantum–classical correspondence principle, the distribu-

tion of orientations corresponds to the square of the rotational wavefunctions. Hence, it is important to calculate exact rotational wavefunctions as initial states for simulations of the photodissociation dynamics [5].

4.5.2 Potential Energy Surfaces

In this section, we want to present the potential functions for molecular rotation inside a cluster or a matrix and discuss the rotational energies and wavefunctions obtained. Let us first consider the case of a molecule located at the center of an icosahedral (I_h) $HXAr_{12}$ cluster.The potential functions for rotation of the hydrogen halide molecule in the cluster is illustrated in Fig. 4.6 (a,b). For HF we find an almost flat potential energy surface with undulations of less than 3 cm^{-1}. Apparently the strong anisotropy of the individual atom–molecule potentials of more than 100 cm^{-1} averages out almost completely. In contrast, the potential for HCl exhibits sharp peaks corresponding to the orientations of the surrounding Ar atoms which are caused by the repulsive part of the H6 potential for an optimized atom–molecule distance of 376.6 pm.

A different situation is found for the rare gas matrix with locally octahedral symmetry (O_h), see Fig. 4.6 (c,d). For both HF and HCl, there are eight minima at the crystallografic $< 111 >$ directions indicating the energetically preferred orientations of the molecule in the solid. Note that this is in agreement with the C_{3v} structure of $HXAr_3$ clusters. Interestingly, the main repulsive orientations are qualitatively different. For HF we find six maxima corresponding to the $< 100 >$ orientations whereas in the case of HCl, twelve maxima can be found at the $< 110 >$ directions pointing towards the nearest neighbour atoms. While the energy maximum for HF is simply caused by less attractive interactions for this particular orientation, the maxima in the potential for HCl in Ar can be rationalized as mentioned above, i. e. the confinement in the cage leads to repulsion by the nearest neighbour atoms. The difference between the potential minima and maxima for either of the systems is around 30 cm^{-1}. It is noted that this anisotropy is much smaller than that of the atom–molecule pair potentials of Fig. 4.1, see also our remarks below (Sec. 4.5.5). Furthermore, it is found that more than 90% of the anisotropy of the matrix potential is caused by the interaction with the nearest neighbour atoms only.

A simple way to classify the qualitative difference of the two rotational potential energy surfaces is to expand them in symmetry adapted linear combinations of spherical harmonics (SASHs) [373]. For the point group O_h, the lowest functions which transform according to the totally symmetric representation A_{1g} (except for a constant term $J = 0$) are those for $J = 4$ and for $J = 6$ [344]. It turns out that the potential function for rotation of HF in Ar is dominated by the $J = 4$ term while that for HCl most closely resembles that for a $J = 6$ function. Thus the Devonshire model as early as in the 1930s [374] which allows predictions of splittings of rotational lines for the case of a pure $J = 4$ potential can reproduce the HF case very well while it has to fail for

[5] Note that also the debate in the literature on the existence of resonances in the photodissociation spectrum of HClAr is most likely to be caused by different initial bending states of the H atom [265, 266, 268, 269, 270]

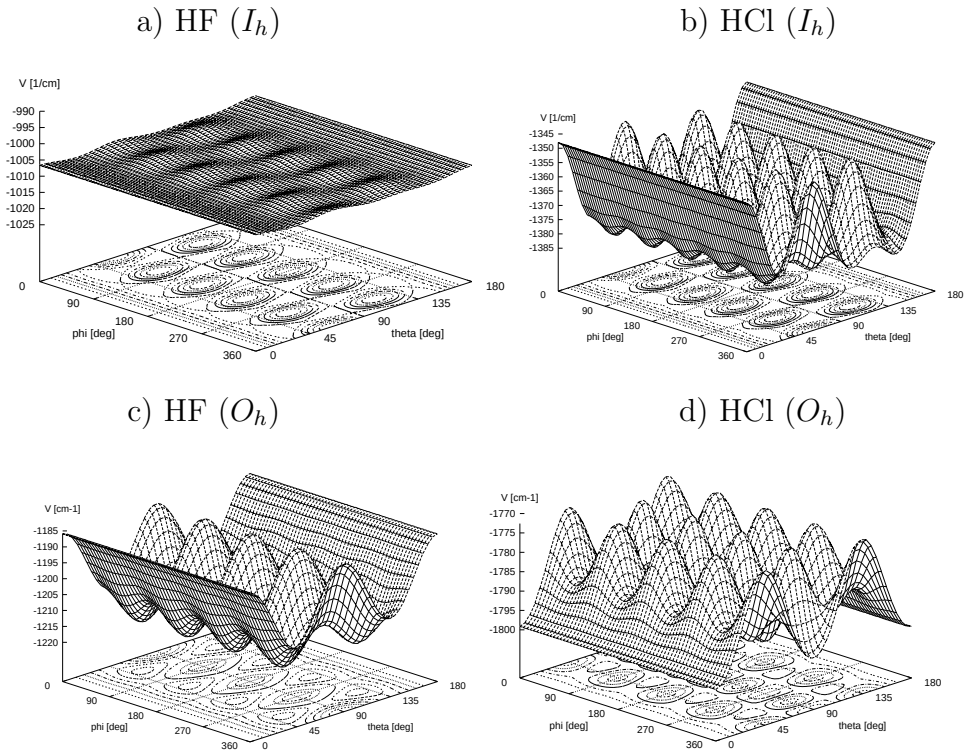

Figure 4.6: Potential energy surface for rotation of an HF (a) or HCl (b) molecule in an icosahedral $HXAr_{12}$ cluster and for rotation of HF(c) or HCl(d) at a substitutional site of an Ar (fcc) matrix. The plot shows the electronic ground state interaction energy between the guest molecule and the Ar solvent as a function of the spherical coordinates Θ, Φ defined with respect to one of the C_5 (I_h) or C_4 (O_h) axes.

HCl. However, for this case predicted splittings and rotational spectra can be found in the work of Beyeler who developed an extended model including both $J = 4$ and $J = 6$ terms and smooth transitions between the two cases [373].

4.5.3 Energy Levels

Our results for the rotational energy levels are summarized in Tab. 4.1 up to $J = 3$. At a first glance, the energy levels are relatively close to those of a free molecule, i. e. $E_J = BJ(J + 1)$ with a rotational constant of 20.2 cm^{-1} or 10.3 cm^{-1} for HF or HCl, respectively, which is a consequence of the relatively weak perturbation of the rotor states by the rare gas environment. A closer look, however, reveals the influence of the surrounding cluster or matrix. In particular, we find that the $(J + 1)$–fold degeneracy of the rotational energy levels is partially lifted. Using group theoretical arguments analogously to those common in crystal field theory [345, 346], it can be shown that these splittings occur only for $J \geq 3(I_h)$ or $J \geq 2(O_h)$.

For the icosahedral clusters the splitting of the $J = 3$ level of HF is extremely

J	I_h			O_h		
	Symm.	HF	HCl	Symm.	HF	HCl
0	A_g	0.0	0.0	A_{1g}	0.0	0.0
1	T_{1u}	40.3	20.6	T_{1u}	40.3	20.6
2	H_g	120.9	61.6	E_g	126.2	59.6
				T_{2g}	117.5	63.1
3	T_{2u}	242.1	128.6	A_{2u}	235.0	122.2
	G_u	241.6	119.7	T_{1u}	245.3	120.6
				T_{2u}	241.0	126.8

Table 4.1: Rotational energy levels (in cm^{-1}) of HF ($v = 0$) and HCl ($v = 0$) in icosahedral clusters with 12 Ar atoms (I_h) and in fcc Ar matrices (O_h).

small because of the near–isotropic potential energy surface. In contrast, for HCl there is a large splitting of about one rotational constant between the T_{2u} and the G_u state. Similarly, splittings in the order of one half of a rotational constant are found for the E_g/T_{2g} splitting of the $J = 2$ levels and the $A_{2u}/T_{1u}/T_{2u}$ splitting of the $J = 3$ levels of HF and HCl in Ar (fcc) matrices. Hence, in an experiment these states should be distinguishable without extremely high effort.

Unlike the situation for the smallest clusters with one or two Ar atoms, experimental data on rotational spectroscopy is not available for the icosahedral clusters. Also for matrix isolated species data for $J > 1$ is extremely sparse. To the best of our knowledge, the only observation of the E_g/T_{2g} splitting is in Ref. [375] for DCl in Ar which is in reasonable agreement with our calculations (2.6 cm^{-1} vs. 3.3 cm^{-1})[6].

4.5.4 Wave Functions

In this part we discuss the nature of the rotational eigenstates. First of all, one notices that the eigenvectors of the Hamiltonian matrix 4.6 defined on page 85 are very close to unit vectors, i. e. the eigenfunctions are very close to single symmetry adapted spherical harmonic (SASH) basis functions. [7] Typically the admixture of further SASHs is well below 1% which is consistent with our results on the energetic levels also suggesting only a minor perturbation of the free rotor states. Hence, the main influence of the rare gas environment is that it forces its symmetry upon the rotational eigenfunctions.

Now let us consider the rotational ground states of cluster or matrix isolated HF or HCl. In each of the cases considered here, the contribution of the isotropic $J = 0$ (A_g or A_{1g}) to the ground state is $\gg 99\%$. This result seems to be in contradiction with the rotational potential energy surfaces of Fig. 4.6 exhibiting barriers of 1.5 (HF) or even (HCl) three times the rotational constant. However,

[6]Note that it would be very desirable to check our predicition of the reversed energetic order of the E_g and T_{2g} energy levels for HF.

[7]Note that this enables us to label the rotational states with a quantum number J and an irreducible representation of the respective point group.

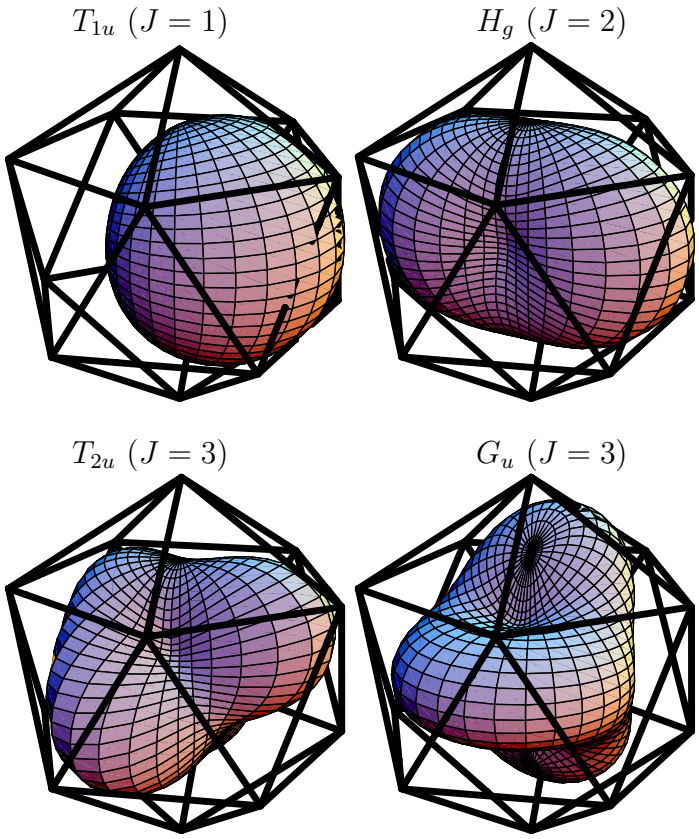

Figure 4.7: Rotationally excited states of HF/HCl in an icosahedral $HFAr_{12}$ cluster. The polar diagrams show the wavefunction superimposed on a sphere. An increase or a decrease of the radius corresponds to a positive or a negative value of the wavefunction. The neighbouring Ar atoms are located at the corners of the circumscribed icosahedra. From C.2

a rotational state with maxima of the probability amplitude located at the minima of the potential energy surface would have to be comprised of higher SASHs of the totally symmetric irreducible representation. For example, for HF or HCl in an Ar matrix, the second ($J = 4$) or even the third ($J = 6$) basis function would be required to fit the minima of the PES. The corresponding high kinetic energy $BJ(J + 1)$ keeps the contribution of these functions to the rotational ground state extremely low.

Graphical representations of the first few rotationally excited eigenstates can be found in the polar representations of Fig. 4.7 for the case of icosahedral symmetry. The first two excited states T_{1u} $(J = 1)$ and H_g $(J = 2)$ are preferentially oriented along a C_3 axis through the centers of an opposing pair of triangles. The same is true for one of the two $J = 3$ states (G_u) while the other one (T_{2u}) is oriented along a C_5 axis pointing towards the corners of the icosahedron.

The situation for the octahdral symmetry is depicted Fig. 4.8. The first rotationally excited state T_{1u} $(J = 1)$ as well as one of the $J = 2$ states (E_g)

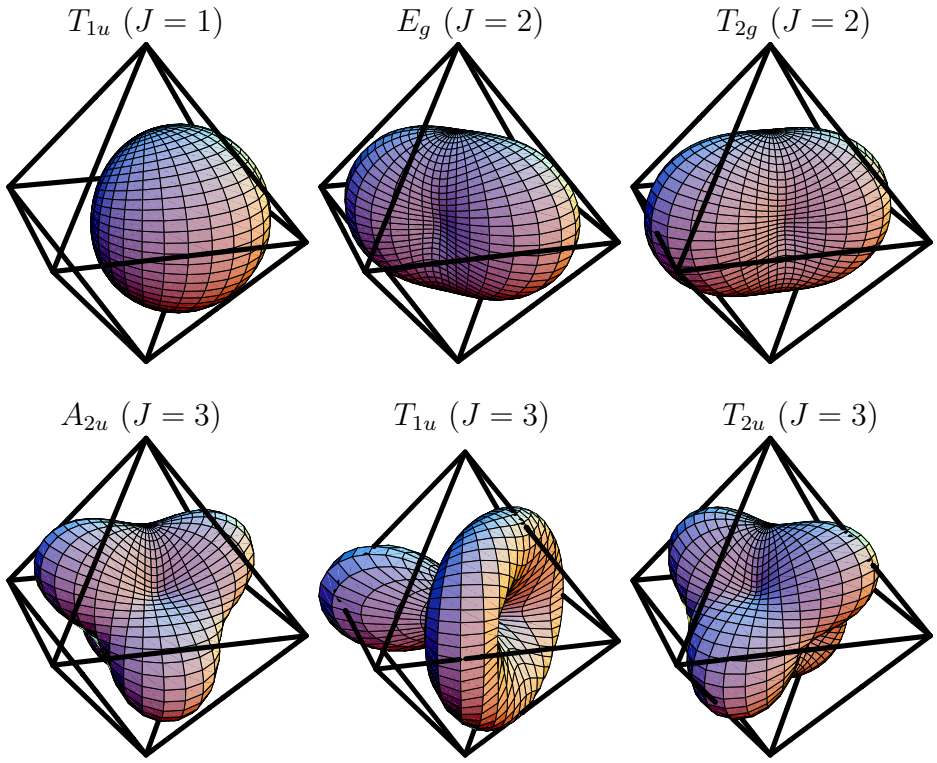

Figure 4.8: Rotationally excited states of HF/HCl in an octahedral Ar matrix. The polar diagrams show the wavefunction superimposed on a sphere. The neighbouring Ar atoms are located at the centers of the edges of the circumscribed octahedra. From C.3

are oriented along the crystallographic $< 100 >$ axes thus pointing towards the second–nearest neighbours. In contrast, the T_{2g} $(J = 2)$ and the T_{2u} $(J = 3)$ states exhibit preferential orientation towards the nearest neighbour positions which are along the $< 110 >$ axes in an fcc lattice. A special case is the A_{2u} $(J = 3)$ state with its $< 111 >$ orientation corresponding to the preferred cage exit pathway [226] of the classical simulations presented in Sec. 4.5.1 above.

4.5.5 Discussion

In the follwing we want to compare our results with the rotational spectroscopy of smaller $HXAr_n$ $(n = 1, 2, \ldots)$ aggregates. In the paragraphs above, we have stressed the fact that both HF and HCl are essentially behaving like free rotors in a closed shell Ar cluster or in an Ar matrix. The only effects of the rare gas surrounding the guest molecule are (1) the small (but detectable) splittings of the rotational energy levels and (2) the mixing of different M sublevels resulting in rotational wavefunctions which are adapted to the symmetry of the solvent. The situation for smaller aggregates with an incompletely filled solvation shell, however, is qualitatively different. As can be guessed from the PESs for the systems with a single Ar atom, the lowest eigenfunctions do not permit free

rotation but are rather characterized by large amplitude hydrogenic bending motions and terms like hindered rotation or libration are often used in this context. For example, neglecting the Ar stretching modes, the two lowest librational states of the $n = 1$ aggregate correspond to an HF–Ar (ground state) or on Ar–HF (Σ bend) structure. Despite considerable delocalization of the hydrogen atom, the rotation is still hindered. The next state (Π bend) , however, allows rotation of the HF molecule with respect to the Ar atom. When going to slightly larger systems ($n = 2 \ldots 4$) the number of bound states which are quasi–free rotors increases [366]. In summary, the transition from librational motion to quasi–free rotations can be seen as the limit (1) of higher internal excitation and/or (2) of closing the first solvation shell.

4.6 Photodissociation Dynamics

4.6.1 Hydrogen Wavepacket Dynamics

Rotational Ground State In this paragraph we consider the photodissociation for the example of HCl molecules in an Ar(fcc) matrix. The initial rovibrational state of the molecule is assumed to be a direct product of a Morse oscillator ground state function and a rotational ground state $J = 0$ (A_{1g}) function. Upon excitation of the HCl molecule from the bound $^1\Sigma$ to the purely repulsive $^1\Sigma$ state (Condon approximation), the hydrogen photofragment recoils from the much heavier chlorine and starts to interact with the rare gas matrix. The quantum dynamics of this process is illustrated in Fig. 4.9. We are recalling that three–dimensional wavefunctions are represented in the "close coupled wavepacket" (CCWP) approach of Sec. 4.3.3 as a product of symmetry adapted spherical harmonics (SASHs) transforming according to a given irreducible representation of the O_h point group and time–dependent radial wavefunctions. In this and in the following figures, corresponding angular and radial wavefunctions are arranged column–wise.

Initially all the probability amplitude is in the $J = 0$ state at an internuclear distance of $r = 0.127$ nm. The corresponding (radial) wavepacket is moving away from the Cl atom and reaches the repulsive regime of the nearest neighbour atoms. A bifurcation takes place in which a part of the wavepacket is reflected inwards while another part of the wavepacket penetrates the cage formed by the nearest neighbour. The former part oscillates within the cage loosing some amplitude due to cage exit each time it reaches the outer turning point. The vibrational period of about 15 fs corresponds to a vibrational quantum of approx. 2000 cm^{-1}. Further bifurcations are found at a distance corresponding to the second nearest neighbours of the lattice. Moreover, interferences of ingoing and outgoing wavepackets can be recognized, e. g. at $t \approx 20 \ldots 22$ fs.

Due to the off–diagonal elements of the representation of the potential energy in the basis of SASHs (see Eq. 4.11), higher SASH states of the same irreducible representation are populated within a timescale of a few femtoseconds. The correlation between the angular wavefunction and the radial wavepacket dynamics is nicely illustrated in the second and third column of Fig. 4.9. For

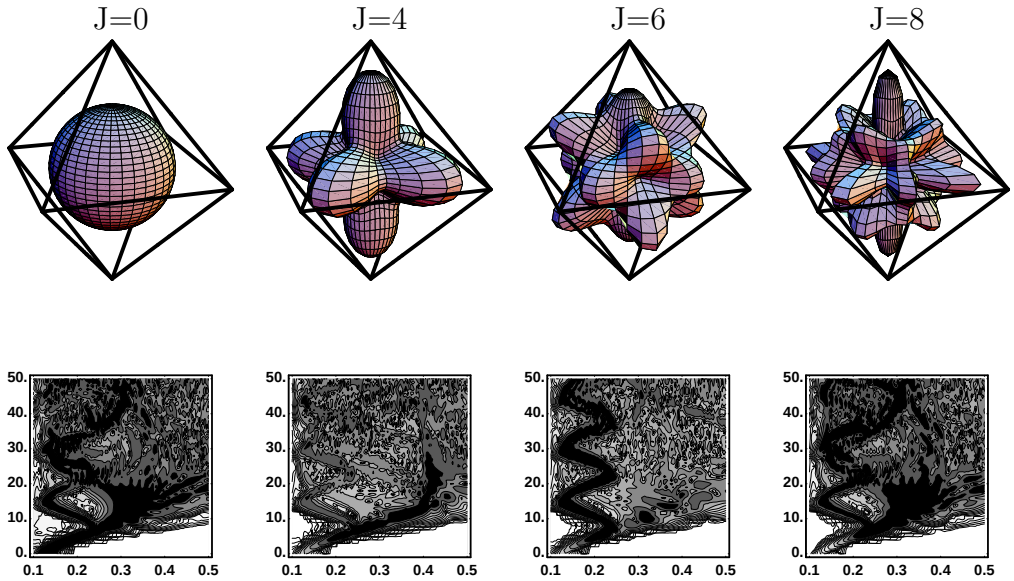

Figure 4.9: Hydrogen atom wavepacket dynamics of HCl photodissociation in Ar(fcc) for the initial state $J = 0$ (A_{1g}). The upper part shows the SASHs used as basis functions, the lower part shows the square of the time–dependent radial wavefunctions (Abscissa: r in nm, ordinate: t in fs). From C.3.

$J = 4$ the strong angular focussing along the crystallographic $< 100 >$ leads to neglibible reflection from the nearst neighbours ($< 110 >$) but to strong caging by the second coordination shell. Vice versa, the wavepacket dynamics in the $J = 6$ state is characterized by very strong caging inside the first shell leading to (almost) coherent vibrations.

Rotationally Excited States As examples for the photodissociation dynamics of rotationally excited molecules in a matrix, let us consider two sublevels of the $J = 3$ state, namely the A_{2u} and the T_{2u} state which are separated by 6 cm^{-1} in the electronic ground state, see Tab. 4.1. As could be expected, the left column of Fig. 4.10 shows that the $J = 3$ (A_{2u}) permits almost unhindered cage exit due to its preferrential orientation along the $< 111 >$ axes of the fcc lattice. However, the coupling to higher rotational states of the A_{2u} representation reduces the total cage exit probability. While the $J = 7$ and $J = 11$ states also prefer orientations with a strong tendency for cage exit, the $J = 9$ state (as well as some of the higher states not shown in the figure) reduce the total exit probability because the corresponding wavepacket dynamics exhibits oscillatory motions within the cage formed by the nearest neighbour atoms.

A different picture is obtained for the T_{2u} sublevel of the $J = 3$ state, see Fig. 4.11. For this irreducible representation, three out of the first four SASHs exhibit maxima along the crystallograhic $< 110 >$ directions. Accordingly, the wavepacket dynamics in these rotational states is dominated by (almost) coherent vibrations within the inner solvent cage with very minor probabilties

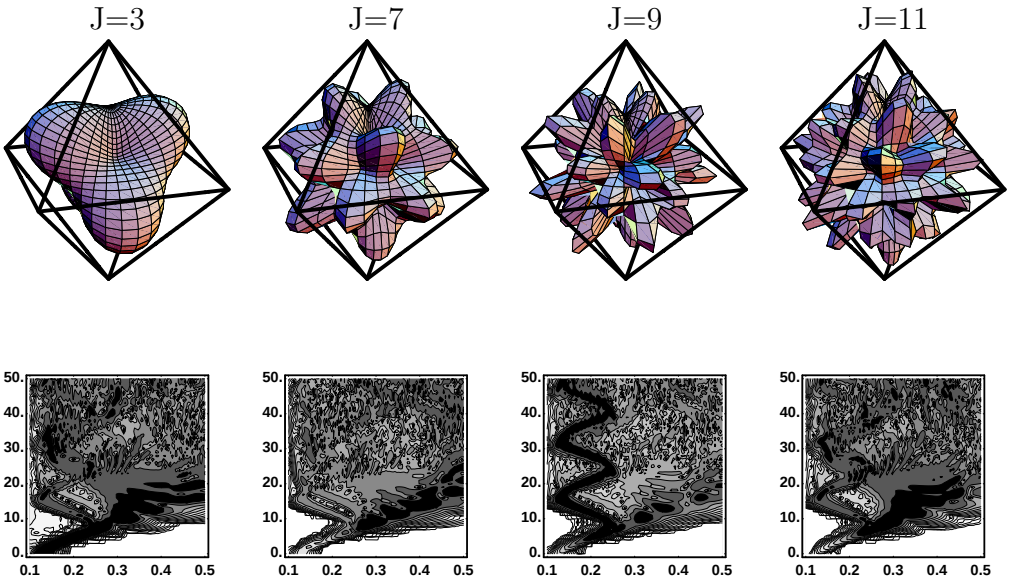

Figure 4.10: Same as Fig. 4.9 but for initial state $J = 3$ (A_{2u}).

of finding the H atom at larger distances from the Cl atom. Again, coupling to even higher rotational states leads to corrections of this picture. For example, there is a relatively high cage exit probability for the $J = 9$ state.

4.6.2 Cage Exit Probabilties

Our findings are summarized in this subsection where we want to consider the cage exit probability versus the initial ro–vibrational state of the guest molecule in the rare gas matrix. In analogy to the wavepacket approch to reactive (bimolecular) scattering [14], we define a projection operator which equals unity if the hydrogen atom is found outside the first coordination shell and which is zero inside this shell. Then the cage exit probability is simply obtained as the expectation value of this operator

$$P(t) = \sum_{JM} \int_{r=r_{NN}}^{\infty} |\phi_{JM}(r,t)|^2 \tag{4.13}$$

where r_{NN} stands for the nearest neighbour distance of the Ar (fcc) lattice[8]. Here we calculate this quantity for two different times. The cage exit after one vibrational period (15 fs) is regarded as *immediate cage exit*. The further increase of P(t) up to 10 vibrational periods (150 fs) is termed *delayed cage exit*. Although our model does not account for non–adiabatic transitions and recombination in the electronic ground state, we know from the literature [230, 277, 278] that recombination can be expected to play an important role for longer timescale which cannot be considered here.

[8]Note that it is straightforward to calculate the range of migration of photodissociated H atoms in an Ar matrix by varying the lower boundary of the radial integration in Eq. (4.13). This quantity could indeed be measured in experiments with layered rare gas crystals [376]

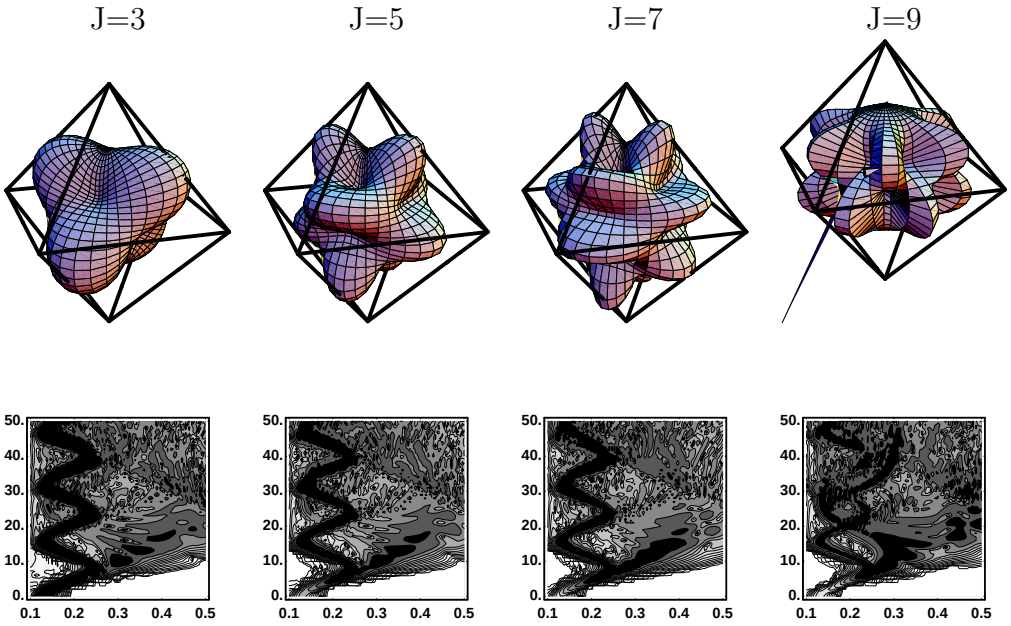

Figure 4.11: Same as Fig. 4.9 but for initial state $J = 3$ (T_{2u}).

First, let us consider the dependence of immediate cage exit probability $P(t = 15fs)$ as a function of the initial rotational state of the HCl molecule as displayed in Fig. 4.12 (a). We assume the molecule to be initially in its vibrational ground state. The upper left part of the graphics shows different values of P for the different rotational states varying from 24% to 56%. For $J = 0$ (A_{1g}) and $J = 1$ (T_{1u}) the probabilities are similar. However, the two sublevels of the $J = 2$ state (E_g, T_{2g}) exhibit a different influence of the cage effect. Clearly, there is much stronger caging for the T_{2g} state because of its $< 110 >$ orientation. These differences are even stronger for the sublevels of the $J = 3$ state. As has been illustrated above, the cage effect is strongest for the T_{2u} state. In contrast, the A_{2u} and T_{1u} state allow a more facile cage exit than the isotropic $J = 0$ (A_{1g}) state.

This sensitivity of the cage effect is diminished at longer times. After 10 vibrational periods ($t = 150$ fs) the probability for delayed cage exit depends only weakly on the initial rotational state of the HCl molecule. Moreover, in some case, also the order of the probabilities is reversed. This is a consequence of the coupling to more (and higher) rotational states.

Another interesting aspect is the dependence of the dynamics of the cage exit on the initial vibrational state of the molecule. Our results are shown in Fig. 4.12 (b). It can be seen that the immediate cage exit probability strongly decreases for increasing vibrational quantum number v. This can be explained in the framework of the Condon approximation. Upon vertical transition of a vibrationally excited wavefunction from the electronic ground state to the excited state, the outer lobes gain much less energy on the steep, repulsive potential curve of the $^1\Pi$ state (see Fig. 4.2). This is also indicated on the

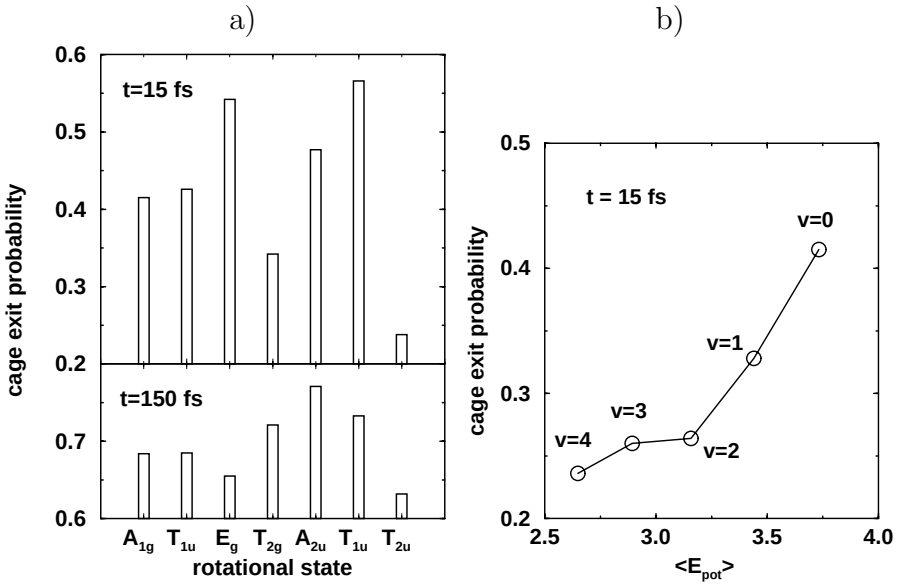

Figure 4.12: Cage exit probability upon photodissociation of HCl in Ar(fcc). a) Dependence of immediate ($t = 15$ fs) and delayed ($t = 150$ fs) cage exit probability on initial rotational state (for $v = 0$). b) Dependence of immediate ($t = 15$ fs) cage exit probability on initial vibrational state (for $J = 0$, A_{1g}).

abscissa denoting the potential energy of the wavepacket upon excitation. Note that especially the low energies for high values of v suggest that vibrational excitation may serve to determine the energetic threshold for cage exit more exactly. In this way, investigations of the photodissociaton dynamics of matrix in molecules may be used to calibrate interaction potentials, in particular the H–Ar repulsion.

4.6.3 Absorption Spectra

Apart from measuring the cage exit probability in experiments with multi–layered rare gas crystals [376] the main observable in a measurement of photodissociation of matrix–isolated molecules is the absorption spectrum. The standard way to obtain a stationary absorption spectrum from a time–dependent wavepacket formalism is the following [377]: The initial state is assumed to be instantaneously excited (Condon–Approximation) and the wavepacket created in the excited state is propagated in time. Then the (complex) autocorrelation is calculated as the overlap between the wavepacket at time $t > 0$ and the initial one ($t = 0$)

$$S(t) = \langle \psi(t) | \psi(0) \rangle = \sum_{JM} \int_0^\infty dr\, \phi^*_{JM}(r,t) \phi_{JM}(r,0) \quad . \tag{4.14}$$

An absorption spectrum is then obtained as the Fourier transform of the autocorrelation function[9]. It is noted that this is equivalent to the conventional, i. e. time–independent way to obtain spectra using the Condon approximation [377].

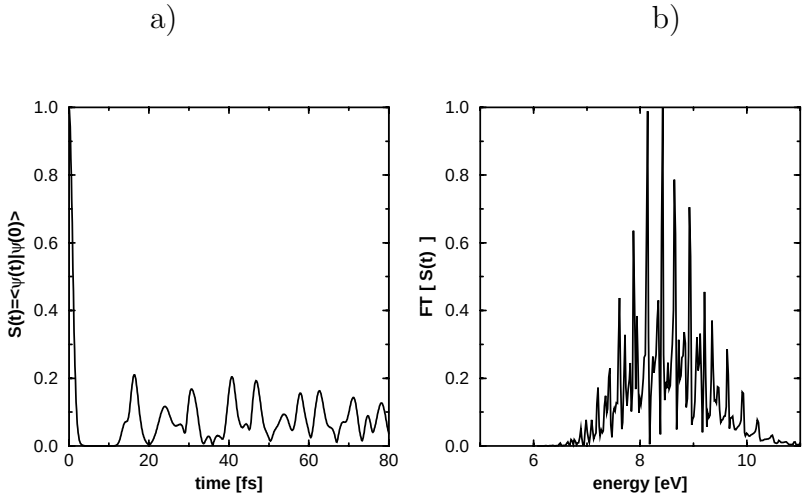

Figure 4.13: a) Autocorrelation function and (b) absorption spectrum of HCl in an icosahedral Ar_{12} cluster.

Our results for the example of HCl photodissociation in an icosahedral Ar_{12} cluster are displayed in Fig. 4.13. The initial state is assumed to be the ro–vibrational ground state. Assuming a frozen rare gas environment or, equivalently, infinitely heavy rare gas atoms, the autocorrelation function of the cluster is obtained from propagating the H atom wavepacket only[10]. After a steep fall–off of the autocorrelation function within the first three femtoseconds, there are partial recurrences at later times. These recurrences are related to rotational states that display a mainly vibrational wavepacket dynamics within the cage, see e. g. the $J = 6$ state in Fig. 4.9. For increasing time, the further rephasing and mixing of more and higher rotational states results in a structure–less autocorrelation function for longer times. The corresponding spectrum is shown in part (b) of the figure. It exhibits a broad envelope around 8.5 eV which corresponds to the energetic difference of the $v = 0$ wavepacket in the ground and excited state. The width of approx. 2 eV is inversely proportional to the duration of the initial fall–off of the autocorrelation function. Note that the envelope alone would correspond to the spectrum of the isolated molecule (no recurrences!). The quasi–periodic structure superimposed onto the broad peak is a remnant of the vibrations inside the cage. Indeed, the distance of about 0.27 eV between the main spectral peaks corresponds to a vibrational period of approx. 15 fs for the H atom rattling between the Cl atom and the surrounding

[9] Alternatively, spectral line positions, intensities, and widths can be obtained from a harmonic inversion via a filter diagonalization of the autocorrelation function [378,379,380]. The advantage is that considerably shorter propagation times are needed to achieve the same spectral resolution [381]

[10] For remarks on a more realistic spectrum, see section 4.6.6.

Ar atoms. However it has to be kept in mind that this spectrum is obtained only from the H atom wavepacket dynamics assuming a frozen cage. A realistic spectrum is most likely to be structureless, see our remarks below in Sec. 4.6.6.

4.6.4 Cage Dynamics

All the investigations of the photodissociation of matrix–isolated molecules presented above have been relying on the assumption of negligible energy dissipation into the rare gas matrix, i. e. the matrix was assumed to be frozen. This is a reasonable approximation for the following two reasons: (1) According to Eq. (3.12), the maximum energy transfer in a hard collision between H and Ar atoms (mass ratio 1:40) is limited to only 10%. (2) Even if a considerable amount of energy were transferred to the rare gas environment, this would not open any new reactive channels because the rare gas atoms are closely packed and cannot freely rearrange. However, the sudden and punctual release of energy [382] can give rise to excitation of phonons [383], and possibly to shock waves [384] or to local melting [385] which we intend to investigate in future work.

In a small cluster, however, an energy transfer to the rare gas solvation can in principle lead to (partial or total) fragmentation of the cluster by evaporation of rare gas atoms [11]. For the smallest cluster systems with only a single rare gas atom, this fragmentation process can be simulated quantum mechanically in all three degrees of freedom [268, 269, 270, 267]. For larger systems, a quantum classical molecular dynamics (QCMD) approach presents a viable alternative (see Sec. 4.3.4). Examples from the literature span the range from the systems with a single solvent atom [262] up to matrix studies [274]. Also the photodissociation dynamics of HCl adsorbed on insulator surfaces has been treated using a QCMD approach [386, 387].

In the following, we want to apply the QCMD approach presented in Sec. 4.3.4 to the case of a first complete solvent shell, i. e. the icosahedral $HClAr_{12}$ cluster. We assume the HCl molecule to be initially in its ro–vibrational ground state ($J = 0, v = 0$), and we propagate the three–dimensional H atom wavepacket and the trajectories of the 13 classical particles self–consistently using the PICKABACK algorithm [388]. For the hydrogenated system, we see that within a timespan of 200 fs (or more than 12 vibrational periods) the hydrogen atom looses about 10% of its initial energy, see left part of Fig. 4.14 [12]. The (very weak) undulations of the curve are connected with the temporal structure of the oscillatory motion of the radial wavepackets for some of the SASHs as illustrated in Fig. 4.9. However, for longer times, the wavepackets dephase completely and the curve becomes smooth. The decreasing slope of the curve indicates that after 200 fs most of the probability amplitude connected with the H atom wavepacket has already escaped from the cage so that there is

[11] The fragmentation upon photodissociation bears many similarities with the fragmentation upon association reactions in a cluster, see our findings on solvent–induced stabilization in Chap. 3 of this thesis.

[12] Note that an energy transfer of only 10% within 12 vibrational periods is considerable less than the upper boundary estimated for the case of a "hard" collision (see above).

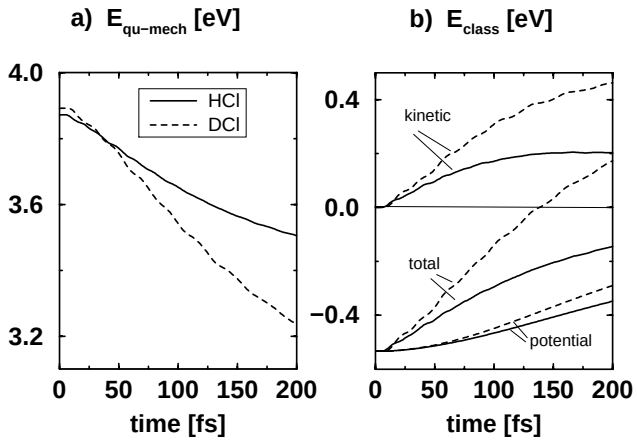

Figure 4.14: QCMD simulation of HCl/DCl photodissociation in icosahedral $HClAr_{12}$ clusters. Parts (a) and (b) of the figure show the energy of the quantum–mechanical and of the classical subsystem, respectively. Solid curve: HCl, dashed curve: DCl.

not much more energy transfer on a longer timescale. It is interesting to compare this result with the deuterated system. Despite of the slower vibrational motion, the D atom looses almost twice as much energy which is due to the larger mass.

Within the restriction to the totally symmetric irreducible representation A_g of the icosahedral point group (I_h), energy can be only dissipated into the (totally symmetric) breathing mode of the icosahedral solvation shell, see the right part of Fig. 4.14. In the case of the H atom, the transferred energy gives rise to a breathing vibration with a vibrational period on a picosecond timescale. In contrast, the larger energy transfer from a D atom brings the total energy of the heavy atoms into the regime of positive total energies. Hence, as a consequence of the collisions with the photodissociated D atom, the cluster fragments completely into Cl + 12 Ar.

In summary, we note that the excess energy of 3.9 eV gained by excitation of the HCl molecule into the $^1\Pi$ state is enough to evaporate even a much larger cluster of several complete solvation shells. Hence, the outcome of the photochemical event is determined by the competition between two different processes, i. e. the escape from the cage and the energy transfer while rattling inside the cage. If the former process is faster, the cluster stays intact and will only be vibrationally excited; if the latter process is more efficient, evaporation of solvent particles will dominate.

One word of caution has to be added: The present calculations have been carried out within the totally symmetric irreducible representation assuming the classical particles to be initially in perfect icosahedral symmetry, i. e. for $T \to 0$. This implies that there are only two possible outcomes of the reaction: either none or all twelve solvent particles are evaporated. The presence of thermal motions for $T > 0$ results in a loss of symmetry. However, for not too large

deviations from the icosahedral symmetry, we expect very large amplitudes of rotational or librational wavefunctions for the H atom resulting in a relatively large number of Ar atoms to be ejected from the cluster. This speculation is in contrast to the results of a classical trajectory study of $HFAr_{12}$ where the most likely event is the evaporation of a single Ar atom [272]. A final judgement of this discrepancy would be numerically extremely expensive because of the large number of spherical harmonics needed in a CCWP *ansatz* without symmetry restrictions.

4.6.5 Summary

In the work presented in C.2 and C.3 it has been demonstrated that the quantum yield of a photodissociation reaction of matrix–isolated hydrogen halide molecules can be controlled, to some extent, via the initial ro–vibrational state of the guest molecule. In an experiment, this can be realized by an infrared (IR) pre–excitation of the molecule into the respective ro–vibrational state, and by subsequent photodissociation initiated by ultrashort ultraviolett (UV) light pulses[13]. At present, these experiments are in preparation in the labs of the FU Berlin [**?**].

The idea of performing photochemistry with vibrationally pre–excited molecules has lead to the concept of vibrationally mediated chemistry. Since its very beginnings in the 1970s [279, 280, 281] it has been applied to gas phase molecules, in particular to control the branching ratio of competing bond cleavages [282, 283, 284, 285]. In the present work (C.3) we have been extending the idea of vibrationally mediated chemistry towards two directions. On the one hand, this investigation presents a first step towards an application of this concept in the field of condensed phases. On the other hand, rotational effects have been included for the first time. Hence, this work opens the way to a **rotationally mediated photochemistry** of matrix isolated molecules. However, we do not want to conceal the limitations of this concept. First, our results seem to indicate that there is a limitation towards short timescales. Second, the mechanism seems to be limited to weakly bound systems where nearly free rotations or other large–amplitude motions are possible.

A promising further extension of the concept of ro–vibrationally mediated photochemistry is to utilize the properties of the photodissociated hydrogen atoms in a further (pseudo–)bimolecular reaction. This possibility has been demonstrated in recent work, where the Cl_2 formation upon HCl photolysis in $HCl\cdots Ar_{12}Cl$ [217] as well as in $HCl\cdots Cl$ [389] was studied. In theses clusters, the rotational motions of the HCl molecule are more strongly hindered by the anisotropy of the potential energy surface and the dynamics is characterized by librational motions, see also our discussion in Sec. 4.5.5. Hence, the novel mechanism to control the reaction yield is termed **librationally mediated photochemistry**.

[13] The IR pre–excitation and the UV photodissociation do not have to be in immediate succession because of the extremely slow ro–vibrational relaxation of these systems on a microsecond to millisecond timescale, see e. g. Ref. [365] or many contributions in [243].

4.6.6 Outlook

The QCMD calculations presented above offer the advantage of being computationally not too expensive and providing reasonable results for quantities that do not depend on the quantum mechanical phase of the heavy atom wavefunction. Examples of such phase–independent quantities are expectation values such as the cage exit probability or the cluster fragmentation discussed previously. However, spectroscopic quantities such as the absorption or Raman spectrum are calculated – in the time–dependent picture – from correlation functions of wavefunctions characterizing the full system [35]. Then the phase information of the wavefunctions can become extremely important. Typically, the inclusion of more modes leads to a strong damping or, eventually, to a disappearing of the recurrence structure of the autocorrelation function leading to a structure–less spectrum. This is confirmed in a preliminary 4–D calculation of the photodissociation of $HClAr_{12}$ (I_h) including the symmetrical breathing mode of the solvent cage. Also in the experimental spectrum for HCl in Ar(fcc) there is no visible vibrational structure within the experimental resolution [376].

One of the simplest ways to extend the QCMD model in order to approximate the quantum mechanical phase of the full system under investigation is to replace the classical dynamics by Gaussian wavepacket dynamics [390]. This leads to the quantum–semiclassical molecular dynamics (QSMD) model which has also been applied to the photodissociation dynamics of ArHCl [263]. Another example is the work of Ref. [391, 392] where a QSMD model is used to simulate spectra of particles adsorbed in a zeolite. If details of the solvent dynamics are not of interest, the reduced density matrix approach can be an alternative. In recent work on HCl in Ar(fcc), the dissipative wavepacket dynamics of the hydrogen atom under the stochastic influence of the rare gas atoms has been calculated and absorption spectra have been simulated [275].

An alternative to the QCMD or QSMD models discussed above is the "classicle separable potential" (CSP) model which has been developed during the past few years. It is based on a time–dependent self–consistent field approach (TDSCF) [14] [393, 394, 326, 395]. The computational bottleneck of the TDSCF which lies in the integrations to obtain the effective, time–dependent potentials is circumvented in the CSP model in the following way. First, a set of classical trajectories is propagated to generate effective, one–dimensional potentials. Based on these potentials, a quantum–mechanical TDSCF propagation is carried out. This technique provides a new tool to calculate the quantum dynamics for moderately quantal systems with a few hundred degrees of freedom [396, 397, 398, 399]. Currently, CSP simulations of HCl in icosahedral Ar_{12} are in preparation [301].

The next step of sophistication would be to go beyond the restrictions of a separable *ansatz*. In analogy to the multi–configuration extensions of TDSCF into MC–TDSCF methods [400, 401, 402, 403, 404, 405], also the CSP method has recently been developed further to incorporate also non–separability in a configuration interaction (CI–CSP) approach [406, 407, 408, 381].

Finally, we have to mention that we have been restricting ourselves to adi-

[14] Sometimes the TDSCF is also referred to as time–dependent Hartee (TDH) method.

abatic dynamics on a single potential energy surface. This was justified by the fact that (1) we considered the photodissociation dynamics only on a very short time scale where non–adiabatic transition back to the ground states do not play a role, and (2) the three excited state potential energy curves of the $^1\Pi$, $^3\Pi$, and $^3\Sigma$ states are not too different from each other [300]. So far, the non–adiabatic dynamics of the class of systems considered here has been only treated using a surface hopping approach. Results for HCl in Ar matrices [226, 409, 230] and clusters [277] show that on the timescale of a few hundred femtoseconds the spin–orbit coupling plays a major role in the non–adiabatic dynamics.

Chapter 5

Extended Summary

The present thesis is concerned with the dynamics of elementary chemical reactions. In particular, the processes of bond formation (association) and of bond cleavage (dissociation) are studied. Both photo–induced and solvent–induced reaction mechanisms are elucidated. By embedding simple diatomic model systems in rare gas clusters and matrices, the transition of the dynamics of making and breaking of chemical bonds from the gas phase to the condensed phase is systematically investigated.

Methodology. The methodologies employed here depend on the size of the systems as well as on the quantities of interest. They range from purely classical trajectory simulations or quantum–classical hybrid techniques for larger systems up to quantum mechanical (exact and perturbative) wavepacket propagations for the smallest (diatomic) systems. In the latter case also the interaction with external, time–dependent electromagnetic fields of pulsed lasers is accounted for. Fully three–dimensional quantal treatments of continuum wavefunctions and wavepackets have been adapted from scattering theory and further developed. In particular, in the present work rotational effects on photoassociation processes such as shape resonances and rotational coherence have been considered for the first time. For photodissociation dynamics in clusters and matrices, a highly efficient technique for symmetry adaption of wavepackets has been developed.

Photo–induced stabilization of collision pairs. In chapter 2 photoassociative collisions of two colliding atoms are treated. By stimulated emission of light, a collision pair can be stabilized to form a ground state molecule. The work in A.1 and in A.2 represents the first studies of ground state photoassociation by infrared picosecond light pulses. It is shown that by simultaneous optimization of the incoming wavepacket and of the laser pulse, photoassociation can be achieved with a high efficiency of $> 80\%$ for a rotation–less model of an O + H collision pair. At the same time, an extremely high vibrational state selectivity close to 100% can be achieved if there is no coincidence with higher–order transitions to lower vibrational states.

An extension of these models to include rotational degrees of freedom is presented in A.4. Taking advantage of the high scattering cross section of shape resonance states we have shown that the efficiency of photoassociation reactions can be considerably enhanced. At the same time, preparation of molecules in specific ro–vibrational states is possible because the condition for a shape resonance is only met for one specific partial wave.

In principle, the process of ground state photoassociation by stimulated emission competes with photoacceleration induced by absorption of photons. In these inelastic free←free transitions, the collision pair is accelerated in the field of the laser pulse. In analogy to the phenomena of above–threshold ionization and above–threshold dissociation, the increase of kinetic energy corresponds to the energy of one or more photons and leads to sharp peaks in the energy distribution of the scattered particles. In A.2 and A.4 this process is investigated and the ranges of suitable laser parameters are explored.

Also the question of electronic state–selectivity has been addressed in the present work. This is especially interesting for molecules where low–lying bound electronic states exist and where ground and excited state photoassociation are eligible in a similar frequency regime. It is demonstrated in A.3 for the example of the OH radical that even in these cases various control mechanisms exist. Apart from the different polarization of permanent and transition dipole moments, effective control can be exerted through variation of the scattering energy of a collision pair.

When going to even shorter pulses in the femtosecond regime, coherent superpositions of ro–vibrational states can be excited. In modern pump–probe experiments the time evolution of wavepackets be oberserved in real time. This has been illustrated in A.5 for the example of the exciplex formation of the mercury dimer. On the borderline of classical and quantum mechanics, (fractional) revivals in the wavepacket dynamics are predicted. The fast and the slow timescales of the pump–probe experiments of Marvet and Dantus are interpreted in terms of quantum beats of different vibrational and rotational states, respectively, which have been coherently excited in the photoassociation process. Note that these spectral features persist even for relatively high temperatures. Moreover, by excluding the possibility that the observed signals originate from van der Waals precursors, our results provide evidence for the bimolecular nature of this experiment thus rendering it one of the first of its kind.

Solvent–induced stabilization of collision pairs. In chapter 3 the (radiation–less) stabilization of collision pairs in the presence of a solvent is studied. In particular, we investigated solvent effects on hydrogen halide association reactions by attaching a rare gas "microsolvation" to the halide reagent, see B.1. The follwing two cases serve as models: For the H + Cl$\cdots$Ar system the existence and the extent of the third–body or "chaperon" effect is explored. Already a single solvent atom can stabilize a collision pair by removing some energy from it such as to keep it from redissociating. Due to kinematic constraints for the energy transfer from the H–Cl mode to the Cl–Ar mode, we find ro–vibrationally hot products while only a very small fraction of the available energy is found in product translation. Among the most interesting predictions is the discovery of very long–lived orbiting resonances with lifetimes in the order of picoseconds.

To explore the transition from gas to condensed phase dynamics, the cage effect on association reactions was studied in B.2 for the H + Cl$\cdots$Ar$_{12}$ system where a first complete solvation shell shields the Cl reactant. We found a pronounced structural transition between $T = 40$ K and $T = 45$ K in MD simulations of ClAr$_{12}$. The reactivity to form HCl molecules in collisions with a H atom can be extremely sensitive to the melting–like transition. Our novel approach can serve to elucidate more on the much debated question of "phase transitions" in finite systems. In this way, reactive collisions could provide an alternative to the spectroscopy of chromophores embedded in solvent clusters.

Finally, the studies of association reactions are extended towards larger sys-

tems in order to model nucleation from the gas phase towards the formation of bulk matter. In particular, associative collisions of alkali halide molecules and clusters are studied in B.3 as a model for cluster growth from the gas phase. The collision complexes investigated here are large enough to redistribute the excess energy among their abundant internal degrees of freedom for a relatively long time before they finally are stabilized by evaporation. The cluster sizes considered here (up to the tetramer) are on the border of the validity of statistical RRKM models. While general trends can be explained in terms of these models, a detailed microscopic study is necessary to understand the quantitative effects.

Photodissociation of molecules in clusters and matrices. The process of light–induced bond breaking is investigated in chapter 4. Here our special emphasis is on the cage effect delaying or hindering the photofragments from separation and on possible cage exit mechanisms. In analogy to our treatment of solvent–induced association reactions, hydrogen halide molecules in the environment of rare gas clusters and matrices are chosen as model systems. As a presupposition for the understanding of the photodissociation dynamics, the vibrational and rotational spectroscopy of these guest–host systems is investigated first.

Vibrational frequency shifts of the guest molecule serve to characterize the structure and size of the rare gas host systems. Using vibrationally adiabatic atom–molecule potentials the following two effects are found in C.1: (1) Icosahedral and octahedral symmetry give rise to distinctly different frequency shifts and (2) between three and five complete solvation shells are required in order to reach convergence of the shift towards the value for bulk matter.

The rotational spectroscopy is characterized by nearly free rotations of the hydrogen halide molecules with respect to the rare gas cluster (C.2) or matrix (C.3) because the anisotropy of the atom–molecule interaction cancels to a large extent for systems with closed solvation shells. Apart from small but characteristic splittings of degenerate energy levels, the main influence of the solvation is that it imposes its symmetry on the rotational wavefunctions.

Based on this knowlegde of the initial state, the excited state dynamics is investigated. The hydrogen atom wavepacket motion shows distinctly quantal features such as bifurcations and interferences. The initial rotational wavefunctions have important implications on this dynamics i. e. the cage exit probability sensitively depends on its initial rotational state. Furthermore, the quantum yield of a photodissociation reaction also depends on the vibrational state of the guest molecule.

As a consequence, we suggest a novel extension from vibrationally to rotationally, or ro–vibrationally mediated chemistry for isolated molecules in clusters (C.2) or matrices (C.3) which proceeds via (far–)infrared pre–excitation of the molecules to be photolyzed. A further development of this idea is the recently proposed librational control of the reactivity of photofragments in small hydrogen containing clusters [389].

Finally, first steps towards a full treatment of the photodissociation dy-

namics of molecules in clusters and matrices have been made. Here quantum–classical or other approximate quantum mechanical methods have to be applied. For clusters with one complete solvation shell the different energy transfer of H versus D atoms leads to vibrational excitation or complete decomposition of the solvent cage, respectively. Another consequence of the cage dynamics is the quenching of resonance structures in the absorption spectrum.

Chapter 6

Ausführliche Zusammenfassung

Die vorliegende Habilitationsschrift behandelt die Dynamik elementarer chemischer Reaktionsschritte. Insbesondere der Prozeß der Bindungsknüpfung (Assoziation) und des Bindungsbruches (Dissoziation) werden studiert. Sowohl lichtinduzierte als auch stoßinduzierte Reaktionsmechanismen sind Gegenstand der Untersuchungen. Anhand der Einbettung einfacher zweiatomiger Modellsysteme in Cluster und Matrizen aus Edelgasatomen wird der Übergang der Dynamik des Knüpfens und Brechens chemischer Bindungen von der Gasphase zur kondensierten Phase systematisch untersucht.

Methodik. Die zur Anwendung kommenden Methoden hängen sowohl von der Größe der Systeme als auch von den interessierenden Größen ab. Sie reichen von rein klassischen Trajektoriensimulationen oder quanten-klassischen Hybridverfahren für größere Systeme bishin zu quantenmechanischen (exakten oder störungstheoretischen) Wellenpaket-Propagationen für die kleinsten (zweiatomigen) Systeme. Bei letzteren wird auch die Wechselwirkung mit äußeren, zeitabhängigen elektromagnetischen Feldern gepulster Laser mit eingeschlossen. Vollständig dreidimensionale quantenmechanische Behandlungsweisen von Kontinuums-Wellenfunktionen und Wellenpaketen werden aus der Streutheorie übernommen und weiterentwickelt. Dabei wird der Effekt der molekularen Rotation auf Photoassoziations-Prozesse, insbesondere das Auftreten von quasi-gebundenen Zuständen und Rotations-Kohärenzen, zum ersten Mal berücksichtigt. Zur Beschreibung der Dynamik der Photodissoziation kleiner Moleküle in Clustern und Matrizen ist eine effiziente Technik zur Symmetrieadaptierung von Wellenpaketen entwickelt worden.

Photoinduzierte Stabilisierung von Stoßpaaren. In Kapitel 2 werden photoassoziative Stöße zweier Atome betrachtet. Durch stimulierte Emission von Licht kann ein Stoßpaar stabilisiert werden, um ein Molekül im elektronischen Grundzustand zu bilden. Die Arbeiten in A.1 und in A.2 stellen die ersten Studien der Grundzustands-Photoassoziation mittels infraroter Pikosekunden-Lichtpulse dar. Durch gleichzeitige Optimierung des einfallenden Wellenpaketes

und des Laserpulses kann Photoassoziation mit einer Effizienz von mehr als 80% für ein rotationsloses Modell eines O + H-Stoßpaares erreicht werden. Gleichzeitig kann eine extrem hohe Selektivität bezüglich des Schwingungszustandes des Produktmoleküls nah bei 100% realisiert werden, wenn keine Koinzidenz mit Übergängen höherer Ordnung vorliegt.

Eine Erweiterung dieses Modells, die auch Rotationsfreiheitsgerade mit einschließt, wird in A.4 vorgestellt. Unter Ausnutzung der hohen Streuquerschnitte quasi-gebundener Zustände haben wir gezeigt, daß die Effizienz von Photoassoziations-Reaktionen wesentlich gesteigert werden kann. Dabei ist die Präparation von Molekülen in spezifischen Schwingungs-Rotations-Zuständen möglich, weil die Bedingung für das Auftreten eines quasi-gebundenen Zustandes nur für eine spezielle Partialwelle vorliegt.

Im Prinzip steht der Prozeß der Grundzustands-Photoassoziation mittels stimulierter Emission in Konkurenz zur lichtinduzierten Beschleunigung durch Absorption. Bei dieser Klasse von inelastischen Stößen werden die Partner im Feld eines Laserpulses beschleunigt. In Analogie zu den Phänomenen der Ionisierung beziehungsweise Dissoziation im Kontinuum entspricht die Zunahme der kinetischen Energie der Energie eines oder meherer Photonen. Dieser Prozeß wird in A.2 and A.4 untersucht und die Bereiche geeigneter Laserparameter werden erkundet.

Auch die Frage der elektronischen Zustands-Selektivität ist in der vorliegenden Schrift behandelt worden. Dies ist besonders für Moleküle interessant, bei denen tiefliegende gebundene elektronische Zustände vorliegen und wo Photoassoziation im Grund- und angeregten Zustand bei vergleichbaren Frequenzen auftreten kann. In A.3 wird für das Beispiel des OH-Radikals gezeigt, daß auch in diesen Fällen verschiedene Kontrollmechanismen existieren. Abgesehen von der verschiedenen Polarisierungsrichtung der permanenten und der Übergangs-Dipolmomente kann effektive Kontrolle auch durch Variation der Streuenergie ausgeübt werden.

Bei Benutzung noch kürzerer Pulse im Bereich von Femtosekunden können kohärente Überlagerungen von Schwingungs-Rotations-Zuständen angeregt werden. Die Zeitentwicklung der so entstehenden Wellenpakete kann in modernen Pump-Probe-Experimenten direkt beobachtet werden. Dies ist in A.5 für das Beispiel der Excimer-Bildung von Quecksilber gezeigt worden. Im Grenzbereich der klassischen und der Quantenmechanik werden (nicht–ganzzahlige) Wiederkehren der Wellenpaketdynamik vorhergesagt. Die schnellen und die langsamen Strukturen in den experimentellen Spektren von Marvet und Dantus können mittels Quantenschwebungen verschiedener Schwingungs- bzw. Rotations-Zustände interpretiert werden. Es ist beachtlich, daß diese spektralen Strukturen sogar für relativ hohe Temperaturen bestehen bleiben. Außerdem konnte durch das Ausschließen des Vorliegens von van der Waals-Vorläufer-Komplexen die bimolekulare Natur des Experiments eindeutig gezeigt werden.

Lösungsmittel-induzierte Stabilisierung von Stoßpaaren. In Kapitel 3 wird die strahlungslose Stabilisierung unter Anwesenheit eines Lösungsmittels

studiert. Im Speziellen haben wir Lösungsmittel-Effekte bei der Assoziation von Wasserstoff-Halogeniden durch Anhängen einer "Mikro-Solvatation" aus Edelgasatomen an den Halogenid-Reaktanden modelliert. Die folgenden beiden Fälle dienen dabei als Prototypen. Anhand des H + Cl-Ar Stoßpaares wird in B.1 die Existenz des Dreikörper- oder "Chaperon"-Effekts erforscht. Dabei hat sich gezeigt, daß schon die Existenz eines einzigen Lösungsmittel-Teilchens ein Stoßpaar stabilisieren kann, indem es einen Teil der Überschußenergie aufnimmt und dadurch das Molekül vom erneuten Dissoziieren abhält. Aufgrund kinematischer Beschränkungen für den Energietransfer von der H-Cl-Mode zur Cl-Ar-Mode liegen die Produkte in sehr hohen Schwingungs-Rotations-Zuständen vor, und nur ein kleiner Bruchteil der verfügbaren Energie geht in Translation der Produkte über. Zu den interessantesten Voraussagen gehört die Entdeckung sehr langlebiger "Orbiting"-Resonanzen mit Lebensdauern im Bereich von Pikosekunden.

Um den Übergang von der Gasphase zur kondensierten Phase zu simulieren und insbesondere den Käfigeffekt bei Assoziations-Reaktionen zu erkunden, wurde in B.2 das System H + $Cl\cdots Ar_{12}$ als Beispiel gewählt, bei dem der Cl-Reaktand von einer ersten vollständigen Solvatationshülle umgeben ist. Wir haben einen deutlichen strukturellen Übergang zwischen $T = 40$ K und $T = 45$ K in MD-Simulationen von $ClAr_{12}$ gefunden. Die Reaktivität bezüglich der Bildung von HCl-Molekülen in Stößen mit einem H-Atom kann äußerst empfindlich von diesem "Schmelzübergang" abhängen. Somit kann dieser neuartige Ansatz dazu dienen, zur vieldebattierten Frage von Phasenübergängen in endlichen Systemen beizutragen und könnte so eine Alternative zur Spektroskopie von Chromophoren in Lösungsmittel-Clustern bieten.

Schließlich sind die Studien von Assoziations-Reaktionen hin zu größeren Systemen ausgeweitet worden, um die Nukleation von kondensierter Materie aus der Gasphase zu simulieren. Dazu werden in B.3 assoziative Stöße von Alkalihalogenid-Molekülen und -Clustern untersucht. Die hier untersuchten Stoßkomplexe sind groß genug, um die überschüssige Energie unter ihren vielen Freiheitsgraden für relativ lange Zeit umzuverteilen, bevor sie schließlich durch Abdampfen von Teilchen abkühlen. Die hier betrachteten Clustergrößen bis zum Tetramer liegen an der Grenze der Gültigkeit statistischer RRKM-Theorien. Während allgemeine Trends noch von diesen Modellen erklärt werden können, ist eine detaillierte mikroskopische Studie nötig, um die Effekte auch quantitativ zu verstehen.

Photodissoziation von Molekülen in Clustern und Matrizen. Der Prozess des lichtinduzierten Bindungsbruchs wird in Kapitel 4 behandelt. Hierbei ist der Themenschwerpunkt auf den Käfigeffekt, der die Trennung der Photofragmente verzögert oder verhindert, und auf mögliche Käfigaustritts-Mechanismen zentriert. Analog zu unserer Behandlung von Lösungsmittel-induzierten Assoziationsreaktionen dienen auch hier Wasserstoff-Halogenid-Mokleküle in der Umgebung von Edelgasclustern und -matrizen als Modellsysteme. Als Voraussetzung für das Verständnis der Photodissoziations-Dynamik wird zunächst die Schwingungs- und Rotations-Spektroskopie dieser Wirts-

Gast-Systeme betrachtet.

Schwingungsfrequenz-Verschiebungen der Gastmoleküle dienen zur Charakterisierung von Struktur und Größe der Edelgas-Wirts-Systeme. Basierend auf schwingungs-adiabatischen Atom-Molekül-Potentialen sind in unseren Untersuchungen in C.1 folgende zwei Effekte gefunden worden. (1) Die ikosaedrische und oktaedrische Symmetrie von Clustern bzw. Matrizen spiegelt sich in deutlich verschiedenen Frequenzverschiebungen wieder, und (2) zwischen drei und fünf vollständige Solvatationshüllen sind erforderlich, um Konvergenz der Verschiebungen gegen den Wert für unendlich ausgedehnte Materie zu erreichen.

Die Rotationspektroskopie ist gekennzeichnet durch annähernd freie Rotation der Gast-Moleküle, weil die Anisotropie der Atom-Molekül-Wechselwirkung sich für Systeme mit geschlossenen Lösungsmittelhüllen weitgehend aufhebt. Abgesehen von kleinen aber charakteristischen Aufspaltungen der entarteten Energieniveaus besteht der wesentliche Einfluß der Umgebung darin, daß sie den Rotations-Wellenfunktionen ihre Symmetrie aufzwingen.

Aufbauend auf dieser Kenntnis der Anfangszustände, wurde die Dynamik im angeregten Zustand untersucht. Die Wellenpaket-Bewegung des H-Atoms weist quantenmechanische Merkmale, wie z.B. Bifurkationen und Interferenzen auf. Der anfängliche Rotationszustand hat wichtige Implikationen für die Photodissoziations-Dynamik, insbesondere hängt die Wahrscheinlichkeit für einen Käfigaustritt empfindlich von ihm ab. Außerdem hängt die Quantenausbeute der hier untersuchten Photodissoziations-Reaktionen auch vom Schwingungszustand der Gastmoleküle ab.

Schlußfolgernd schlagen wir eine neuartige Erweiterung des Konzepts der schwingungsgesteuerten hin zu einer rotationsgesteuerten Photochemie isolierter Moleküle in Clustern (C.2) oder Matrizen (C.3) vor, die mittels einer Infrarot-Anregung der zu photolysierenden Moleküle kontrolliert wird. Eine Weiterentwicklung dieses Konzeptes besteht in der kürzlich vorgeschlagenen Librations-Kontrolle der Reaktivität von Photofragmenten in wasserstoffhaltigen kleinen Clustern [389].

Schließlich sind auch erste Schritte in Richtung auf eine vollständige Behandlung der Photodissoziations-Dynamik von Molekülen in Clustern und Matrizen unternommen worden. Hierbei müssen quanten-klassische oder andere Näherungsverfahren angewendet werden. Für Cluster mit einer vollständigen Solvatationshülle führt der unterschiedliche Energietransfer von H und D-Atomen zu Schwingungsanregung bzw. vollständiger Fragmentierung des Käfigs. Eine weitere Konsequenz der Käfigdynamik besteht in einer Auslöschung der Resonanzstruktur des Absorptionsspektrums.

Danksagung

An dieser Stelle möchte ich mich bei allen denjenigen bedanken, ohne deren Hilfe das Zustandekommen dieser Arbeit sicherlich nicht möglich gewesen wäre. Insbesondere sind meine wissenschaftlichen Betreuer während der letzten Jahre zu nennen, Prof. J. Manz an der Freien Universität (FU) in Berlin sowie Prof. R. B. Gerber, bei dem ich sowohl an der *Hebrew University (HUJI)* in Jerusalem als auch an der *University of California (UCI)* in Irvine (Kalifornien) mehrere Male äußerst gastfreundlich aufgenommen wurde. Sie haben, jeder auf seine eigene Weise, mir mit Rat und Tat zur Seite gestanden und durch ihr wohlwollendes Interesse ganz entscheidend zum Erfolg dieser Arbeit beigetragen.

Ebenso wenig möchte ich versäumen, mich auch bei den Kollegen in der Arbeitsgruppe an der FU Berlin zu bedanken, durch deren tatkräftige Hilfe die hier vorgestellten Arbeiten während der letzten Jahre entstanden sind. Vor allem möchte ich Peter Backhaus, Mikhail Korolkov, Britta Meißner, Boris Proppe sowie Peter Saalfrank für die anregende und interessante wissenschaftliche Zusammenarbeit danken. Außerdem waren Holger Busse und Markus Oppel mit ihren zahlreichen Hilfestellungen im Zusammenhang mit den auftretenden Computerfragen sowie Markus Miertschink mit der Erstellung von Visualisierungen beteiligt. Darüber hinaus sei auch allen anderen gedankt, die mir auch auf die eine oder andere Weise geholfen haben und vor allem zur angenehmen Atmosphäre in der Arbeitsgruppe beigetragen haben.

Weiterhin bleiben noch die wissenschaftlichen Kontakte außerhalb der FU zu nennen, die auch ganz wesentlich zur Bereicherung der vorliegenden Arbeit beigetragen haben. Dazu zählen vor allem Pavel Jungwirth und Petra Ždánská von der Tschechischen Akademie der Wissenschaften in Prag, Christoph Schütte, Peter Nettesheim und Martin Holz vom benachbarten Konrad–Zuse–Zentrum sowie Prof. R. S. Berry von der *University of Chicago*.

Schließlich freue ich mich über die langjährige finanzielle Unterstützung meiner Vorhaben durch die Minerva–Gesellschaft, die Deutsche Forschungsgemeinschaft (DFG), den Deutschen Akademischen Austauschdienst (DAAD) und die Volkswagenstiftung. Neben der Bereitstellung von Stellen war die Finanzierung von Reisen zum Besuch von Projektpartnern und zu Konferenzen im In– und Ausland auch über den rein wissenschaftlichen Aspekt hinaus sehr förderlich.

Besonderen Dank verdient meine Freundin Anette, die mir in den vergangenen Jahren stets einen starken Rückhalt gewährt hat und mich immer wieder bestätigt hat. Vor allem während der letzten Monate konnte ich immer auf ihr Verständnis bauen.

Bibliography

[1] R. G. Gilbert and S. C. Smith, *Theory of Unimolecular and Recombination Reactions*, Blackwell, Oxford, 1990.

[2] G. G. Hammes, *Principles of Chemical Kinetics*, Academic, New York, 1978.

[3] P. J. Robinson and K. A. Holbrook, *Unimolecular Reactions*, Wiley, New York, 1972.

[4] S. Glasstone, K. J. Laidler, and H. Eyring, *The Theory of Rate Processes*, McGraw-Hill, New York, 1941.

[5] J. I. Steinfeld, J. S. Francisco, and W. L. Hase, *Chemical Kinetics and Dynamics*, Prentice Hall, Englewood Cliffs, NJ, 1989.

[6] H. Eyring and M. Polanyi, Z. Phys. Chem. **12**, 279 (1931).

[7] J. M. Farrar and Y. T. Lee, Ann. Rev. Phys. Chem. **25**, 357 (1974).

[8] D. R. Herschbach, Adv. Chem. Phys. **10**, 319 (1966).

[9] J. C. Polanyi, Acc. Chem. Res. **5**, 161 (1971).

[10] M. Child, *Molecular Collision Theory*, Academic, London, 1974.

[11] W. H. Miller, editor, *Dynamics of Molecular Collisions*, volume B, New York, 1976, Plenum.

[12] R. B. Bernstein, *Chemical Dynamics via Molecular Beam and Laser Techniques*, Oxford University, New York, 1982.

[13] R. D. Levine and R. B. Bernstein, *Molecular Reaction Dynamics and Chemical Reactivity*, Oxford University, Oxford, 1987.

[14] N. Balakrishnan, C. Kalyanaraman, and N. Sathyamurthy, Phys. Rep. **280**, 79 (1995).

[15] R. E. Wyatt and J. Z. H. Zhang, editors, *Dynamics of Molecules and Chemical Reactions*, New York, 1996, Dekker.

[16] G. D. Billing and K. V. Mikkelsen, *Molecular Dynamics and Chemical Kinetics*, Wiley Interscience, New York, 1996.

[17] D. M. Neumark, Acc. Chem. Res. **26**, 33 (1992).

[18] J. C. Polanyi and A. H. Zewail, Acc. Chem. Res. **28**, 119 (1995).

[19] L. R. Khundkar and A. H. Zewail, Annu. Rev. Phys. Chem. **41**, 15 (1990).

[20] S. Mukamel, Annu. Rev. Phys. Chem. **41**, 647 (1990).

[21] W. T. Pollard and R. A. Mathies, Annu. Rev. Phys. Chem. **43**, 497 (1992).

[22] A. H. Zewail, editor, *Femtochemistry – Ultrafast Dynamics of the Chemical Bond*, Singapore, 1994, World Scientific.

[23] M. Chergui, editor, *Femtochemistry: Ultrafast Chemical and Physical Processes in Molecular Systems*, Singapore, 1996, World Scientific.

[24] V. Sundström, editor, *Femtochemistry and Femtobiology: Ultrafast Reaction Dynamics at Atomic–Scale Resolution*, London, 1997, Imperial College Press.

[25] W. Domcke, P. Hänggi, and D. Tannor, editors, *Special Issue on Dynamics of Driven Quantum Systems*, volume 217 of *Chem. Phys.*, 1997.

[26] P. Gaspard and I. Burghardt, editors, *Chemical Reactions and their Control on the Femtosecond Time Scale. XXth Solvay Conference on Chemistry*, volume 101, Adv. Chem. Phys., 1997.

[27] E. Schrödinger, Naturwiss. **14**, 664 (1926).

[28] C. Cohen-Tannoudji, B. Liu, and F. Laloe, *Quantum Mechanics*, Wiley, New York, 1977.

[29] M. D. Feit, J. A. Fleck, Jr, and A. Steiger, J. Comput. Phys. **47**, 412 (1982).

[30] H. Köppel, W. Domcke, and L. S. Cederbaum, Adv. Chem. Phys. **57**, 59 (1984).

[31] R. Kosloff, J. Phys. Chem. **92**, 2087 (1988).

[32] C. Leforestier, R. H. Bisseling, C. Cerjan, M. D. Feit, R. Friesner, A. Guldberg, A. Hammerich, G. Jolicard, W. Karrlein, H.-D. Meyer, N. Lipkin, O. Roncero, and R. Kosloff, J. Comp. Phys. **94**, 59 (1991).

[33] J. Broeckhove and L. Lathouwers, editors, *Time–Dependent Quantum Molecular Dynamics*, New York, 1992, Plenum.

[34] R. Kosloff, Annu. Rev. Phys. Chem. **45**, 145 (1994).

[35] G. C. Schatz and M. A. Ratner, *Quantum Mechanics in Chemistry*, Prentice Hall, Englewood Cliffs, NJ, 1993.

[36] J. Manz and L. Wöste, editors, *Femtosecond Chemistry*, Weinheim, 1995, Verlag Chemie.

[37] J. Manz, in *Femtochemistry and Femtobiology: Ultrafast Reaction Dynamics at Atomic–scale Resolution*, edited by V. Sundström, pages 80–318, Imperial College Press, London, 1997.

[38] W. Domcke and G. Stock, Adv. Chem. Phys. **100**, 1 (1997).

[39] D. C. Clary, editor, *Special Issue on Quantum Theory of Chemical Reactions*, volume 93 of *J. Chem. Soc. Faraday Trans.*, 1997.

[40] V. S. Dubov, L. I. Gudzenko, L. V. Gurvich, and S. I. Iakovlenko, Chem. Phys. Lett. **45**, 330 (1977).

[41] P. D. Lett, P. S. Julienne, and W. D. Phillips, Annu. Rev. Phys. Chem. **46**, 423 (1995).

[42] M. I. Christie, R. G. W. Norrish, and G.Porter, Proc. Roy. Soc. **A216**, 152 (1952).

[43] G. Porter, Disc. Faraday Soc. **33**, 198 (1962).

[44] J. Troe, Annu. Rev. Phys. Chem. **29**, 223 (1978).

[45] J. Troe, J. Phys. Chem. **90**, 357 (1986).

[46] J. T. Hynes, Annu. Rev. Phys. Chem. **36**, 573 (1985).

[47] R. Schinke, *Photodissociation Dynamics*, Cambridge University Press, Cambridge, 1993.

[48] E. J. Heller, P. L. Houston, R. D. Levine, and A. H. Zewail, editors, *James Lloyd Kinsey Festschrift: Spectroscopy of a Molecule Falling apart*, volume 100 of *J. Phys. Chem.*, 1996.

[49] J. Franck and E. Rabinovitch, Trans. Faraday Soc. **30**, 120 (1934).

[50] C. Wittig, S. Sharpe, and R. A. Beaudet, Acc. Chem. Res. **21**, 341 (1988).

[51] G. Scoles, editor, *The Chemical Physics of Atomic and Molecular Clusters*, Amsterdam, 1990, Proceedings of the Enrico Fermi Summer School (Varenna 1988), North-Holland.

[52] M. Takayanagi and I. Hanazaki, Chem. Rev. **91** (1991).

[53] *Special Issue on Reactions in and with Clusters*, volume 92 of *Ber. Bunsenges. Phys. Chem.*, 1993.

[54] V. A. Apkarian and V. E. Bondybey, editors, *Special Issue on Photophysics of Matrix–Isolated Molecules*, volume 189 of *Chem. Phys.*, 1994.

[55] R. B. Gerber, A. B. McCoy, and A. Garcia-Vela, Annu. Rev. Phys. Chem. **45**, 275 (1994).

[56] R. B. Gerber, A. B. McCoy, and A. Garcia-Vela, in *Femtosecond Chemistry*, edited by J. Manz and L. Wöste, chapter 16, Verlag Chemie, Weinheim, 1995.

[57] T. P. Martin, editor, *Large Clusters of Atoms and Molecules*, Netherlands, 1996, Kluwer Academic.

[58] D. Gerlich and S. Horning, Chem. Rev. **92**, 1509 (1992).

[59] M. Berblinger and C. Schlier, Mol. Phys. **63**, 779 (1988).

[60] L. Frommhold, *Collision–Induced Absorption in Gases*, Cambridge University Press, Cambridge, 1993.

[61] T. Sizer and M. G. Raymer, Phys. Rev. Lett. **56**, 123 (1986).

[62] T. Sizer and M. G. Raymer, Phys. Rev. A **36**, 2643 (1987).

[63] H. R. Thorsheim, J. Weiner, and P. S. Julienne, Phys. Rev. Lett. **58**, 2420 (1987).

[64] P. D. Lett, K. Helmerson, W. D. Phillips, L. P. Ratliff, S. L. Rolston, and M. E. Wagshul, Phys. Rev. Lett. **71**, 2200 (1993).

[65] L. P. Ratliff, M. E. Wagshul, P. D. Lett, S. L. Rolston, and W. D. Phillips, J. Chem. Phys. **101**, 2638 (1994).

[66] C. J. Williams and P. S. Julienne, J. Chem. Phys. **101**, 2634 (1994).

[67] Y. B. Band and P. S. Julienne, Phys. Rev. A **51**, 4317 (1995).

[68] D. Leonhardt and J. Weiner, Phys. Rev. A **52**, 4332 (1995).

[69] K. A. Suominen, J. Phys. B: At. Mol. Opt. Phys. **29**, 5981 (1996).

[70] J. L. Bohn and P. S. Julienne, Phys. Rev. A **54**, 4637 (1996).

[71] H. Wang, X. T. Wang, P. L. Gould, and W. C. Stwalley, J. Chem. Phys. **106**, 7899 (1997).

[72] H. Wang and W. C. Stwalley, J. Chem. Phys. **108**, 5767 (1998).

[73] J. Qin, T. O. Nelson, and D. W. Setser, J. Phys. Chem. **95**, 5374 (1991).

[74] J. H. Schloss, R. B. Jones, and J. G. Eden, J. Chem. Phys. **99**, 6483 (1993).

[75] G. Lo and D. W. Setser, J. Chem. Phys. **100**, 5432 (1994).

[76] A. W. McCown and J. G. Eden, J. Chem. Phys. **81**, 2933 (1984).

[77] E. B. Gordon, V. G. Egorov, S. E. Nalivaiko, V. S. Pavlenko, and O. S. Rzhevsky, Chem. Phys. Lett. **242**, 75 (1995).

[78] G. Rodriguez and J. G. Eden, J. Chem. Phys. **95**, 5539 (1991).

[79] J. Koperski, J. B. Atkinson, and L. Krause, Chem. Phys. Lett. **219**, 161 (1994).

[80] J. Koperski, J. B. Atkinson, and L. Krause, Can. J. Phys. **72**, 1070 (1994).

[81] P. Bicchi, C. Marinelli, and R. A. Bernheim, Phys. Rev. A **56**, 2025 (1997).

[82] U. Marvet and M. Dantus, Chem. Phys. Lett. **245**, 393 (1995).

[83] U. Marvet and M. Dantus, in *Femtochemistry: Ultrafast Chemical and Physical Processes in Molecular Systems*, edited by M. Chergui, pages 138–142, World Scientific, Singapore, 1996.

[84] P. Gross and M. Dantus, J. Chem. Phys **106**, 8013 (1997).

[85] U. Marvet, Q. Zhang, and M. Dantus, J. Phys. Chem. A **102**, 4111 (1998).

[86] H. M. J. M. Boesten, C. C. Tsai, B. J. Verhaar, and D. J. Heinzen, Phys. Rev. Lett. **77**, 5194 (1996).

[87] H. M. J. M. Boesten, C. C. Tsai, J. R. Gardner, D. J. Heinzen, and B. J. Verhaar, Phys. Rev. A **55**, 636 (1997).

[88] H. M. J. M. Boesten, C. C. Tsai, D. J. Heinzen, A. J. Moonen, and B. J. Verhaar, J. Phys. B, submitted (1998).

[89] C. Orzel, S. D. Bergeson, S. Kulin, and S. L. Rolston, Phys. Rev. Lett. **80**, 5093 (1998).

[90] M. Machholm, A. Giusti-Suzor, and F. H. Mies, Phys. Rev. A **50**, 5025 (1994).

[91] A. Vardi, D. Abrashkevich, E. Frishman, and M. Shapiro, J. Chem. Phys. **107**, 6166 (1997).

[92] I. D. Petsalakis, T. Mercouris, and C. A. Nicolaides, Chem. Phys. **189**, 615 (1994).

[93] P. Saalfrank, J. Chem. Phys, to be published (1998).

[94] S. K. Shin, Y. Chen, S. Nickolaisen, S. W. Sharpe, R. A. Beaudet, and C. Wittig, Adv. Photochem. **16**, 249 (1991).

[95] I. R. Sims, M. Gruebele, E. D. Potter, and A. H. Zewail, J. Chem. Phys. **97**, 4127 (1992).

[96] S. I. Ionov, G. A. Brucker, C. Jaques, L. Valachovic, and C. Wittig, J. Chem. Phys. **99**, 6553 (1993).

[97] S. Shi and H. Rabitz, Comp. Phys. Commun. **63**, 71 (1991).

[98] R. S. Judson and H. Rabitz, Phys. Rev. Lett. **68**, 1500 (1992).

[99] H. Rabitz, Nature **366**, 304 (1993).

[100] Z.-M. Lu and H. Rabitz, J. Phys. Chem. **99**, 13731 (1995).

[101] N. Wang and H. Rabitz, J. Chem. Phys. **104**, 1173 (1996).

[102] M. Shapiro and P. Brumer, J. Chem. Phys. **84** (1986).

[103] M. Shapiro, J. W. Hepburn, and P. Brumer, Chem. Phys. Lett. **149** (1988).

[104] M. Shapiro, J. Chem. Phys. **101** (1994).

[105] D. G. Abrashkevich, M. Shapiro, and P. Brumer, J. Chem. Phys. **108**, 3585 (1998).

[106] G. K. Paramonov and V. A. Savva, Phys. Lett. A **97**, 340 (1983).

[107] G. K. Paramonov, V. A. Savva, and A. M. Samson, Infrared Phys. **25**, 201 (1985).

[108] B. Just, J. Manz, and I. Trisca, Chem. Phys. Lett. **193**, 423 (1992).

[109] M. V. Korolkov, Y. A. Logvin, and G. K. Paramonov, J. Phys. Chem. **100**, 8070 (1996).

[110] G. K. Paramonov, in *Femtosecond Chemistry*, edited by J. Manz and L. Wöste, pages 671–712, Verlag Chemie, Weinheim, 1995.

[111] J. Manz, M. Oppel, and G. K. Paramonov, J. Phys. Chem. A **102**, 4271 (1998).

[112] J. E. Combariza, B. Just, J. Manz, and G. K. Paramonov, J. Phys. Chem. **95**, 10351 (1991).

[113] S. Chelkowski and A. D. Bandrauk, Chem. Phys. Lett. **233**, 185 (1995).

[114] M. Dohle, J. Manz, G. K. Paramonov, and H. Quast, Chem. Phys. **197**, 91 (1995).

[115] S. Chelkowski and A. D. Bandrauk, J. Chem. Phys. **99**, 4279 (1993).

[116] M. Kaluža and J. T. Muckerman, J. Chem. Phys. **105**, 535 (1996).

[117] M. V. Korolkov, G. K. Paramonov, and B. Schmidt, J. Chem. Phys. **105**, 1862 (1996).

[118] M. V. Korolkov, J. Manz, and G. K. Paramonov, Chem. Phys. **217**, 341 (1997).

[119] I. V. Andrianov and G. K. Paramonov, Phys. Rev. A **59**, 2134 (1999).

[120] C. Meier and V. Engel, in *Femtosecond Chemistry*, edited by J. Manz and L. Wöste, chapter 11, Verlag Chemie, Weinheim, 1995.

[121] I. N. Levine, *Quantum Chemistry*, Prentice–Hall, Englewood Cliffs, NJ, 1991.

[122] R. Loudon, *The Quantum Theory of Light*, Clarendon, Oxford, 1973.

[123] G. Arfken, *Mathematical Methods for Physicists*, Academic, Boston, 1985.

[124] K. C. Kulander, editor, *Time-Dependent Methods for Quantum Dynamics*, Amsterdam, 1991, North–Holland.

[125] M. D. Feit and J. A. Fleck, Jr, J. Chem. Phys. **78**, 301 (1983).

[126] J. Alvarellos and H. Metiu, J. Chem. Phys. **88**, 4957 (1988).

[127] A. D. Bandrauk and H. Shen, J. Chem. Phys. **99**, 1185 (1993).

[128] R. Meyer, J. Chem. Phys. **52**, 2053 (1970).

[129] C. C. Marston and G. G. Balint-Kurti, J. Chem. Phys. **91**, 3571 (1989).

[130] W. H. Press, S. A. Teukolsky, W. T. Vetterling, and B. P. Flannery, *Numerical Recipes in Fortran*, Cambridge University, Cambridge, 1992.

[131] J. R. Taylor, *Scattering Theory: The Quantum Theory on Nonrelativistic Collisions*, Wiley, New York, 1972.

[132] P. Pillet, A. Crubellier, A. Bleton, and O. Dulieu, J. Phys. B **30**, 2801 (1997).

[133] R. T. Lawton and M. S. Child, Mol. Phys. **40**, 773 (1980).

[134] M. S. Child and M. Halonen, Adv. Chem. Phys. **57**, 1 (1984).

[135] M. V. Korolkov and G. K. Paramonov, Phys. Rev. A. **57**, 4998 (1998).

[136] J. N. Murrel and K. S. Sorbie, J. Chem. Soc. Faraday Trans. II **68**, 1552 (1972).

[137] C. W. Bauschlicher and S. R. Langhoff, J. Chem. Phys. **87**, 4665 (1987).

[138] W. J. Stevens, G. Das, and A. C. Wahl, J. Chem. Phys. **61**, 3686 (1974).

[139] S.Chu, M.Yoshimine, and B.Liu, J. Chem. Phys. **61**, 5389 (1974).

[140] S. R. Langhoff, E. F. van Dishoeck, R. Wetmore, and A. Dalgarno, J. Chem. Phys. **77**, 1379 (1982).

[141] D. R. Yarkony, J. Chem. Phys. **97**, 1838 (1992).

[142] J. S. Wright and D. J. Donaldson, Chem. Phys. **94**, 15 (1985).

[143] R. Mecke, Z. Elektrochem. **54**, 38 (1950).

[144] G. F. Adams and C. F. Chabalowski, J. Phys. Chem. **98**, 5878 (1994).

[145] J. F. Ogilvie, W. R. Rodwell, and R. H. Tipping, J. Chem. Phys. **73**, 5221 (1980).

[146] M. Gavrila, editor, *Atoms in Intense Laser Fields*, San Diego, 1992, Academic.

[147] A. D. Bandrauk, editor, *Molecules in Intense Laser Fields*, New York, 1994, Dekker.

[148] A. D. Bandrauk and S. C. Wallace, editors, *Coherence Phenomena in Atoms and Molecules in Laser Fields*, New York, 1992, Plenum.

[149] A. Giusti-Suzor, F. H. Mies, L. F. DiMauro, E. Charron, and B. Yang, J. Phys. B. **28**, 309 (1995).

[150] K. W. Ford, D. L. Hill, M. Wakano, and J. A. Wheeler, Ann. Phys. **7**, 239 (1959).

[151] P. Courteille, R. S. Freeland, D. J. Heinzen, F. A. van Abeelen, and B. J. Verhaar, Phys. Rev. Lett. **81**, 69 (1998).

[152] F. A. van Abeelen, D. J. Heinzen, and B. J. Verhaar, Phys. Rev. A **57**, 4102 (1998).

[153] R. J. LeRoy, *Univerity of Waterloo Chemical Physics Research Report CP-555*, 1995.

[154] G. N. Makarov, Chem. Phys. Lett. **237**, 361 (1995).

[155] K. Balasubramanian, K. K. Das, and D. W. Liao, Chem. Phys. Lett. **195**, 487 (1992).

[156] E. W. Smith, R. E. Drullinger, M. M. Hessel, and J. Cooper, J. Chem. Phys. **66**, 5667 (1977).

[157] F. H. Mies, W. J. Stevens, and M. Krauss, J. Mol. Spectr. **72**, 303 (1978).

[158] K. C. Celestino and W. C. Ermler, J. Chem. Phys. **81**, 1872 (1984).

[159] R. D. van Zee, S. C. Blankespoor, and T. S. Zwier, J. Chem. Phys. **88**, 4650 (1988).

[160] J. Tellinghuisen, Adv. Chem. Phys. **60**, 399 (1985).

[161] I. S. Averbukh and N. F. Perelman, Phys. Lett. A **139**, 449 (1989).

[162] C. Leichtle, I. S. Averbukh, and W. P. Schleich, Phys. Rev. Lett. **77**, 3999 (1996).

[163] C. Leichtle, I. S. Averbukh, and W. P. Schleich, Phys. Rev. A **54**, 5299 (1996).

[164] P. Stifter, C. Leichtle, W. P. Schleich, and J. Markloff, Z. Naturforsch. **52 a**, 377 (1997).

[165] T. Baumert, V. Engel, C. Röttgermann, W. T. Strunz, and G. Gerber, Chem. Phys. Lett. **191**, 639 (1992).

[166] S. Y. Grebenshchikov, C. Beck, H. Flöthmann, D. H. Mordaunt, and R. Schinke, Chem. Phys. Lett. **271**, 197 (1997).

[167] P. M. Felker and A. H. Zewail, J. Chem. Phys. **86**, 2460 (1987).

[168] S. Baskin, P. M. Felker, and A. H. Zewail, J. Chem. Phys. **86**, 2483 (1987).

[169] P. M. Felker and A. H. Zewail, in *Femtosecond Chemistry*, edited by J. Manz and L. Wöste, chapter 5, Verlag Chemie, Weinheim, 1995.

[170] P. Backhaus, *Theoretische Untersuchungen zur Laserpuls–induzierten Stabilisierung von Stoßkomplexen*, PhD thesis, Freie Universität Berlin, 1998.

[171] P. Backhaus, J. Manz, and B. Schmidt, Adv. Chem. Phys. **101**, 86 (1997).

[172] G. Herzberg, *Spectra of Diatomic Molecules*, Van Nostrand–Reinhold, London, 1940.

[173] P. Backhaus, B. Schmidt, and M. Dantus, Chem. Phys. Lett. **306**, 18 (1999).

[174] R. B. Gerber, R. Alimi, A. Garcia-Vela, and Y. Hurwitz, in *Mode Selective Chemistry*, edited by J. Jortner, pages 201–215, Kluwer, Dordrecht, 1991.

[175] J. Nieman and R. Naaman, J. Chem. Phys. **84**, 3825 (1986).

[176] J. Nieman, J. Shwartz, and R. Naaman, Z. Phys. D **1**, 231 (1986).

[177] Y. Hurwitz, Y. Rudich, R. Naaman, and R. B. Gerber, J. Chem. Phys. **98**, 2941 (1993).

[178] X. Hu and W. L. Hase, J. Phys. Chem. **96**, 7535 (1992).

[179] X. Hu and C. C. Martens, J. Chem. Phys. **97**, 8805 (1992).

[180] X. Hu and C. C. Martens, J. Chem. Phys. **98**, 8551 (1993).

[181] X. Hu and C. C. Martens, J. Chem. Phys. **99**, 2654 (1993).

[182] X. Hu and C. C. Martens, J. Chem. Phys. **99**, 9532 (1993).

[183] H.-P. Kaukonen, U. Landman, and C. L. Cleveland, J. Chem. Phys. **95**, 4997 (1991).

[184] C. E. Klots, Nature **327**, 222 (1987).

[185] C. E. Klots, Physical Review A **39**, 339 (1989).

[186] E. Engel, U. R. Schmitt, H.-J. Lüdde, A. Toepfer, E. Wüst, R. M. Dreizler, O. Knospe, R. Schmidt, and P. Chattopadhyay, Phys. Rev. B **48**, 1862 (1993).

[187] G. Seifert, R. Schmidt, and H. O. Lutz, Phys. Lett. A **158**, 237 (1991).

[188] R. Schmidt, G. Seifert, and H. O. Lutz, Phys. Lett. A **158**, 231 (1991).

[189] G. Seifert and R. Schmidt, Int. J. Mod. Phys. B **6**, 3845 (1992).

[190] R. Schmidt and H. O. Lutz, Phys. Rev. A **45**, 7981 (1992).

[191] R. Schmidt and H. O. Lutz, Phys. Lett. A **183**, 338 (1993).

[192] F. Rohmund, E. E. B. Campbell, O. Knospe, G. Seifert, and R. Schmidt, Phys. Rev. Lett. **76**, 3289 (1996).

[193] D. Eichenauer and R. J. LeRoy, J. Chem. Phys. **88**, 2898 (1988).

[194] S. Leutwyler and J. Bösiger, Chem. Rev. **90**, 489 (1990).

[195] L. Perera and F. G. Amar, J. Chem. Phys. **93**, 4884 (1990).

[196] R. S. Berry, in *The Chemical Physics of Atomic and Molecular Clusters*, edited by G. Scoles, North–Holland, Amsterdam, 1990.

[197] M. A. Kmetic and R. J. LeRoy, J. Chem. Phys. **95**, 6271 (1991).

[198] U. Buck, B. Schmidt, and J. Siebers, J. Chem. Phys. **99**, 9428 (1993).

[199] U. Buck, Phys. Bl. **11**, 1052 (1994).

[200] J. Jellinek, V. Bonačić-Koutecký, P. Fantucci, and M. Wiechert, J. Chem. Phys. **101**, 10092 (1994).

[201] D. Reichardt, V. Bonačić-Koutecký, P. Fantucci, and J. Jellinek, Chem. Phys. Lett. **279**, 129 (1997).

[202] G. C. Schatz, Annu. Rev. Phys. Chem. **39**, 317 (1988).

[203] R. N. Porter and L. M. Raff, in *Dynamics of Molecular Collisions*, edited by W. H. Miller, pages 1–52, Plenum, New York, 1976.

[204] H. Goldstein, *Classical Mechanics*, Addison–Wesley, Reading, Ma., 1950.

[205] D. W. Heermann, *Computer Simulations in Theoretical Physics*, Springer, Berlin, 1986.

[206] C. W. Gear, *Numerical Initial Value Problems in Ordinary Differential Equations*, Prentice-Hall, Englewood Cliffs, N. J., 1971.

[207] M. P. Allen and D. J. Tildesley, *Computer Simulations of Liquids*, Clarendon, Oxford, 1987.

[208] H. J. C. Berendsen and W. F. van Gunsteren, in *Molecular Dynamics Simulation of Statistical Mechanical Systems*, pages 43–65, Soc. Italiana di Fisica, Bologna, 1986.

[209] G. C. Maitland, M. Rigby, E. B. Smith, and W. A. Wakeham, *Intermolecular Forces. Their Origin and Determination*, Clarendon Press, Oxford, 1981.

[210] R. A. Aziz and M. J. Slaman, Mol. Phys. **58**, 679 (1986).

[211] V. Aquilanti, D. Cappeletti, V. Lorent, E. Luzzatti, and F. Pirani, J. Phys. Chem. **97**, 2063 (1993).

[212] J. M. Hutson, J. Phys. Chem. **96**, 4237 (1992).

[213] J. M. Hutson, Annu. Rev. Phys. Chem. **41**, 123 (1990).

[214] M. P. Tosi and F. G. Fumi, J. Phys. Chem. Solids **25**, 45 (1964).

[215] D. E. Manolopoulos, J. Chem. Soc. Faraday Trans. **93**, 673 (1997).

[216] P. J. Kuntz, in *Dynamics of Molecular Collisions*, edited by W. H. Miller, pages 53–120, Plenum, New York, 1976.

[217] P. Jungwirth, Chem. Phys. Lett. **289**, 324 (1998).

[218] J. Farges, M. F. de Feraudy, B. Raoult, and G. Torchet, J. Chem. Phys. **78**, 5067 (1983).

[219] J. Farges, M. F. de Feraudy, B. Raoult, and G. Torchet, J. Chem. Phys. **84**, 3491 (1986).

[220] A. L. Mackay, Acta Crystallogr. **15**, 916 (1962).

[221] M. R. Hoare and P. Pal, in *Advances in Physics, 24*, edited by B. R. Coles, page 645, Taylor & Francis, London, 1975.

[222] F. A. Lindemann, Z. Phys. **11**, 609 (1911).

[223] C. L. Briant and J. J. Burton, J. Chem. Phys. **63**, 2045 (1975).

[224] J. Jellinek, T. L. Beck, and R. S. Berry, J. Chem. Phys. **84**, 2783 (1986).

[225] F. G. Amar and R. S. Berry, J. Chem. Phys. **85**, 5943 (1986).

[226] I. H. Gersonde and H. Gabriel, J. Chem. Phys. **98**, 2094 (1993).

[227] A. I. Krylov, R. B. Gerber, and V. A. Apkarian, Chem. Phys. **189**, 261 (1994).

[228] A. I. Krylov and R. B. Gerber, Chem. Phys. Lett. **231**, 395 (1994).

[229] A. I. Krylov, R. B. Gerber, and R. D. Coalson, J. Chem. Phys. **105**, 4626 (1996).

[230] A. I. Krylov and R. B. Gerber, J. Chem. Phys. **106**, 6574 (1997).

[231] M. Amini and R. W. Hockney, J. Non–Cryst. Sol. **31**, 447 (1979).

[232] T. P. Martin, Phys. Repts. **95**, 167 (1983).

[233] J. Diefenbach and T. P. Martin, J. Chem. Phys. **83**, 4585 (1985).

[234] T. P. Martin, T. Bergmann, and B. Wassermann, Cluster energy surfaces, in *Large Finite Systems*, edited by J. Jortner and B. Pullmann, Dordrecht, 1987, Proceedings of the 20^{th} Jerusalem Symposium on Quantum Chemistry and Biochemistry, Reidel.

[235] B. I. Dunlap, J. Chem. Phys. **84**, 5611 (1986).

[236] J. P. Rose and R. S. Berry, J. Chem. Phys. **98**, 3246 (1993).

[237] J. P. Rose and R. S. Berry, J. Chem. Phys. **98**, 3262 (1993).

[238] R. Schmidt, J. Schulte, O. Knospe, and G. Seifert, Phys. Lett. A **194**, 101 (1994).

[239] C. Ochsenfeld and R. Ahlrichs, Ber. Bunsenges. Phys. Chem. **98**, 34 (1994).

[240] A. Heidenreich, J. Jortner, and I. Oref, J. Chem. Phys. **97**, 197 (1992).

[241] J. P. Rose and R. S. Berry, J. Chem. Phys. **96**, 517 (1992).

[242] Z. Bačić and R. E. Miller, J. Phys. Chem. **100**, 12945 (1996).

[243] H. E. Hallam, editor, *Vibrational Spectroscopy of Trapped Species*, London, 1973, Wiley.

[244] L. Andrews and M. Moskovits, editors, *Chemistry and Physics of Matrix–Isolated Species*, Amsterdam, 1989, North–Holland.

[245] M. Chergui and N. Schwentner, Trends in Chem. Phys. **2**, 89 (1992).

[246] J. N. Murrell, A. J. Stace, and R. Dammel, J. Chem. Soc. Faraday Trans. 2 **74**, 1532 (1978).

[247] J.-M. Philippoz, R. Monot, and H. van den Berg, J. Chem. Phys. **93**, 8676 (1990).

[248] E. D. Potter, Q. Liu, and A. H. Zewail, Chem. Phys. Lett. **200**, 605 (1992).

[249] R. Zadoyan, Z. Li, C. C. Martens, and V. A. Apkarian, J. Chem. Phys. **101**, 6648 (1994).

[250] W. Wang, K. A. Nelson, L. Xiao, and D. F. Coker, J. Chem. Phys. **101**, 9663 (1994).

[251] M. P. de Miranda, J. A. Beswick, and N. Halberstadt, Chem. Phys. **187**, 185 (1994).

[252] Z. Li, R. Zadoyan, V. A. Apkarian, and C. C. Martens, J. Phys. Chem. **99**, 7453 (1995).

[253] J.-K. Wang, Q. Liu, and A. H. Zewail, J. Phys. Chem. **99**, 11309 (1995).

[254] Q. Liu, J.-K. Wang, and A. H. Zewail, J. Phys. Chem. **99**, 11321 (1995).

[255] J. Che, M. Messina, K. R. Wilson, V. A. Apkarian, Z. Li, C. C. Martens, and R. Zadoyan, J. Phys. Chem. **100**, 7873 (1996).

[256] H. Schröder and H. Gabriel, J. Chem. Phys. **104**, 587 (1996).

[257] V. S. Batista and D. F. Coker, J. Chem. Phys. **105**, 4033 (1996).

[258] C. Meier, V. Engel, and J. A. Beswick, Chem. Phys. Lett. **287**, 487 (1998).

[259] R. Alimi and R. B. Gerber, Phys. Rev. Lett. **64**, 1453 (1990).

[260] A. Garcia-Vela, R. B. Gerber, and J. J. Valentini, Chem. Phys. Lett. **186**, 223 (1991).

[261] A. Garcia-Vela, R. B. Gerber, and J. J. Valentini, J. Chem. Phys. **97**, 3297 (1992).

[262] A. Garcia-Vela, R. B. Gerber, and D. G. Imre, J. Chem. Phys. **97**, 7242 (1992).

[263] A. Garcia-Vela and R. B. Gerber, J. Chem. Phys. **98**, 427 (1993).

[264] A. Garcia-Vela, R. B. Gerber, D. G. Imre, and J. J. Valentini, Chem. Phys. Lett. **202**, 473 (1993).

[265] A. Garcia-Vela, R. B. Gerber, D. G. Imre, and J. J. Valentini, Phys. Rev. Lett. **71**, 931 (1993).

[266] A. Garcia-Vela and R. B. Gerber, J. Chem. Phys. **103**, 3463 (1995).

[267] A. Garcia-Vela and R. B. Gerber, J. Chem. Phys. **108**, 5755 (1998).

[268] T. Schröder, R. Schinke, M. Mandziuk, and Z. Bačić, J. Chem. Phys. **100**, 7239 (1994).

[269] T. Schröder, R. Schinke, and Z. Bačić, Chem. Phys. Lett. **235**, 316 (1995).

[270] E. Narevicius and N. Moiseyev, Chem. Phys. Lett. **287**, 250 (1998).

[271] R. Alimi, R. B. Gerber, and V. A. Apkarian, J. Chem. Phys. **89**, 174 (1988).

[272] T. Schröder, R. Schinke, S. Liu, Z. Bačić, and J. W. Moskowitz, J. Chem. Phys. **103**, 9228 (1995).

[273] A. Garcia-Vela, R. B. Gerber, and U. Buck, J. Phys. Chem. **98**, 3518 (1994).

[274] R. Alimi and R. B. Gerber, Chem. Phys. Lett. **173**, 393 (1990).

[275] F. Neugebauer and V. May, Chem. Phys. Lett. **289**, 67 (1998).

[276] J. Zoval and V. A. Apkarian, J. Phys. Chem. **98**, 7945 (1994).

[277] M. Y. Niv, A. I. Krylov, and R. B. Gerber, Faraday Discussion **108**, 243 (1998).

[278] M. Y. Niv, A. I. Krylov, R. B. Gerber, and U. Buck, in preparation (1998).

[279] V. S. Letokhov, Science **180**, 451 (1973).

[280] P. F. Zittel and D. D. Little, J. Chem. Phys. **71**, 713 (1979).

[281] F. F. Crim, Science **249**, 1387 (1990).

[282] D. G. Imre and J. Zhang, Chem. Phys. **139**, 89 (1989).

[283] F. F. Crim, Annu. Rev. Phys. Chem. **44**, 397 (1993).

[284] F. F. Crim, J. Phys. Chem. **100**, 12725 (1996).

[285] C. Daniel, R. de Vivie-Riedle, M.-C. Heitz, J. Manz, and P. Saalfrank, Int. J. Quant. Chem. **57**, 595 (1996).

[286] J. Manz, J. Am. Chem. Soc. **102**, 1801 (1980).

[287] L. Pauling, Phys. Rev. **36**, 430 (1930).

[288] W. H. Flygare, J. Chem. Phys. **39**, 2263 (1963).

[289] H. Kono and S. H. Lin, J. Chem. Phys. **78**, 2607 (1983).

[290] H. Dubost, in *Inert Gases*, edited by M. L. Klein, volume 34 of *Series in Chemical Physics*, chapter 4, Springer, Berlin, 1984.

[291] R. Alimi, A. Brokman, and R. B. Gerber, J. Chem. Phys. **91**, 1611 (1989).

[292] H. Kunttu and V. A. Apkarian, Chem. Phys. Lett. **171**, 423 (1990).

[293] A. V. Benderskii and C. A. Wight, J. Chem. Phys. **101**, 292 (1994).

[294] M. Lewerenz, J. Chem. Phys. **104**, 1028 (1996).

[295] A. R. Cooper and J. M. Hutson, J. Chem. Phys. **98**, 5337 (1992).

[296] A. Ernesti and J. M. Hutson, Faraday Discuss. **97**, 119 (1994).

[297] A. Ernesti and J. M. Hutson, Phys. Rev. A **51**, 239 (1995).

[298] J. M. Hutson, J. Chem.Phys. **96**, 6752 (1992).

[299] T. H. Dunning Jr., J. Chem. Phys. **65**, 3854 (1976).

[300] D. M. Hirst and M. F. Guest, Mol. Phys. **41**, 1483 (1980).

[301] P. Ždánská, B. Schmidt, and P. Jungwirth, J. Chem. Phys **110**, 6246 (1999).

[302] E. Aquilanti, E. Luzzatti, F. Pirani, and G. G. Volpi, J. Chem. Phys. **89**, 6165 (1988).

[303] R. W. Bickes, Jr, B. Lantzsch, J. P. Toennies, and K. Walaschewski, Faraday Discuss. Chem. Soc. **55**, 167 (1973).

[304] K. T. Tang and J. P. Toennies, Chem. Phys. **156**, 413 (1991).

[305] V. Aquilanti, G. Liuti, F. Pirani, and F. Vecchiocattivi, J. Chem. Soc. Faraday Trans. 2 **85**, 955 (1989).

[306] J. C. Tully, in *Dynamics of Molecular Collisions*, edited by W. H. Miller, pages 217–267, Plenum, New York, 1976.

[307] J. C. Tully, J. Chem. Phys. **93**, 1061 (1990).

[308] F. M. Tao and W. Klemperer, J. Chem. Phys. **101**, 1129 (1994).

[309] B. L. Grigorenko, A. V. Nemukhin, and V. A. Apkarian, J. Chem. Phys. **104**, 5510 (1997).

[310] B. L. Grigorenko and A. V. Nemukhin, Chem. Phys. Lett. **270**, 103 (1997).

[311] D. T. Anderson and J. S. Winn, Chem. Phys. **189**, 171 (1994).

[312] D. T. Anderson, S. Davis, and D. J. Nesbitt, J. Chem. Phys. **107**, 1115 (1997).

[313] S. Goyal, D. L. Schutt, and G. Scoles, J. Chem. Phys. **97**, 2236 (1993).

[314] S. Goyal, D. L. Schutt, and G. Scoles, J. Chem. Phys. **102**, 2302 (1995).

[315] S. Liu, Z. Bacic, J. W. Moskowitz, and K. E. Schmidt, J. Chem. Phys. **103**, 1829 (1995).

[316] H. Friedmann and S. Kimel, J. Chem. Phys. **43**, 3925 (1965).

[317] H. Friedmann and S. Kimel, J. Chem. Phys. **47**, 3589 (1967).

[318] R. C. Mowrey and D. J. Kouri, J. Chem. Phys. **84**, 6466 (1986).

[319] D. J. Kouri and R. C. Mowrey, J. Chem. Phys. **86**, 2087 (1987).

[320] M. E. Rose, *Elementary Theory of Angular Momentum*, J. Wiley, New York, 1957.

[321] A. R. Edmonds, *Angular Momentum in Quantum Mechanics*, Princeton University, Princeton, 1960.

[322] R. N. Zare, *Angular Momentum. Understanding Spatial Aspects in Chemistry and Physics*, Wiley, New York, 1987.

[323] S. Mahapatra, J. Chem. Soc. Faraday Trans. **93**, 773 (1997).

[324] H. Tal-Ezer and R. Kosloff, J. Chem. Phys. **81**, 3967 (1984).

[325] P. Nettesheim, W. Huisinga, and C. Schütte, Konrad–Zuse–Center (Berlin), Preprint SC-96-47 , available through `http://www.zib.de/bib`.

[326] R. B. Gerber, V. Buch, and M. A. Ratner, J. Chem. Phys. **77**, 3022 (1982).

[327] R. B. Gerber, M. A. Ratner, and V. Buch, Chem. Phys. Lett. **91**, 173 (1982).

[328] J. Mavri, H. J. C. Berendsen, and W. F. van Gunsteren, J. Phys. Chem. **97**, 13469 (1993).

[329] P. Bala, B. Lesyng, and J. A. McCammon, Chem. Phys. Lett. **219**, 259 (1994).

[330] P. Bala, P. Grochowski, B. Lesyng, and J. A. McCammon, J. Phys. Chem. **100**, 2535 (1996).

[331] S. Hammes-Schiffer and J. C. Tully, J. Chem. Phys. **101**, 4657 (1994).

[332] S. Hammes-Schiffer and J. C. Tully, J. Chem. Phys. **105**, 2236 (1996).

[333] N. P. Blake and H. Metiu, J. Chem. Phys. **101**, 223 (1994).

[334] N. Balakrishnan and G. D. Billing, J. Chem. Phys. **104**, 4005 (1996).

[335] G. D. Billing, J. Chem. Soc. Faraday Trans. **93**, 833 (1997).

[336] F. A. Bornemann, P. Nettesheim, and C. Schütte, J. Chem. Phys. **105**, 1074 (1996).

[337] F. A. Bornemann and C. Schütte, SIAM J. Appl. Math. **59**, 1208 (1999).

[338] C. Schütte and F. A. Bornemann, in *Computational Molecular Dynamics: Challenges, Methods, Ideas*, edited by P. Deuflhard, J. Hermans, B. Leimkuhler, A. E. Mark, S. Reich, and R. D. Skeel, volume 4 of *Lecture Notes in Computational Science and Engineering*, pages 380–395, Springer, 1999.

[339] U. Müller and G. Stock, J. Chem. Phys. **108**, 7516 (1998).

[340] J. L. McWhirter, J. Chem. Phys. **108**, 5683 (1998).

[341] P. Nettesheim and C. Schütte, in *Computational Molecular Dynamics: Challenges, Methods, Ideas*, edited by P. Deuflhard, J. Hermans, B. Leimkuhler, A. E. Mark, S. Reich, and R. D. Skeel, volume 4 of *Lecture Notes in Computational Science and Engineering*, pages 396–411, Springer, 1999.

[342] U. Schmitt and J. Brickmann, Chem. Phys. **208**, 45 (1996).

[343] P. Nettesheim, Konrad–Zuse–Center, Preprint SC-98-37 (1998), available through `http://www.zib.de/bib`.

[344] C. J. Bradley and A. P. Cracknell, *The Mathematical Theory of Symmetry in Solids*, Clarendon, Oxford, 1972.

[345] F. A. Cotton, *Chemical Applications of Group Theory*, Wiley, New York, 1963.

[346] M.Tinkham, *Group Theory and Quantum Mechanics*, McGraw-Hill, New York, 1964.

[347] N. V. Cohan, Proc. Cambridge Phil. Soc. **54**, 28 (1958).

[348] A. G. McLellan, J. Chem. Phys. **34**, 1350 (1961).

[349] K. H. Michel, Z. Phys. B. **88**, 71 (1992).

[350] L. Elcoro, J. M. Perez-Mato, and G. Madariaga, Acta Cryst. A **50**, 182 (1994).

[351] W. Prandl, P. Schiebel, and K. Wulf, Acta Cryst. **A 52**, 171 (1996).

[352] Y. Zheng and P. C. Doerschuk, Acta Cryst. A **52**, 221 (1996).

[353] Z. Bacic, J. Chem. Soc. Faraday Trans. **93**, 1459 (1997).

[354] P. Korpiun and E. Lüscher, in *Rare Gas Solids*, edited by M. L. Klein and J. A. Venables, volume 2, chapter 12, page 729, Academic, New York, 1977.

[355] A. McIlroy, R. Lascola, C. M. Lovejoy, and D. J. Nesbitt, J. Phys. Chem. **95**, 2636 (1991).

[356] M. T. Bowers, G. I. Kerley, and W. H. Flygare, J. Chem. Phys. **45**, 3399 (1966).

[357] M. G. Mason, W. G. von Holle, and D. W. Robinson, J. Chem. Phys. **54**, 3491 (1971).

[358] L. Andrews and G. L. Johnson, J. Phys. Chem. **88**, 425 (1984).

[359] S. Liu, Z. Bacic, J. W. Moskowitz, and K. E. Schmidt, J. Chem. Phys. **100**, 7166 (1994).

[360] S. Liu, Z. Bacic, J. W. Moskowitz, and K. E. Schmidt, J. Chem. Phys. **101**, 6359 (1994).

[361] S. Liu, Z. Bacic, J. W. Moskowitz, and K. E. Schmidt, J. Chem. Phys. **101**, 10181 (1994).

[362] L.-C. Brunel, J.-C. Bureau, and M. Peyron, Chem. Phys. **28** (1978).

[363] D. Maillard, A. Schriver, J. P. Perchard, and C. Girardet, J. Chem. Phys. **71**, 505 (1979).

[364] J. M. Wiesenfeld and C. B. Moore, J. Chem. Phys. **70**, 930 (1979).

[365] L. Young and C. B. Moore, J. Chem. Phys. **81**, 3137 (1984).

[366] M. Domin, *Theoretische Untersuchungen zu Struktur und Infrarotspektren von HF in kleinen Argonclustern*, Diploma thesis, Freie Universität Berlin, 1998.

[367] P. Niyaz, Z. Bacic, J. W. Moskowitz, and K. E. Schmidt, Chem. Phys. Lett. **252**, 23 (1996).

[368] R. B. Gerber and M. A. Ratner, J. Phys. Chem. **92**, 3252 (1988).

[369] R. B. Gerber and M. A. Ratner, Adv. Chem. Phys. **70**, 97 (1988).

[370] J. O. Jung and R. B. Gerber, J. Chem. Phys. **105**, 10682 (1996).

[371] E. Fredj, R. B. Gerber, and M. A. Ratner, J. Chem. Phys. **105**, 1121 (1996).

[372] B. Schmidt, P. Jungwirth, and R. B. Gerber, in *Ultrafast Chemical and Physical Processes in Molecular Systems*, edited by M. Chergui, pages 637–640, World Scientific, Singapore, 1996.

[373] H. U. Beyeler, J. Chem. Phys. **60**, 4123 (1974).

[374] A. F. Devonshire, Proc. Roy. Soc. (London) A **153**, 601 (1936).

[375] H. E. Hallam, in *Vibrational Spectrocopy of Trapped Species*, edited by H. E. Hallam, pages 67–132, Wiley, London, 1973.

[376] K. H. Gödderz, N. Schwentner, and M. Chergui, J. Chem. Phys. **105**, 451 (1996).

[377] E. J. Heller, Acc. Chem. Res. **14**, 368 (1981).

[378] D. Neuhauser, J. Chem. Phys. **93**, 2611 (1990).

[379] V. A. Mandelshtam and H. S. Taylor, J. Chem. Phys **107**, 6756 (1998).

[380] V. A. Mandelshtam, J. Chem. Phys. **108**, 9999 (1998).

[381] P. Jungwirth, B. Schmidt, and N. Moiseyev, Chem. Phys. Lett. **280**, 177 (1997).

[382] A. Cenian, S. Hennig, and H. Gabriel, J. Chem. Phys. **102**, 9276 (1995).

[383] M. Ovchinnikov and V. A. Apkarian, J. Chem. Phys. **108**, 2277 (1998).

[384] A. Borrmann and C. C. Martens, J. Chem. Phys. **102**, 1905 (1995).

[385] E. I. Tarasova, A. M. Ratner, V. M. Stepanenko, I. Y. Fugol, M. Chergui, R. Schriever, and N. Schwentner, J. Chem. Phys. **98**, 7786 (1993).

[386] M. Hintenender, F. Rebentrost, R. B. Gerber, and R. Kosloff, J. Chem. Phys. **102**, 578 (1995).

[387] M. Hintenender, F. Rebentrost, R. Kosloff, and R. B. Gerber, J. Chem. Phys. **105**, 11347 (1997).

[388] P. Nettesheim, F. A. Bornemann, B. Schmidt, and C. Schütte, Chem. Phys. Lett. **256**, 581 (1996).

[389] P. Jungwirth, P. Žďánská, and B. Schmidt, J. Phys. Chem. **102**, 7241 (1998).

[390] E. J. Heller, J. Chem. Phys. **62**, 1544 (1975).

[391] K. Haug and H. Metiu, J. Chem. Phys. **99**, 6253 (1993).

[392] N. P. Blake and H. Metiu, in *Femtosecond Chemistry*, edited by J. Manz and L. Wöste, chapter 17, Verlag Chemie, Weinheim, 1995.

[393] P. A. M. Dirac, Proc. Cambridge Phil. Soc. **26**, 376 (1930).

[394] A. D. McLachlan, Mol. Phys. **8**, 39 (1963).

[395] T. Gunkel, H.-J. Bär, M. Engel, E. Yurtsever, and J. Brickmann, Ber. Bunsenges. Phys. Chem. **98**, 1552 (1994).

[396] P. Jungwirth and R. B. Gerber, J. Chem. Phys. **102**, 6046 (1995).

[397] P. Jungwirth and R. B. Gerber, J. Chem. Phys. **102**, 8855 (1995).

[398] P. Jungwirth, E. Fredj, and R. B. Gerber, J. Chem. Phys. **104**, 9332 (1996).

[399] P. Jungwirth, E. Fredj, P. Zdanska, and R. B. Gerber, Computers and Chemistry **21**, 419 (1997).

[400] N. Makri and W. H. Miller, J. Chem. Phys. **87**, 5781 (1987).

[401] N. Makri, Chem. Phys. Lett. **169**, 541 (1990).

[402] Z. Kotler, A. Nitzan, and R. Kosloff, Chem. Phys. Lett. **153**, 483 (1988).

[403] Z. Kotler, E. Neria, and A. Nitzan, Comp. Phys. Commun. **63**, 243 (1991).

[404] J. Campos-Martinez and R. D. Coalson, J. Chem. Phys. **93**, 4740 (1990).

[405] J. Campos-Martinez, J. R. Waldeck, and R. D. Coalson, J. Chem. Phys. **96**, 3613 (1992).

[406] R. B. Gerber, P. Jungwirth, E. Fredj, and A. Y. Rom, in *Multidimensional Dynamics Methods*, edited by D. L. Thompson, World Scientific, Singapore, 1997.

[407] P. Jungwirth, E. Fredj, and R. B. Gerber, J. Chem. Phys. **107**, 8963 (1997).

[408] P. Jungwirth and B. Schmidt, Chem. Phys. Lett. **275**, 127 (1997).

[409] A. I. Krylov and R. B. Gerber, in *Ultrafast Chemical and Physical Processes in Molecular Systems*, edited by M. Chergui, pages 628–632, World Scientific, Singapore, 1996.

List of Figures

1.1 General scheme of (photo–)association and (photo–)dissociation reactions 8

2.1 Model of the OH molecule 24
2.2 Photodissociation spectrum of OH by pulsed IR lasers 26
2.3 Ground state photoassociation of OH 28
2.4 Population dynamics of ground state photoassociation 29
2.5 Photoacceleration spectrum of an OH collision pair 30
2.6 Excited state photoassociation of an OH collision pair 31
2.7 Two–pulse strategy for excited state photoassociation 33
2.8 Bound and quasi-bound states of the HCl molecule 35
2.9 Population dynamics and state selectivity of HCl photoassociation 36
2.10 Photoinduced association and acceleration of HCl collision pairs . 38
2.11 Potential energy curves and transition dipole moment of Hg_2 . . 41
2.12 Excitation probabilities for mercury photoassociation 42
2.13 Pump–probe spectra of mercury photoassociation dynamics . . . 43
2.14 Averaged pump–probe spectra of mercury 46

3.1 Initial conditions of a molecular collision 54
3.2 Total and partial cross sections for the HCl formation 59
3.3 Distribution of velocities and collision times 60
3.4 Formation of a long–lived complex 61
3.5 Reaction mechanism for the $H + ClAr_{12}$ collision pair 63
3.6 Thermal and structural properties of the $ClAr_{12}$ cluster 65
3.7 Temperature dependence of the $H + ClAr_{12} \rightarrow HCl + 12Ar$ association reaction 67
3.8 Product survival probabilities and associative cross sections for cluster–cluster collisions 71

4.1 Atom–molecule ground state potentials for Ar–HF, Ar–HCl . . . 81
4.2 Atom–atom excited state potentials for Ar–HF, Ar–HCl 82
4.3 HX (X = F, Cl) configuration in rare gas cluster, matrix 83
4.4 HX (X = F, Cl) vibrational frequency shift in argon cluster, matrix 90
4.5 Classical trajectories for HCl photodissociation in an argon matrix 92
4.6 Potential for molecular rotation in an Ar cluster and matrix . . . 94
4.7 Rotational wavefunctions of HF/HCl in an icosahedral $HFAr_{12}$ cluster 96

4.8 Rotational wavefunctions of HF/HCl in an octahedral Ar matrix 97
4.9 Photodissociation of HCl in Ar(fcc). Initial state $J = 0$ (A_{1g}) . . 99
4.10 Photodissociation of HCl in Ar(fcc). Initial state $J = 3$ (A_{2u}) . . 100
4.11 Photodissociation of HCl in Ar(fcc). Initial state $J = 3$ ($T2u$) . . 101
4.12 Cage exit probability upon photodissociation of HCl in Ar(fcc) . 102
4.13 Autocorrelation and absorption spectrum of HCl in Ar_{12} (I_h) . . 103
4.14 QCMD simulation of HCl/DCl photodissociation in icosahedral $HClAr_{12}$. 105

Appendix A

Photo–Induced Stabilization

A.1 Vibrational State–Selectivity

Vibrationally State Selective Photoassociation by
Infrared Picosecond Laser Pulses:
Model Simulations for O + H → OH(v)

M. V. Korolkov, J. Manz, G. K. Paramonov, and B. Schmidt

Chem. Phys. Lett. **260**(5–6), 604–610 (1996)
DOI:10.1016/0009-2614(96)00938-4

A.2 Competition with Photoacceleration

Infrared Picosecond Laser Control of
Acceleration of Neutral Atoms:
Model Simulations for the Collision Pair O + H

M. V. Korolkov and B. Schmidt

Chem. Phys. Lett. **272**(1–2), 96–102 (1997)
DOI:10.1016/S0009-2614(97)00512-5

A.3 Electronic State–Selectivity

Vibrationally State-Selective Laser Pulse Control of Electronic Branching in OH ($X^2\Pi/A^2\Sigma^+$) Photoassociation

M. V. Korolkov and B. Schmidt

Chem. Phys. **237**(1–2), 123–138 (1998)
DOI:10.1016/S0301-0104(98)00219-5

A.4 Rotational State Selectivity

Effect of Rotations and Shape Resonances on Photoassociation and Photoacceleration by Ultrashort Infrared Laser Pulses

P. Backhaus, J. Manz, and B. Schmidt

J. Phys. Chem. A **102**(23), 4118–4128 (1998)
DOI:10.1021/jp9800057

A.5 Wavepacket Dynamics

Femtosecond Quantum Dynamics
of Photoassociation Reactions:
The Exciplex Formation of Mercury

P. Backhaus and B. Schmidt

Chem. Phys. **217**(2–3), 131–143 (1997)
DOI:10.1016/S0301-0104(97)00035-9

Appendix B

Solvent–Induced Stabilization

B.1 Three–Body Collisions and the Chaperon Effect

Solvation Effects on Association Reactions in Microclusters:
Classical Trajectory Study of H + $Cl(Ar)_n$

B. Schmidt and R. B. Gerber

J. Chem. Phys **101**(1), 343–355 (1994)
DOI:10.1063/1.468141

B.2 Phase Transitions and the Cage Effect

Reactive Collisions as a Signature for
Meltinglike Transitions in Clusters

B. Schmidt and R. B. Gerber

Phys. Rev. Lett. **72**(15), 2490–2493 (1994)
DOI:10.1103/PhysRevLett.72.2490

B.3 Effect of Evaporative Cooling

Cluster Growth From the Gas Phase:
Associative Collisions of Small
Alkali Halide Aggregates

B. Meißner, B. Schmidt, and R. S. Berry,

Z. Phys. Chem. **195**, 237–251 (1996)
http://www.z-phys-chem.de

Appendix C

Photodissociation Dynamics

C.1 Vibrational Frequency Shifts

Vibrational Line Shifts of
Hydrogen Halides in a Rare Gas Environment:
HF/DF and HCl/DCl in Ar Matrices and Clusters

B. Schmidt and P. Jungwirth

Chem. Phys. Lett., **259**(1-2), 62-68 (1996)
DOI:10.1016/0009-2614(96)00718-X

C.2 Photodissociation of Molecules in Clusters

Quantum Dynamics of HF Photodissociation
in Icosahedral $Ar_{12}HF$ Clusters:
Rotational Control of the
Hydrogen Atom Cage Exit

B. Schmidt

Chem. Phys. Lett. **301**(3–4), 207–216 (1999)
DOI:10.1016/S0009-2614(99)00030-5

C.3 Photodissociation of Molecules in Matrices

Quantum Dynamical Aspects of Rotationally and Vibrationally Mediated Photochemistry in Matrices and at Surfaces: HCl/DCl in Ar, and NH_3/ND_3 at Cu(111)

J. Manz, P. Saalfrank, and B. Schmidt

J. Chem. Soc. Faraday Trans. **93**(5), 957–967 (1997)
DOI:10.1039/a606144c